MODELING THREE REACTING FLOW SYSTEMS WITH MODERN COMPUTATIONAL FLUID DYNAMICS

by

Ralph J. Price

A dissertation submitted to the faculty of

Brigham Young University

in partial fulfillment of the requirements for the degree of

Doctor of Philosophy

Department of Chemical Engineering

Brigham Young University

August 2007

BRIGHAM YOUNG UNIVERSITY

GRADUATE COMMITTEE APPROVAL

of a dissertation submitted by

Ralph J. Price

This dissertation has been read by each member of the following graduate committee and by majority vote has been found to be satisfactory.

April 13, 2007 Date	Thomas H. Fl Thomas H. Fletcher, Chair
APRIL 13, 2007 Date	Merrill W Beckstead Merrill W. Beckstead
April 13, 2007 Date	Joseph D Smith Joseph D. Smith
April 13, 2007 Date	William G. Pitt William G. Pitt
April 13, 2007 Date	Dean R. Wh Dean R. Wheeler

BRIGHAM YOUNG UNIVERSITY

As chair of the candidate's graduate committee, I have read the dissertation of Ralph J. Price in its final form and have found that (1) its format, citations, and bibliographical style are consistent and acceptable and fulfill university and department style requirements; (2) its illustrative materials including figures, tables, and charts are in place; and (3) the final manuscript is satisfactory to the graduate committee and is ready for submission to the university library.

April 13, 2007
Date

Thomas H. Flet
Thomas H. Fletcher
Chair, Graduate Committee

Accepted for the Department

Larry Baxt
Larry L. Baxter
Graduate Coordinator

Accepted for the College

Alan R. Parkinson
Dean, Ira A. Fulton College of Engineering and Technology

ABSTRACT

MODELING THREE REACTING FLOW SYSTEMS WITH MODERN COMPUTATIONAL FLUID DYNAMICS

Ralph J. Price

Department of Chemical Engineering

Doctor of Philosophy

Computational fluid dynamics (CFD) modeling and analysis were used in three projects: solar CO_2 conversion modeling, improved coal combustion modeling using STAR-CD, and premixed combustion modeling. Each project is described below.

The solar CO_2 conversion modeling project involved CFD simulations of a prototype solar CO_2 converter that uses sunlight to dissociate CO_2 into CO and O_2. Modeling was used to predict the performance of this prototype converter using three CFD software packages, and involved predicting the flow, heat transfer, and chemical kinetics. Accuracy was determined by comparison of model predictions and experimental data. Parametric modeling studies were performed in order to better understand converter performance and limitations. Modeling analysis led to proposed operational and design changes meant to improve converter performance. Modeling was performed to quantify the effects of proposed design modifications and operational adjustments. Modeling was

also used to study the effects of pressure, some geometric design changes, and changing from pure CO_2 to a CO_2/He mixture. The insights gained from these modeling studies have played a key role in improving the performance of this process.

The second project involved the implementation of advanced coal models into STAR-CD, a commercial CFD program. These coal models were originally developed for PCGC-3, a code developed at Brigham Young University. This project involved modifying modern PCGC-3 coal combustion and gasification models so that they could be incorporated into STAR-CD. Models implemented included a coal set-up subroutine, and coal reactions models for devolatilization, char oxidation, and vaporization. Each implemented model was tested to verify its accuracy by comparison of model predictions with experimental data. All implemented coal submodels were validated by comparison between overall modeling predictions and experimental data. These implemented coal models increased the capability of STAR-CD to model coal combustion and gasification systems.

The third project was to assemble previously obtained experimental data on lean, premixed natural gas combustion. Velocity, temperature, and species concentration measurements were previously taken throughout a laboratory-scale gas turbine combustor using advanced laser diagnostics. However, these data were taken by different investigators at BYU over the course of 10 years, and the data were scattered through several publications, theses, and dissertations. This third project was to compile these data into a central location for analysis and distribution. This data set is excellent for validation of any comprehensive combustion model, and is now accessible to the public.

ACKNOWLEDGMENTS

I would, first off, like to thank my advisor, Dr. Thomas Fletcher for all his hard work, support, and encouragement. He has been a great example of a well-rounded individual who balances all his professional, spiritual, and personal commitments.

I would like to thank the individuals from CD-adapco who allowed me to help with the installation and verification of the ACERC coal submodels. I would especially like to thank Rajesh Rawat and Yongzhe Zhang from CD-adapco who worked directly with me. Joseph Smith was also instrumental in bringing ACERC and CD-adapco together for this project. He also gave me in-depth training on using STAR-CD software.

I would like to thank Reed Jensen from Los Alamos Renewable Energy Corporation. He was the one who dreamed up the idea of solar CO_2 conversion and also funded most of the solar CO_2 conversion modeling research. He also provided ideas and insight that enabled the CFD modeling efforts to be as thorough and beneficial as possible.

I would like to thank Paul Hedman, a retired professor at BYU. He was helpful in locating and obtaining all the data taken on the Laboratory Scale Gas Turbine Combustor. He also concisely explained the LSGTC facility.

I would especially like to thank Bill and Margaret Pope, who provided funding through the Bill and Margaret Pope Professorship. This financial support enabled me to work on all my projects without worry.

I would like to thank David Morse and Steve Hardy, two undergraduate students who helped with my research. David Morse helped with the PCGC-3 modeling, and Steve Hardy crunched some numbers for the FLUENT modeling work.

I would lastly like to thank my family for instilling in me the value of education and importance of hard work and dedication.

TABLE OF CONTENTS

LIST OF TABLES

LIST OF FIGURES

NOMENCLATURE

Symbol	**Definition**	**Units**
A	Mixing Rate Parameter	None
A	Pre-exponential Factor	Units Vary
B	Mixing Rate Parameter	None
B_{ji}	Transpiration Parameter	None
C_A	Concentration of Species A	mol/m^3
C_d	Mixture Fraction Constant	None
C_g	Mixture Fraction Constant	None
C_P	Heat Capacity	kJ/kg-s
D	Pipe Diameter	m
D_{ab}	Binary Diffusivity	m^2/s
D_{im}	Effective Mixture Diffusivity	m^2/s
E	Energy	J
E_a	Activation Energy	J/mol
F(p)	Statistical Relationship in CPD Model	None
H	Enthalpy	kJ/kg
I	Radiation Intensity	W/m^2
L	Length	cm
K(p)	Statistical Relationship in CPD Model	None
K_{eq}	Equilibrium Constant	None
MW_A	Molecular Weight of Species A	g/mol
Nu	Nusselt Number	None
Pr	Prandtl Number	None
Q	Heat	W/m^2
R	Ideal Gas Constant	J/mol-K
Re	Reynolds Number	None
S	Source Term	Units Vary
S^{part}	Source Term from Particle Phase	Units Vary
S_f	Fraction of Particle Surface Evaporating	None
SA	Particle Surface Area	m^2
Sh	Sherwood Number	None
T	Temperature	K
Y	Volatiles/Char Split Parameter	None
b	Reaction Temperature Exponent	None
c	Overall Concentration	mol/m^3
c	Fraction of Char Bridges (CPD Model)	None

d	Particle Diameter	m
f	Mixture Fraction	None
f	Fractional Amount (CPD Model)	None
g	Mixture Fraction Variance	None
g	Gravitational Acceleration	m/s^2
g	Fraction of Light Gas (CPD Model)	None
h	Convective Heat Transfer Coefficient	W/m^2-K
h	Planck's Constant	
h	Specific Enthalpy	kJ/kg
k	Thermal Conductivity	W/m-K
k	Reaction-rate Constant	Units Vary
k	Turbulent Kinetic Energy	kJ/kg
k_c	Convective Mass Transfer Coefficient	m/s
$\dot{m}_A$	Flow rate of Species A	mg/s
n	Number of molecules	None
n	Reaction Order	None
p	Pressure	kPa
p	Number of Intact Bridges in Coal Lattice (CPD)	None
q	Heat Flux	W/m^2
r	Reaction Rate	Units Vary
r	Ratio of Bridge Mass to Site Mass	None
s	Unit Vector in the Radiation Direction	None
t	Time	s
v	Velocity	m/s
x_A	Mole Fraction of Species A	No Units
£	Fractional Number of Labile Bridges	None
$£^*$	Fraction of Reactive Bridge Intermediates	None
Φ	Radiation In-scattering Function (RTE)	None
Φ	Radiation Ordinate Direction	None
Φ	Statistical Relationship in CPD Model	None
Θ	Radiation Ordinate Direction	None
Ω	Statistical Relationship in CPD Model	None
α_m	Particle Volatiles Mass	kg
β	Radiation Extinction Coefficient (RTE)	m^{-1}
ε	Turbulent Dissipation Rate	kW/kg
ϕ	Photon Flux	photons/cm^2-s
ϕ	Stoichiometric Ratio of Char to Oxidizer	None
η	Quenching Efficiency	None
η	Overall Effectiveness Factor (CBK Model)	None
κ	Radiation Absorption Coefficient (RTE)	m^{-1}
λ	Wavelength (RTE)	nm
μ	Viscosity	N-s/m^2
υ_A	Stoichiometric Coefficient of Species A	None

ρ	Density	kg/m^3
ρ	Ratio of Rate of Side Chain Formation to Rate of Char Bridge Formation (CPD Model)	None
ρ_A	Density of Species A	kg/m^3
σ	Radiation Scattering Coefficient (RTE)	m^{-1}
σ	Optical Absorption Cross-Section	cm^2
σ	Fraction of side chains (CPD Model)	None
σ_t	Turbulent Transport Coefficient	None
τ	Viscous Stress	N/m^2
ω	Solid Angle	Steradians
ζ	Asphericity Correction Factor	None

Subscripts

0	Initial Conditions
D	Diameter
F	Fuel
H	Enthalpy
O	Oxidizer
P	Products
R	Reactants
a	Species A
b	Blackbody Radiation (RTE)
b	Bridge Breaking (CPD Model)
c	Raw Coal
f	Mixture Fraction
g	Bulk Gas Phase
gas	Light Gas Formation (CPD Model)
h	Char
l	Char Reaction Number (1 to l)
m	Volatiles Reaction Number (1 to m)
m	Mass
o	Oxidizer
r	Reaction
s	Surface
t	Turbulent Property
tar	Tar
v	Velocity
vol	Volatiles
w	Coal Moisture
λ	Constant Wavelength (RTE)

Superscripts

~	Favre-averaged Value
-	Mass-Weighted Averaged Value
→	Vector (implies direction)
’	Fluctuating Value

1. Introduction

One recently developed tool that has the potential to provide low-cost improvement in many scientific and engineering areas is computational fluid dynamics (CFD) modeling. CFD modeling is used to predict the performance of a wide variety of systems that involve flow, heat transfer, and/or chemical reactions. CFD modeling analysis is used to evaluate the performance of equipment and to design new equipment. This software is designed for accuracy, stability, adaptability, and to be user-friendly. Accuracy is evaluated by comparison of experimental data with CFD simulation predictions. For this reason, experimental data are needed to validate the accuracy of an initial CFD simulation.

This push for cost-effective improvement has led to the development of many commercial CFD software packages. These commercial packages include FLUENT, STAR-CD, CFX, FIDAP, and FLOW3D, plus several others not mentioned here. The on-going development and improvement of commercial CFD software has coincided with a decrease in code development at the university level. University-level CFD codes were originally developed for specific research applications. These applications included aerodynamics, turbomachinery, oil and gas recovery, coal combustion and gasification, and catalysis. While commercial CFD codes offer applications for a broader range of problems, these codes often lag behind university-level codes in advanced model development for specialized applications. For this reason, commercial CFD software companies often incorporate useful university-level subroutines into their codes.

Computational fluid dynamics analysis can broadly be divided into three main areas: (1) code development and improvement, (2) code application, and (3) code evaluation. Code development and improvement entails building submodels that describe important phenomena or numerical techniques that solve for important variables. In any given CFD code, there are hundreds of submodels that predict flow, turbulence, temperature, heat transfer, reaction kinetics, and many other variables. Code development and improvement also involves the verification of these codes to ensure their accuracy. Code application involves using computational fluid dynamics modeling to predict important variables such as velocities, pressures, temperatures, and species concentrations that occur throughout an apparatus. Code application typically involves the building of a geometric model for simulation, the selection of appropriate sub-models to be used with the simulation, and the convergence of the simulation. The last area of CFD analysis, code evaluation, involves analysis of model predictions to identify areas of a process or system for which improvement can be made. This also involves modeling the process with the improvements in order to quantify their effect on the overall process.

This research involved all three areas of CFD modeling applied to three separate projects:

- Solar CO_2 Conversion Modeling
- Improved Coal Combustion Modeling using STAR-CD
- Premixed Turbulent Combustion Data Compilation

These projects are described briefly in the following sections.

1.1 Solar CO_2 Conversion Modeling

Recently, solar energy has become a popular source of electricity because it is renewable and has a lower environmental impact than traditional power sources such as coal. However, little research has been done on using solar energy to produce a fuel, which may be a more economic use of solar energy. One possibility for producing a "solar fuel" was proposed by Jensen (Traynor and Jensen, 2002). They proposed the use of high-temperature chemistry using CO_2 to produce a solar fuel. Jensen and coworkers built a prototype solar CO_2 converter that uses sunlight to dissociate CO_2 into CO and O_2. The CO can then be used as a fuel or reacted with steam in a water-gas shift reaction to produce H_2.

This PhD project involved using CFD modeling to predict the performance of this prototype converter. Modeling this process involved predicting flow, heat transfer (conduction, convection, and radiation), and chemical kinetics. Results of the original model were evaluated to improve the converter performance. CFD modeling was performed to evaluate the impact of changes meant to improve converter performance. The overall goal of this project is to help make the solar-powered production of a fuel from CO_2 more economical.

1.2 Improved Coal Combustion Modeling Using STAR-CD

Coal has been used as a fuel for centuries and is the main fuel source for electric power generation in the United States. Recently, CFD modeling has led to many advances in coal combustion, including pollutant reductions and efficiency increases. One of the first 3-dimensional CFD codes used for modeling coal combustion, Pulverized

Coal Gasification and Combustion (PCGC-3) was developed by the Advanced Combustion Engineering Research Center (ACERC) located at BYU. This development involved the research of many faculty, staff, and students at BYU, as well as many individuals at other universities and institutions. These researchers developed and evaluated many coal models to predict numerous coal combustion phenomena. The intent of the development of PGCG-3 was to help the electric utility industry use CFD as a tool for plant optimization.

Over the years many advances in utility boiler design and retrofit have been made with the help of CFD analysis. Today, commercial CFD codes are popular in the power industry due to their graphical user interfaces, sophisticated grid/mesh capabilities, and numerical solution schemes. However, the coal combustion and gasification submodels in the commercial codes are not as advanced as those in PCGC-3.

This project involved modification of a commercial CFD software package, STAR-CD, to implement many of the modern PCGC-3 coal combustion submodels. These modified submodels were verified by comparison of submodel predictions and experimental data. This project also involved validation of STAR-CD with the implemented submodels by comparing overall CFD predictions to measured laboratory furnace data.

1.3 Premixed Turbulent Combustion Data Compilation

Natural gas is also used as a fuel source for power generation and heating. One benefit of natural gas combustion is its low pollutant emissions. One method for achieving low pollutant emissions is a combustion technique known as lean, premixed combustion. Numerous experiments were performed by Hedman and associates (Hedman, et al., 2005), in high intensity lean, premixed combustion environments. Velocity, temperature, and OH species concentration measurements were taken at many locations in a laboratory-scale gas turbine combustor (LSGTC) using advanced laser diagnostics. The laser diagnostic techniques included laser Doppler anemometry (LDA), coherent Anti-Stokes Raman Spectroscopy (CARS), and planar laser-induced fluorescence (PLIF). This extensive data set was taken over a period of 10 years by several students and only recently published. These data were never centrally compiled for analysis and distribution. These data were compiled into a central location, and have been made available on the internet.

1.4 Research Roadmap

The research on solar CO_2 modeling is to involve using CFD modeling as a tool to improve the performance of the solar CO_2 converter. This research is to involve the following steps:

- Develop and analyze a base-case model to predict performance of the experimental prototype.
- Perform parametric studies to better understand the limitations of the converter.
- Identify and evaluate potential adjustments meant to improve converter performance.

The research on improving the coal combustion modeling capabilities of STAR-CD is to involve implementing submodels developed for PCGC-3 into STAR-CD. This work is to involve the following steps:

- Modifying PCGC-3 submodels for implementation.
- Verifying the accuracy of the individual submodels.
- Validating the overall improvement of STAR-CD with the PCGC-3 coal submodels.

The research on turbulent premixed combustion is to involve compiling all the data taken on the LSGTC into a central location and making it available on the internet.

2. Literature Review

The following literature review summarizes general CFD modeling (Section 2.1), solar CO_2 conversion (Section 2.2), coal combustion and gasification modeling (Section 2.3), and premixed, turbulent combustion modeling (Section 2.4). These sections summarize previous experimental research, model development, and model evaluation efforts as they relate to this research.

2.1 Computational Fluid Dynamics Modeling

Computational fluid dynamics modeling was developed to predict the characteristics and performance of flow systems. Overall performance is predicted by breaking the flow system down into an appropriate number of finite volumes or areas, referred to as cells, and solving expressions representing the continuity, momentum, and energy equations for each cell. The process of breaking down the system domain into finite volumes or areas is known as mesh generation. The number of cells in a mesh varies depending on the level of accuracy required, the complexity of the system, and the models used. Equations solve for flow (x, y, and z velocities), energy (heat fluxes and temperatures), chemical reactions (reaction kinetics and species concentrations), and pressure based on various simplifications and/or assumptions. Some simplifications and assumptions are discussed below. If performed correctly, CFD modeling can accurately predict the performance of an entire system.

2.1.1 Flow (Velocity) Modeling

Flow can be modeled using a variety of algorithms depending on the type of flow (laminar or turbulent) and the desired level of accuracy. Flow predictions solve for x, y, and z velocities using the partial differential equations (PDE's) for the equation of motion and the continuity equation, found in Equations 2-1 and 2-2, respectively.

$$\rho \frac{D\vec{v}}{Dt} = -\nabla p - \left[\nabla \cdot \overset{=}{\tau}\right] + \rho \vec{g} + S_v^{part} \tag{2-1}$$

$$\frac{\partial \rho}{\partial t} + \left(\nabla \cdot \rho \vec{v}\right) = S_m^{part} \tag{2-2}$$

These PDE's contain source terms (S_v^{part} and S_m^{part}) that account for exchange between discrete and fluid phases. The PDE for the equation of motion is typically expanded into two or three PDE's, with each PDE calculating a specific dimensional velocity field. Each equation of motion contains a viscous stress term (τ) that is solved based on the fluid properties (viscosity) and conditions (laminar/turbulent). Each equation of motion contains a pressure term which necessitates solving the pressure field. Pressure is typically coupled to the equations of motion and the continuity equation using a technique known as the SIMPLE (**S**emi-**I**mplicit **M**ethod for **P**ressure **L**inked **E**quations) algorithm (Patankar, 1980). The SIMPLER, SIMPLEC, and SIMPLEST algorithms are various derivatives of the SIMPLE algorithm that provide alternative numerical coupling for the pressure field and the velocity fields.

Steady-state fluid flow profiles are typically solved using an Eulerian framework for both laminar and turbulent flow. An Eulerian framework solves for variables (velocities) assuming a continuum of fluid. Particle or droplet velocities are typically calculated in the continuum phase using a Lagrangian framework. Lagangian framework is also used to calculate transient fluid flow profiles. A Lagrangian framework solves for variables by tracking their individual movements over a series of time steps.

Laminar flow is fairly simple to model due to its structured flow patterns which are independent of time. Turbulent flow is inherently more complex, and several models have been developed to predict turbulent flow. These models have varying degrees of accuracy, which depend on the modeling assumptions.

Theoretically, the most accurate model for predicting turbulent flow is direct numerical simulation (DNS) (e.g. Bernard and Wallace, 2002). DNS is a time-dependent technique that attempts to capture all length and time scales of turbulence and their influence on the overall flow. Because of the computational time and resources needed, DNS has only been used to model simple turbulent flow systems. DNS is impractical for most systems, especially those where both heat transfer and chemical reactions occur.

Large eddy simulation (LES) is another turbulence modeling approach (e.g. Bernard and Wallace, 2002). It is similar to DNS in that it attempts to model time-resolved turbulent flow. LES directly calculates time-resolved turbulent eddies larger than a specific size. These eddies are assumed to be dependent on the system conditions. Smaller eddies are not directly calculated, but are modeled assuming that these smaller eddies correspond to isotropic turbulent eddies. LES also neglects the smaller time scales that are associated with the isotropic turbulent eddies. These simplifications enable LES calculations to be less computationally expensive than DNS. As computing resources have increased during the past 10 years, LES has become popular in some fields where predictions of time-resolved turbulent flow are important, but LES calculations still remain very time consuming.

Another category of turbulent flow models are commonly referred to as Reynolds-averaged Navier-Stokes (RANS) models. These models predict time-averaged turbulent flow properties based on various models and assumptions. These models are far less computationally intensive than either DNS or LES. Models in this category include the Reynolds stress model (RSM) (e.g. Launder, et al., 1975), the k-ε turbulence model (e.g. Launder and Spalding, 1972), the k-ω turbulence model (Wilcox, 1998), the Spalart-Allmaras turbulence model (e.g. Spalart and Almarus, 1994), as well as several other models.

The Reynolds stress model uses 7 PDE's to model turbulence: one equation for each Reynolds stress term ($\overline{u'u'}$, $\overline{u'v'}$, $\overline{u'w'}$, etc.). The k-ε turbulence model uses two PDE's to model turbulence: one equation that models turbulent kinetic energy and one that models turbulent dissipation. The k-ω turbulence model is similar to the k-ε model and models turbulent kinetic energy and specific turbulent dissipation. The Spalart-Allmaras turbulence model models turbulence using one equation that estimates turbulent viscosity. RANS models have been used in CFD simulations for over 30 years, and give reasonably accurate results for specific applications if properly applied.

2.1.2 Temperature (Heat Transfer) Modeling

Heat transfer is also important in many applications. To predict heat transfer is used to predict temperatures and heat fluxes the energy equation, shown in Equation 2-3 is solved.

$$\rho \frac{DH}{Dt} = -\left(\nabla \cdot \vec{q}\right) + \nabla \cdot \left(\frac{\mu_t}{\sigma_H} \nabla H\right) + S_H + S_H^{part} \qquad (2\text{-}3)$$

The energy equation contains a heat flux term (q) that is solved using the fluid properties and flow conditions. As seen in the energy equation, heat transfer is closely coupled to flow, and is typically solved using the same modeling approach used to solve for flow: laminar, DNS, LES, or RANS. The energy equation resolves both conductive and convective heat transfer and predicts temperature profiles and heat fluxes. The energy equation includes a source term for volumetric heat sources such as chemical reactions and radiation (S_H), as well as a source term that accounts for the exchange of energy between a discrete phase and a fluid phase (S_H^{part}).

Radiation is an important aspect of heat transfer. Radiation is solved using the radiative transfer equation (RTE) (e.g. Siegel and Howell, 2002), and is shown in Equation 2-4.

$$\frac{\partial I_\lambda}{\partial s} = \kappa_\lambda I_{b\lambda} - \beta_\lambda I_\lambda + \frac{\sigma_\lambda}{4\pi} \int_{4\pi} \Phi_\lambda(s_i, s) I_\lambda(s_i)\, d\omega_i \qquad (2\text{-}4)$$

This equation is used to solve for the radiation intensity in the s direction at a specific wavelength (I_λ), and contains terms for emission, absorption, out-scattering, and in-scattering. To calculate the overall radiation intensity, the RTE is solved over the applicable portion of the electromagnetic spectrum. The RTE is coupled with the energy equation through the emission and absorption terms.

Radiation can be solved using several different models, depending on the complexity of the system and the desired level of accuracy. The discrete transfer radiation model (e.g. Carvalho, et al., 1991), the P-1 radiation model (e.g. Cheng, 1964), the Rosseland radiation model (e.g. Siegel and Howell, 2002), the surface-to-surface radiation model (e.g. Siegel and Howell, 1992), and the discrete ordinates radiation model (e.g. Raithby and Chui, 1990 and Kumar, 1990) are the most commonly used radiation models. All of these models have been incorporated into various commercial CFD models.

2.1.3 Reaction Modeling

Another important feature of CFD modeling is the capability to describe reacting flow. Reacting flow kinetics can be modeled in several ways depending on the conditions of the system. Chemical reactions can occur either in the bulk fluid phase, or in a discrete phase, such as in a coal particle or on a catalyst surface.

Fluid-phase reactions are volumetric reactions, and can be modeled in several ways depending on the state of the flow (laminar or turbulent) and the inlet conditions. Each solution technique has trade-offs between accuracy and efficiency (solution time).

Gas-phase laminar-flow kinetics are solved using the finite rate model, which calculates reaction rates from Arrhenius parameters. A generic global finite reaction-rate expression is shown in Equation 2-5, with the Arrhenius Equation shown in Equation 2-6.

$$r_i = k\, C_i^n\, C_j^m \tag{2-5}$$

$$k = AT^b \exp\left(\frac{-E_a}{RT}\right) \tag{2-6}$$

In calculating reacting flow, all species fractions (species concentrations) in the flow are solved using species continuity equations for each species, shown in Equation 2-7, which accounts for diffusion, advection, overall reaction, and exchange between two phases.

$$\frac{D\rho_i}{Dt} = \nabla \cdot \left[D_{im}(\nabla \rho_i)\right] + MW_i r_i + S_i^{part} \tag{2-7}$$

This approach can be time-consuming, especially if multiple reactions occur or temperatures vary significantly, due to the stiffness of the species continuity equations and the energy equation. In addition, each involved species requires that a differential equation to be solved, increasing the required computational load of the CFD coder.

Turbulent reaction kinetics can be modeled in several ways: (1) the eddy-dissipation model (e.g. Magnussen and Hjertager, 1976), (2) the mixture fraction model (e.g. Libby and Williams, 1980), (3) the premixed reaction progress model (e.g. Zimont, et al., 1997), or the PDF transport model (e.g. Pope, 1985). Each of these modeling methods was developed for a specific type of turbulent reaction system (non-premixed/premixed), with various assumptions and limitations.

The eddy-dissipation model or eddy break-up model (e.g. Magnussen and Hjertager, 1976) is used to predict non-premixed, turbulent reacting flow. This model assumes that chemical reactions are limited by the turbulent mixing of reactants, and predicts reaction rates using empirical mixing correlations. For one reaction (involving species *i*), the mixing-limited reaction rates are shown in Equation 2-8.

$$r_i = \nu_i' \, MW_i \; A \, \rho \frac{\varepsilon}{k} \min\left(\frac{Y_O}{\nu_O'}, \quad \frac{Y_F}{\nu_F'}, \quad B\frac{Y_P}{\nu_P'} \right) \tag{2-8}$$

Equation 2-8 calculates the reaction rate based on the turbulent mixing of the limiting oxidizer, fuel, and products. This model uses component molecular weight (MW_i), component stoichiometric coefficient (ν_i'), all reactants (F for fuel or O for oxidizer) and product (P) mass fractions, molecular weights (MW), and stoichiometric coefficients (ν'), turbulent kinetic energy (k), turbulent dissipation rate (ε), and two empirical constants (A and B) to calculate the reaction rate. The two empirical constants are fitted according to experimental data, and have typical values of A=0.5 and B=4. This kinetic model is less time consuming than the finite-rate chemistry model (due to less stiffness between the species continuity equations and the energy equation), but still requires the calculation of each species fraction using species continuity equations. In addition, this model is closely coupled with turbulent calculations.

The mixture fraction model (e.g. Libby and Williams, 1980) also predicts non-premixed reacting flow. It assumes mixing-limited reactions, and that all chemical reactions proceed to equilibrium. The mixing rate is calculated using the same mixing correlations given in the eddy dissipation model. The equilibrium assumption enables the chemistry to be defined using two variables, the mixture fraction (f) and the mixture fraction variance (g). Typically, Favre-averaged values of mixture fraction ($\tilde{f}$) and mixture fraction variance ($\tilde{g}$) are calculated, according to the PDE's shown in Equations 2-9 and 2-10.

$$\frac{\partial}{\partial t}\left(\rho \tilde{f}\right)+\nabla\cdot(\rho\vec{v}\tilde{f})=\nabla\cdot\left(\frac{\mu_t}{\sigma_t}\nabla\tilde{f}\right)+S_f^{part} \tag{2-9}$$

$$\frac{\partial}{\partial t}\left(\rho \tilde{g}\right)+\nabla\cdot(\rho\vec{v}\tilde{g})=\nabla\cdot\left(\frac{\mu_t}{\sigma_t}\nabla\tilde{g}\right)+C_g\,\mu_t\left(\nabla\tilde{f}\right)^2-C_d\,\rho\frac{\varepsilon}{k}\tilde{g} \tag{2-10}$$

These PDE's solve for the Favre-averaged mixture fraction and mixture fraction variance using the fluid's turbulent properties (μ_t, σ_t, ε, k), source terms for exchange between two phases, and two empirical constants (C_g and C_d). All species fractions are calculated from equilibrium using the mixture fraction and the mixture fraction variance. The mixture fraction model requires solving only two partial differential equations, reducing the computational requirements for a CFD simulation versus the eddy-dissipation model or the finite-rate model. The mixture fraction model has been verified on non-premixed combustion systems, and has proven to give reasonably accurate species predictions.

The premixed reaction progress model (e.g. Zimont, et al., 1997) is used to describe turbulent premixed systems, and uses a single variable to describe the progress of the reaction from beginning to completion. This model attempts to simulate premixed chemistry by predicting the flame speed of the reaction and the turbulence. This model is challenging to apply properly to a simulation, and requires extensive knowledge of the reaction system (laminar flame speed, adiabatic flame temperature) and system turbulence.

The PDF transport model (e.g. Pope, 1985) predicts turbulent chemistry using probability density functions (PDF's) that define the chemical state of a system based on a combination of reaction kinetics and turbulence, and is used to describe premixed systems. A large number of fluid particle trajectories are solved in a Lagrangian framework to obtain a mean Eulerian solution for velocity, temperature, and species concentrations, as well as their corresponding statistics. The greatest advantage of this model is that turbulence/chemistry interactions are solved directly by the PDF transport model, and, therefore, chemical kinetics of any complexity can be incorporated without any turbulence/chemistry modeling assumptions (e.g. mixing limited, reaction-rate limited, infinite reaction-rates, etc.). This model has been extensively tested, and has been proven capable of predicting species concentrations in premixed combustors. However, this model requires a great deal more computational resources than any of the other kinetic models. It has also been tested on non-premixed combustion, and has proven to give reasonable results.

Discrete-phase heterogeneous reactions are modeled based on either (1) an nth order reaction rate expression or (2) a kinetic mechanism with surface reactions. For both cases, the reactant surface concentration is solved assuming the diffusion of reactant to the surface equals the overall destruction of the reactant due to the surface reaction.

Heterogeneous reactions are limited by reaction rates at the surface, diffusion of reactants to the surface, or a combination of the two. Source terms are necessary to account for exchanges (mass, species, heat) between the discrete phase and the fluid phase.

All the reaction models discussed are summarized in Table 2-1. This table lists the typical applications for each reaction model, its limitations, the comparative computational resources required, and the accuracy typically achieved by each model.

Table 2-1. Summary of reaction models.

Model	Applications	Assumptions	Accuracy
Finite-Rate Chemistry	Laminar/Turbulent, Non-premixed, Gas-Phase	Reaction-Rate Limited	± 10%
Eddy Dissipation	Turbulent, Non-premixed, Gas-phase	Mixing Limited, Mixed Is Burnt	± 15%
Mixture Fraction	Turbulent, Non-premixed, Gas-phase	Mixing Limited, Equilibrium	± 10%
Reaction Progress	Turbulent, Premixed, Gas-phase	Equilibrium	± 20%
PDF Transport	Turbulent, Premixed, Gas-phase	Known Kinetic Mechanism	± 10%
Surface Chemistry	Discrete-phase	Diffusion = Reaction	± 10%

2.2 Commercial CFD Codes

A brief review of the three CFD codes (FLUENT, STAR-CD, PCGC-3) used in this project is provided in this section, with emphasis given to strengths and weaknesses.

2.2.1 FLUENT

FLUENT was originally developed by Swithenbank, et al. (Boysan, et al., 1981) and extended by FLUENT Inc., headquartered in Lebanon, New Hampshire. Two main programs are necessary to perform a CFD simulation using FLUENT: Gambit and

FLUENT. Gambit is used for geometry creation and meshing, and FLUENT performs the remainder of the set-up, calculations, and post-processing. FLUENT has hundreds of options for materials (gas, liquid, and solid), material properties, flow (laminar and turbulent), heat transfer (conduction, convection, and radiation), reacting flow, boundary conditions, and solution techniques. Completed simulations can be displayed graphically or in a data-output file.

FLUENT is one of the most popular CFD codes, and is used in a wide variety of applications. It is fairly easy to learn, and has helpful guides (FLUENT, 2007) that explain most of its options. It is also the most robust of the three codes, meaning it very seldom crashes or has unexplained errors. One drawback to FLUENT is the difficulty in meshing complex geometries in Gambit. It is not uncommon to spend more time in the creation of a geometry and mesh in Gambit than the remainder of the simulation in FLUENT (set-up, iteration, post-processing). Another disadvantage is the difficulty in implementing user-defined functions and subroutines into the code.

2.2.2 STAR-CD

STAR-CD was originally designed by Gosman (1998) and is supported by the CD-adapco Group based in Melville, New York. STAR-CD has three distinct CFD codes: pro-STAR, STAR-Design, and STAR-CCM+. Pro-STAR has tools to create the geometry/mesh, to run, and to post-process a CFD simulation. Pro-STAR has similar capabilities and options as FLUENT but is more difficult to use. It requires complex geometries to be created using a CAD package (e.g. SolidWorks). STAR-Design is a much simpler CFD code, and was designed for the novice "design" engineer. It is capable of simulating systems involving flow and heat transfer. STAR-Design has two benefits.

First, it is extremely simple to create, analyze, and display simple CFD simulations. Second, it has a CAD-style geometry creation, which enables fairly easy creation and meshing of complex geometries. The created simulations can then be solved using STAR-Design or transferred into pro-STAR for solution. A next-generation CFD code, STAR-CCM+, is also provided by CD-adapco. This CFD code simplifies meshing and running CFD simulations and has the same capabilities as pro-STAR.

STAR-CD's CFD codes (pro-STAR, STAR-Design, STAR-CCM+) can be used to model a wide range of systems in various areas. One advantage is the succinct organization for set-up of a simulation. The last major advantage is the ease in implementing user-defined subroutines. STAR-CD provides a template for writing various user-defined subroutines. One drawback to STAR-CD is the difficulty in learning the nuances (switches and constants) of the code. In addition, the code is prone to crash or have unexplained errors. The error messages often provide no help in determining the exact cause of the error or how to fix it.

2.2.3 PCGC-3

Pulverized Coal Combustion and Gasification, 3-D (PCGC-3) was developed by ACERC personnel at BYU from 1979 to 1999 (Hill and Smoot, 1993, and Smoot and Smith, 1985). PCGC-3 was initially designed to model reacting flow systems, especially turbulent combustion systems. PCGC-3 has fewer options than FLUENT and STAR-CD, but still can model many important systems, including coal combustion systems.

There are two main advantages of PCGC-3 versus the other codes. First, the source code is available to the user. This enables code alterations for specialized applications. Second, PCGC-3 has advanced submodels for describing combustion.

PCGC-3 also has several drawbacks, including difficulty in creating geometries, especially complex geometries, limited numerical algorithms, and unexplained errors. Also, PCGC-3 is not a commercially supported code as are FLUENT and STAR-CD.

2.3 Solar CO_2 Conversion Modeling

Harnessing solar energy can provide some of society's global energy needs without a net production of greenhouse gases. One problem associated with solar energy is the fact that geographical areas of high solar intensity (i.e. the Sahara Desert) are often far from population centers (i.e New York City), and, therefore, are not easily utilized. Another obstacle to the utilization of solar energy is the low efficiency and high cost of photo-voltaic cells. For these reasons, some recent research has focused on using solar energy to produce transportable fuels. These fuels are synthesized on site and then transported to other locations where needed.

Kodama (2003) compiled research on several methods for the conversion of solar energy to chemical fuels, including water splitting for the production of H_2, steam or CO_2 gasification of coal, steam or CO_2 reforming of methane, and hydrogenetive coupling of methane. All these processes involve 3 steps: 1) the absorption and conversion of solar radiation to thermal energy (heat) using a reflector-collector and receiver-reactor system, 2) the use of heat to drive an endothermic reaction scheme in various working fluids, either with or without a catalyst, and 3) the extraction of the desired products. Kodama concluded that solar reforming of methane was the most viable option for producing a usable fuel using solar radiation. He also concluded that more research was needed because typical industrial processes and materials were not suitable for the conversion of solar energy to fuel due to high thermal flux densities and frequent thermal transients, characteristics of solar radiation. The possibility of using CO_2 as a working fluid to produce fuel was not considered in Kodama's review.

Jensen, et al. (1997) hypothesized that the photolysis reaction of CO_2 shown in Reaction 2-1 could produce a significant amount of CO at high temperatures (> 2000 K).

$$CO_2 + h\nu \rightarrow CO + O \qquad \text{(Reaction 2-1)}$$

This hypothesis was based on the spectral absorption profile of CO_2. Carbon dioxide has negligible spectral absorptivity in the visible and near-ultraviolet regions below 1500 K. However, the spectral absorptivity increases substantially between 1500 K and 3000 K. This increased absorptivity enables hot CO_2 to directly absorb radiation, and then to dissociate to CO and O if the radiation ($h\nu$) is of the correct energy level. This photolysis reaction occurs in addition to thermochemical reactions involving CO_2.

Jensen (Lyman and Jensen, 2001) also performed simple 1-dimensional calculations and determined that a process using high-temperature CO_2 could feasibly produce a product gas of CO_2, CO, and O_2 by quickly quenching photolyzed mixtures of CO_2, CO, and O using either cold CO_2 or a cold mixture of CO_2 and H_2O. Quenching was calculated using a reaction mechanism developed by Yetter, et al. (1995). Species mole fractions were used as initial conditions, and 1-D premixed laminar-flow calculations were performed using CHEMKIN II (Kee, et al., 1996) to solve for species fractions as the mixture was quenched. The cooling rates for the gas mixture were estimated from the amount of excess gas used to quench. Quenching the hot gas mixture stream with a CO_2

stream (at 500 K) with 3.54 times the flow rate of the hot stream proved to be most effective based on (1) the minimization of the impact of reverse reactions to CO_2, and (2) the prevention of excessive dilution. Calculations were also performed using H_2O/CO_2 mixtures to quench the same high-temperature CO_2 product mixtures. These calculations predicted that nearly all of the CO formed would remain in the product stream if the photolyzed CO_2 mixtures were cooled using either pure H_2O or 10 mol% H_2O and 90 mol% CO_2 at a flow rate 5 times that of the hot mixture.

Jensen (Traynor and Jensen, 2002) next developed a process that uses CO_2 as a working fluid to produce a fuel (CO) from solar energy. A prototype production facility was built by Los Alamos Renewable Energy Corporation that consists of a reflective mirror system, a conical silver reflector, a quartz window, a zirconia (ZrO_2) rod, and supporting equipment. The overall prototype apparatus schematic is shown in Figure 2-1. Photos of the apparatus and CO_2 converter are shown in Figure 2-2 and Figure 2-3.

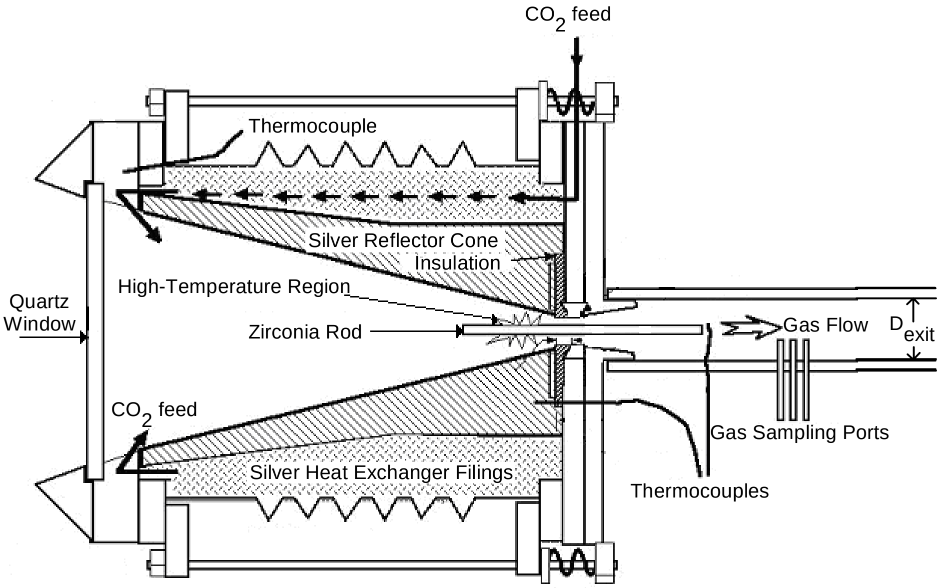

Figure 2-1. Schematic of the prototype CO_2 converter.

Figure 2-2. Photo of the solar collector and CO_2 converter device.

Figure 2-3. Photo of the CO_2 converter device.

Solar energy was used to radiatively heat the zirconia rod located in the throat of the silver reflector cone to temperatures in excess of 2600 K. High solar radiation intensities were achieved using the parabolic reflective mirror system and the conical silver reflector cone to concentrate sunlight on the zirconia rod. The silver cone and zirconia rod were enclosed using a quartz window. This window allowed transmission of solar energy into the apparatus with minimal transmission losses. Carbon dioxide was passed over the hot zirconia rod and thermally dissociated and photolyzed into CO and O. Downstream of the throat and zirconia rod, the $CO_2/CO/O_2/O$ mixture was quenched to prevent reverse reactions of CO to CO_2. The quenching was accomplished by air cooling the exhaust pipe, and, in some cases, by CO_2 cooling gas jets located downstream of the zirconia rod. Experiments using a first-generation prototype yielded 4-6 mol% CO in the cooled product stream, with an estimated peak yield of 12-15 mol% CO in the throat, when operated at a flow rate of 10.0 L/min STP (slpm).

The species in the product stream can be separated, and the CO used as a fuel or converted to H_2 through the water-gas shift reaction. The separation of the $CO_2/CO/O_2$ mixture was studied by Foster (2006). His research focused on liquid absorption of CO using aqueous cuprous chloride (CuCl) and magnesium chloride (Mg_2Cl).

The overall thermochemical reaction of CO_2 to CO and O_2 is described using the three reversible elementary reactions listed below. In these reactions M represents a third body needed for the reaction to occur, meaning any species.

$$CO_2 + M \leftrightarrow CO + O + M \qquad \text{(Reaction 2-2)}$$

$$CO + O_2 \leftrightarrow CO_2 + O \qquad \text{(Reaction 2-3)}$$

$$O_2 + M \leftrightarrow O + O + M \qquad \text{(Reaction 2-4)}$$

Tsang and Hampson (1986) compiled kinetic parameters for hundreds of elementary reactions that are important in combustion and gasification. The reaction-rate coefficients for the forward and reverse reactions of Reactions 2-3 and 2-4, and the reverse reaction of

Reaction 2-2 were listed. No kinetic parameters were found for the forward reaction of Reaction 2-2, but this can be calculated using equilibrium and the reverse reaction rate.

The research of Jensen focused on experimental work based on theoretical physics and chemistry, as well as simple modeling. To thoroughly understand the performance of the prototype CO_2 converter, detailed CFD modeling was required. This modeling identified potential ways to improve the performance of the CO_2 converter and quantify the impact of those improvements.

2.4 Improved Coal Combustion Modeling Using STAR-CD

PCGC-3, (Hill and Smoot, 1993) described earlier, was specifically developed to model entrained flow combustion and gasification and has many advanced coal combustion and gasification subroutines. Commercial CFD codes have more advanced numerical algorithms, superior gridding methods, and better graphical user interfaces than PCGC-3, but typically include very simple and limited "coal-related" submodels.

To improve the capabilities of a commercial code, it was decided to implement PCGC-3's coal submodels into STAR-CD. PCGC-3 has submodels for the physical and chemical parameters associated with coal, various coal reactions, pollutant emissions, and particle deposition. The physical and chemical coal parameters describe coal, and include its ASTM ultimate and proximate analyses.

2.4.1 Original STAR-CD Submodels

STAR-CD was built as a general-purpose CFD code, with a wide range of capabilities to model various industrial systems. STAR-CD is used by several industries, including aerospace, automotive, chemical process, and power generation. To simulate systems and equipment in all these areas, as well as many others, STAR-CD needs many specialized submodels. For example, to simulate a coal-combustion system, submodels need to simulate the following phenomena: (1) heat transfer models to predict conduction, convection, and radiation; (2) chemical reaction models to predict coal reactions and gas-phase reactions; (3) flow models to predict velocity profiles; and (4) 2-phase models to predict interactions and exchanges between the gas and the coal particles. Most of the models needed for coal combustion are used in related systems and are fairly common. A key area in coal combustion where specialized models are required is modeling coal and its chemical reactions. STAR-CD had limited capabilities to model coal combustion previous to this collaborative effort between ACERC and CD-adapco.

The original coal set-up procedure used in STAR-CD described coal using its ultimate and proximate analysis. Proximate analysis describes coal in terms of fractional amounts of volatile matter, moisture, fixed carbon, and ash in the coal. These results are typically obtained from experimental results for individual coal types. Ultimate analysis describes the dry, ash-free portion of coal in terms of its elemental composition, as determined from experimental results. STAR-CD includes carbon, hydrogen, oxygen, and nitrogen in its ultimate analysis. Other variables describing coal in STAR-CD are the coal net calorific value, also known as the higher heating value (HHV), coal radiative properties (emissivity, reflectivity, etc.) and the fraction of total nitrogen in the volatiles.

Coal reaction submodels that were available in STAR-CD previous to the collaborative efforts between ACERC and CD-adapco included two devolatilization submodels: a constant-rate devolatilization submodel and a 1-step devolatilization submodel, and three char oxidation submodels: a constant-rate char burnout submodel, a 1st-order char burnout submodel, and a ½-order char burnout submodel. The constant-rate devolatilization submodel describes devolatilization using two parameters: the overall volatile matter content of the coal and a user-defined devolatilization time. The rate of devolatilization is constant over the devolatilization time such that the volatiles are released evenly throughout the devolatilization time. The 1-step devolatilization submodel describes devolatilization as a single 1st-order reaction with rate constants that follow a simple Arrhenius reaction-rate expression. The reaction is first order with respect to the amount of volatiles remaining in the coal. This model requires three parameters: the overall volatile content of the coal, a pre-exponential factor, and an activation energy.

The constant-rate char oxidation submodel is similar to the constant-rate devolatilization submodel and describes char burnout using two parameters: overall char content of coal and char-burnout time. The first-order char burnout submodel calculates the rate of char burnout by calculating the rate-limiting process, which can be either the diffusion of oxygen to the char surface or the reaction of oxygen at the char surface. The surface reaction is assumed to be first order with respect to oxygen. The char burning rate is also dependent on the char surface area, the concentration of oxygen in the free stream, and the particle temperature. Parameters needed for this model include the overall char fraction of the coal, the pre-exponential factor for the char reaction, and the activation energy of the char reaction. The ½-order char oxidation model is exactly the same as the 1st-order char oxidation model except that the surface reaction of oxygen with char is assumed to be ½ order with respect to oxygen.

2.4.2 PCGC-3 Coal Submodels

Coal particle reactions are modeled assuming three distinct reaction pathways: moisture vaporization, devolatilization, and char oxidation. Moisture vaporization is modeled for liquid which is either in the coal or is an ingredient in a coal-water slurry. Devolatilization is predicted using one of 3 models: the one-step model (Anthony, et al., 1975), the two-step model (Kobayashi, et al., 1976), or the chemical percolation devolatilization (CPD) model (Grant, et al., 1989). Char oxidation is modeled based on surface reactions of char with various oxidizers that have diffused to the particle surface. Two char oxidation models are available in PCGC-3: an nth-order char reaction model (Smith, et al., 1994), and the carbon burnout kinetic (CBK) model (Hurt, et al., 1998). Nitrogen pollutant emissions are also modeled in PCGC-3 (Hill and Smoot, 2000). Subsequent versions of PCGC-3 have also included submodels to predict ash deposition (Wang and Harb, 1997), soot formation (Fletcher, et al., 1997), and a two parameter coal-gas mixture fraction model (Flores and Fletcher, 2000). These submodels are described below.

2.4.2.1 Coal Setup and Initialization

The coal setup and initialization subroutine allows a user to specify the parameters that describe coal and all coal reactions that occur during coal combustion and gasification. The coal is described by its elemental composition determined from ASTM ultimate analysis, its composition calculated from proximate analysis, and its structural parameters determined using ^{13}C NMR analysis. The ^{13}C NMR analysis is used in the CPD model to describe the matrix-like chemical structure of coal. This subroutine defines the higher heating value of the coal using either a user-specified value, or a correlation based on the elemental composition of the coal. This subroutine enables a user to specify which devolatilization and char oxidation submodels to use and the reaction-rate parameters for those submodels. All these parameters are in an input file named Coal0.in.

2.4.2.2 Moisture Vaporization

The water vaporization model calculates the rate at which moisture in the coal is vaporized. Water vaporization is predicted to occur prior to devolatilization and char oxidation, and may occur at temperatures below the boiling point of water. Moisture vaporization is modeled using either a boiling correlation or an evaporation correlation, depending on the conditions (e.g. Turns, 2000). Vaporization is limited either by heat transfer or mass transfer. Mass-transfer limited vaporization is modeled based on a gradient-driven evaporation correlation (see Equation 2-11 in Table 2-2). The surface water vapor mass fraction is calculated assuming it is in equilibrium with the liquid phase. Gradient-driven evaporation is based on convection of water vapor from the coal into the gas phase, and is calculated using a convective mass transfer coefficient (k_w). Heat-transfer limited vaporization is calculated based on an overall heat balance at the particle temperature (see Equation 2-12 in Table 2-2). Molecular diffusion of water vapor is assumed to be negligible compared to convection. The overall water vaporization is based on the heat flux to the particle (q), the heat of vaporization (q_r), the calculated convective flux of water vapor away from the surface, and an asphericity factor (ζ). The overall vaporization rate is the lesser of the two calculated values.

Table 2-2. PCGC-3 particle coal reactions.

Description	Equation	Reference
Moisture vaporization rate (Mass-transfer limited)	$r_w = \dfrac{S_f\, SA\, k_{cw}\, \rho_w (x_{w,s} - x_{w,g}) + x_{w,s} \sum_m S_f\ r_{vol,m}}{1 - x_{w,s}}$	2-11
Moisture vaporization rate (Heat-transfer limited)	$r_w = \dfrac{-Q + Q_r + r_{coal}(h_g - h_c)\zeta + r_h \zeta (h_g - h_h)}{\zeta (h_g - h_w)}$	2-12
Net reaction rate to the gas phase	$r_{coal} = \sum_m r_{vol,m} + \sum_l r_{hl} + r_w$	2-13
Volatile production rate	$r_{vol,m} = k_m Y_m \alpha_m$	2-14
Volatile kinetic rate coefficient	$k_m = A_m \exp\left({-E_{a,m}} \big/ {RT} \right)$	2-15
Labile bridge reaction rate	$-\dfrac{d\pounds}{dt} = -k_b \pounds$	2-16
Side chain reaction rate	$-\dfrac{d\sigma}{dt} = \dfrac{2\rho k_b \pounds}{\rho + 1} - k_{gas} \rho$	2-17
Char bridge reaction rate	$-\dfrac{dc}{dt} = \dfrac{k_b \pounds}{\rho + 1}$	2-18
Volatiles fraction (CPD model)	$f_{vol} = f_{tar} + f_{gas}$	2-19
Tar fraction (CPD model)	$f_{tar} = \dfrac{2}{2 + r(1 - c_0)(\sigma + 1)} \left[\Phi F(p) + r \Omega K(p) \right]$	2-20
Light gas fraction (CPD model)	$f_{gas} = \dfrac{r\, g(\sigma + 1)}{4 + 2r(1 - c_0)(\sigma + 1)}$	2-21
Char production rate	$r_{h,m} = {r_{vol,m}(1 - Y_m)} \big/ {Y_m}$	2-22
Net char reaction rate	$r_h = \sum_m r_{h,m} - \sum_l r_{h,l}$	2-23
Oxidizer-char reaction rate (nth order)	$r_{h,l} = \dfrac{SA^2 MW_h MW_g \phi k_{ch} k_l \zeta C_{og,l}^{n,l} C_g}{MW_g\, SA\, C_g (\zeta k_l - k_{ch}) + r_{coal}}$	2-24
Kinetic char reaction-rate coefficient	$k_l = A_l T^b \exp\left({-E_{a,l}} \big/ {RT} \right)$	2-25
Mass transfer coefficient	$k_{ch} = \dfrac{Sh_g D_{im} B_{ji}}{d(\exp(B_{ji}) - 1)}$	2-26
Transpiration parameter for mass transfer	$B_{ji} = \dfrac{r_{coal}}{2\pi D_{im} \rho_g d}$	2-27
Oxidizer-char reaction rate (CBK model)	$r_{h,l} = \eta \dfrac{SA^2 MW_h MW_g \phi k_{ch} k_l \zeta C_{og,l}^{n,l} C_g}{MW_g\, SA\, C_g (\zeta k_l - k_{ch}) + r_{coal}}$	2-28

2.4.2.3 Devolatilization

The one-step devolatilization model (Anthony, et al., 1975) calculates the devolatilization rate of coal, and is based on one global reaction describing the reaction of coal. This model assumes the devolatilization pathway found in Reaction 2-5, with Y representing the volatiles/char split. Coal reacts to form volatiles, which are released into the gas phase, and char, which remains with the coal and reacts further during char oxidation. All necessary equations for calculating the devolatilization rate are found in Equations 2-14 and 2-15 in Table 2-2. This reaction has kinetics based on an Arrhenius reaction-rate expression calculated using coal-specific devolatilization data. This reaction-rate expression is used in source terms in the continuity, momentum, and energy equations to relate the mass released from the particle phase and gained by the gas phase. These models are fairly accurate in predicting devolatilization behavior, but provide little insight into the physical and chemical processes associated with devolatilization.

$$\text{Coal} \rightarrow (\text{Y})\ \text{volatiles} + (1\text{-Y})\ \text{char} \qquad \text{(Reaction 2-5)}$$

The two-step devolatilization model (Kobayashi, et al., 1976) also calculates the fractions of coal, char, and volatiles released from a coal particle. The two-step devolatilization model is similar to the one-step model except that this model assumes the devolatilization pathway found in Reaction 2-6. Both competing reactions are first order with respect to the unreacted coal, and have kinetic parameters that follow simple Arrhenius reaction-rate expressions. The devolatilization reaction rate is calculated using the same equations as the one-step model (Equations 2-14 and 2-15 from Table 2-2). Increased accuracy is obtained using the two-step model over the one-step model, since this model is more complex. Both models cannot account for the effects of pressure on devolatilization, and neither can predict light gas or tar in the volatiles.

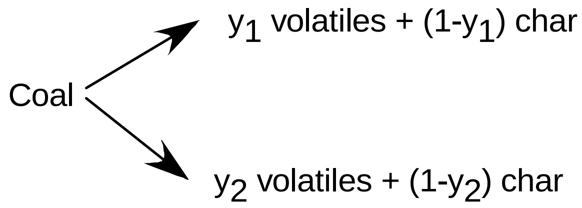

(Reaction 2-6)

The chemical percolation devolatilization (CPD) model (Grant, et al., 1989, Fletcher, et al., 1990, Fletcher, et al., 1992) also calculates the break-up of coal to form volatiles and char. This model is more complex than the one-step and two-step devolatilization models. This model predicts the overall volatiles yield and the volatiles distribution characteristics of coal. The model uses a lattice structure, determined from ^{13}C NMR analysis, to describe the chemical structure of coal, and various reactions to describe the conversion of coal to the devolatilization products of light gas, tar, and metaplast. Light gas, tar, and metaplast are classified based on their origin and physical state. The difference between tar and metaplast is that tar vaporizes after its release from the lattice, whereas metaplast remains as a liquid. Three reactions, shown in Reactions 2-7 through 2-9, describe the devolatilization of coal using the fractional number of labile bridges (£), fractional number of reactive bridge intermediates ($\pounds^*$), fractional number of char bridges (c), and fractional number of side chains (δ).

$$\pounds \rightarrow \pounds^* \qquad \text{(Reaction 2-7)}$$

$$\text{£}^{*} \rightarrow c + 2g_2 \qquad \text{(Reaction 2-8)}$$

$$\text{£}^{*} \rightarrow 2\delta \qquad \text{(Reaction 2-9)}$$

Each of these reactions is described by a first-order distributed activation energy reaction-rate equation with Arrhenius kinetic parameters, shown in Equations 2-16 through 2-18 of Table 2-2. These equations use a steady-state approximation for the reactive bridge intermediate fraction. A vapor-liquid equilibrium flash calculation is performed using the Rachford-Rice method (1952) to determine the tar and metaplast distribution of the products. This flash calculation allows the CPD model to predict the effects of pressure on devolatilization.

The CPD model was verified by comparison of predictions and experimental volatiles and tar yields for various heating rates and pressures (Grant, et al. 1989). Good agreement (<5%) was achieved between predictions and experimental volatiles and tar yields for several coals, including coals not used in determining the kinetic parameters. This model calculates the overall fraction of coal devolatilized based on the solution of the three reaction rates, and is calculated using Equations 5-19 through 5-21. All parameters in these equations are solved from the reaction-rate solutions or from algebraic expressions.

2.4.2.4 Char Oxidation

The global nth-order char reaction submodel (e.g. Smith, et al., 1994) can be used to calculate the char reaction rate. This submodel assumes that char reacts heterogeneously with various gas-phase oxidizers according to Reactions 5-6 to 5-8.

$\text{Char} + \frac{1}{2} O_2 \rightarrow CO$ (Reaction 5-6)

$\text{Char} + CO_2 \rightarrow 2\ CO$ (Reaction 5-7)

$\text{Char} + H_2O \rightarrow H_2 + CO$ (Reaction 5-8)

These reactions follow the extended reaction-rate expression shown in Equation 2-24 from Table 2-2. The oxidizers diffuse from the bulk to the char surface and react. The global nth-order char reaction model is similar to the char burnout model already available in STAR-CD; it calculates the char reaction rate as the limiting process for the char reaction, either the diffusion of oxidizer to the char surface or the reaction of oxidizer at the char surface. Each surface reaction is nth order with respect to the oxidizer, with typical reaction orders (n) ranging from 0.5-1.0. The reaction order for surface reactions is determined using an experiment where the surface reaction is limiting. Kinetic parameters for each char reaction have been experimentally determined for various ranks of coal (Goetz, et al., 1983).

The diffusion portion of the reaction rate contains a term to account for the effects of transpiration (B_{ji}). This parameter accounts for lower heat transfer to the particle that results from blowing from water evaporation and devolatilization. The total reaction rate is the sum of the three overall char reactions. Because the char reaction is a surface reaction, its rate is dependent on the char surface area (SA). The total char surface area is assumed to equal the external surface area of the char sphere multiplied by a parameter, ζ, which accounts for the effects of particle pores and asphericity on the total char surface area. This model assumes a shrinking sphere model, so the diameter of the char particle decreases as the char reacts. All the equations necessary to calculate the char oxidation are found in Equations 2-22 through 2-27 of Table 2-2. Char oxidation requires source terms that relate the exchange of mass and heat between phases. While the simple char oxidation model is accurate in modeling the majority of char oxidation, it fails to accurately predict late carbon burnout, where other phenomena become important.

Another model used for predicting char oxidation is the char burnout kinetic (CBK) model (Hurt, et al. 1998). This model was developed to accurately predict overall carbon burnout (including late carbon burnout) in industrial furnaces. The increased accuracy of this model is due to extensive modeling of late-stage burnout, which is characterized by decreased char reactivity and increased heat and mass transfer resistance due to ash inhibition. Decreased char reactivity is thought to be due to a combination of carbon-mineral interactions, thermal deactivation, and preferential consumption of the more reactive char components.

The CBK model uses either 1) an intrinsic nth order reaction model with rank-dependent kinetics, or 2) a 3-step elementary reaction mechanism with appropriate kinetics to predict burnout. Char reactivity is described using a thermal deactivation submodel that predicts the thermal annealing of char which leads to lower char reactivity. Char is assumed to be annealed by a first-order reaction that follows an Arrhenius rate expression. The CBK model also has an ash inhibition submodel. This submodel evaluates various overall physical parameters of the char-ash particle by calculating the combined effects of an outer ash layer and an inner char-rich core. The CBK model also accounts for the various modes of particle burning by calculating the Thiele modulus.

The CBK model uses the same equations to calculate char oxidation as those used in the global nth-order reaction model (Equations 2-22-2-27 in Table 2-2), but the three CBK subroutines calculate a combined factor (η) that is added to the oxidizer char reaction-rate equation. This updated equation is shown in Equation 2-28 in Table 2-2. The CBK predictions were verified with data obtained from char oxidation experiments (Hurt, et al, 1998), with the CBK model predicting burnout within 5% throughout combustion. These data included conditions typical for a commercial facility.

2.4.2.5 NO_X Emissions

PCGC-3 also has the capability to predict nitrogen pollutant emissions (NO_X) from coal combustion facilities (Hill and Smoot, 2000). Thermal NO_X is modeled using the Zeldovich mechanism. Prompt NO_X is modeled using a simple correlation because detailed hydrocarbon chemistry is currently computationally unrealistic for large-scale simulations. Fuel NO_X is modeled in turbulent systems based on coal-nitrogen evolution into the gas phase. Fuel nitrogen is assumed to evolve from coal into the gas phase as HCN which reacts in the gas phase to form either NO or N_2 depending on the local gaseous conditions. The nitrogen in coal is assumed to be released from the coal in proportion to its total mass loss. NO and HCN are modeled in turbulent systems by an extent of reaction (π) that relates the actual concentration at a particular condition to the predicted thermodynamic equilibrium concentration at that same condition. A simplified mechanism is used to describe NO_X chemistry from HCN. Because both NO and HCN are minor species, NO_X species predictions are solved using converged CFD calculations.

Using profiles for temperature, the coal-gas mixture fraction, and oxygen, the NO and HCN profiles are calculated using: 1) the π's for HCN and NO, 2) the reaction kinetics for NO_X chemistry, and 3) an O_2 species balance. This model has improved predictions for NO_X concentrations in several industrial systems (Hill and Smoot, 2000), although predictions and data frequently vary. This approach is only accurate for turbulent combustion systems, and is closely coupled with the mixture fraction approach.

2.4.2.6 Ash Deposition

A model for predicting ash deposition is also available in PCGC-3 (Wang and Harb, 1997, Wang, et al., 1999). Deposition modeling is used to predict problematic areas of deposition, predict changes in heat flux caused by deposit growth, predict the most efficient timetable for soot blowing, and assess the feasibility of new boiler designs. Calculating deposition involves calculating the following: (1) ash formation from coal, (2) particle transport, (3) particle impaction, and (4) particle sticking. These parameters are used to solve for deposit growth and important deposit properties such as thermal conductivity, porosity, emissivity, and phase composition. These deposit properties are used to predict the local heat transfer through the deposit, and the effects of the deposit on overall operating conditions. All local parameters, such as gas and particle temperatures and particle density, are predicted using a converged CFD simulation. Particle impaction rates are modeled using a statistical particle cloud model, which characterizes a specific number of particles using a probability density function. Particle sticking and deposit growth are predicted based on the local incident heat flux, the local particle impaction rate, and the ash size and composition. The deposition model predicts local transient deposition rates using a converged steady-state CFD solution, and these deposition rates are used to calculate any changes in local boundary conditions that are then applied to the next steady-state CFD simulation. Several steady-state CFD solutions are linked to predict time-resolved boiler performance and deposition. This model was used to predict deposition in both a laboratory-scale facility (Thornock and Borion, 1992) and a commercial utility boiler (Cannon, et al., 1993). Decent agreement (<20%) was achieved between (a) the model predictions for local deposit growth and local heat transfer rates and (b) the experimentally determined local deposition rates and heat transfer rates.

2.4.2.7 Soot

PCGC-3 also contains a model for predicting soot formation (Fletcher, et al., 1997, and Brown and Fletcher, 1998). Soot formation occurs in fuel-rich regions by condensation and polymerization reactions of hydrocarbons. Tar is believed to be the main precursor of soot in coal combustion systems. Soot formation is important in combustion systems because of its effect on the energy balance, especially in near-burner regions of commercial combustion facilities where radiation is the dominant mode of heat transfer. The modeling of coal-derived soot involves three variables: the soot mass fraction, the tar mass fraction, and the number of soot particles per unit mass. Each of these parameters is solved using a transport equation, with source terms for each equation being derived from devolatilization, polymerization, gasification, and oxidation reactions involving tar and soot. Devolatilization is solved using the CPD model. All other reactions use reaction rates obtained from literature. Several radiative soot properties are estimated including emissivity, absorptivity, and the scattering phase function. Predictions made with the soot model were compared to experimental data, as well as to predictions made without this model. Good agreement (±10%) was achieved between the soot model predictions and data available on soot size, soot particle density, gas temperature, and NO_X concentrations (Brown and Fletcher, 1998). Comparison of the predictions made with and without the soot model showed that the inclusion of the soot model lowered the predicted local gas temperature in the flame zone by as much as 300 K, and lowered the predicted NO_X concentration by as much as 250 ppm.

2.4.2.8 Turbulence-Chemistry Modeling

Another model available in PCGC-3 is the 2-η coal-gas mixture fraction model (Flores and Fletcher, 2000). The 2-η coal-gas mixture fraction model tracks coal products based on whether they are the result of devolatilization or char oxidation. This model allows for different initial coal off-gas compositions from the coal based on whether the off-gas is the result of devolatilization or char oxidation. Devolatilization off-gas is known to have greater concentrations of hydrogen, nitrogen, and oxygen than off-gas from char oxidation. One advantage of the 2-η model is its ability to predict coal-nitrogen release, and thus more accurately predict fuel NO_X. This model was validated by comparison of predictions to experimental data, and by comparison of predictions made using the 2-η model and the 1-η model. Predicted temperature and major species concentration for both models were nearly identical and matched experimental data within 15% (Thornock, et al., 1993). The 2-η model was more than 30% more accurate in predicting NO concentrations occurring in several combustion systems than the 1-η model.

2.4.3 Summary

All of the submodels previously described represent some of the most recent research in coal combustion and gasification modeling. Each submodel had previously been validated by comparison with experimental data, but, because of some changes in the models necessary for incorporation into STAR-CD, individual submodels needed to be reevaluated by comparison between model predictions and experimental data. Each submodel was validated by comparison of overall CFD predictions with the appropriate experimental data. An extensive data set was used in the validation of the submodels (Tree, et al., 1998). These data included concentrations of major gas species (O_2, CO_2, and H_2O), nitrogen pollutant concentrations, char burnout, gas and particle temperatures, particle sizes, and velocity measurements for an experimental facility. These data also included inlet, wall, and outlet boundary conditions.

2.5 Premixed Turbulent Combustion Data Compilation

Some recent research has focused on decreasing pollutants, especially NO_X, in gas turbines (Hedman, et al., 2005). One method that has proven successful in decreasing NO_X is lowering the equivalence ratio (defined as the stoichiometric air-fuel ratio divided by the actual air-fuel ratio) in a premixed system, which lowers the temperature but approaches the fuel-lean flammability limit.

Velocity, temperature, and species concentration data were collected under lean, premixed conditions in the Laboratory-Scale Gas Turbine Combustor (LSGTC) located at Brigham Young University (Hedman, et al., 2005). A schematic of the LSGTC is shown in Figure 2-4. The combustor, originally developed by Sturgess, et al. (1992), consists of a premixed injector that mixes the fuel and air prior to its entering the combustor. This injector also swirls the flow using a swirl generator. Two swirl vanes were constructed to be used in this facility, one imparting medium swirl to the flow (MS), and the other imparting high swirl to the flow (HS). The combustion chamber consists of a box-section combustor with corner fillets. These fillets provide a combustion cross section that can be approximated as axi-symmetric. A quartz window allows optical access to the chamber enabling various laser diagnostic measurements. The product gas exits the combustor through a 92-mm diameter outlet.

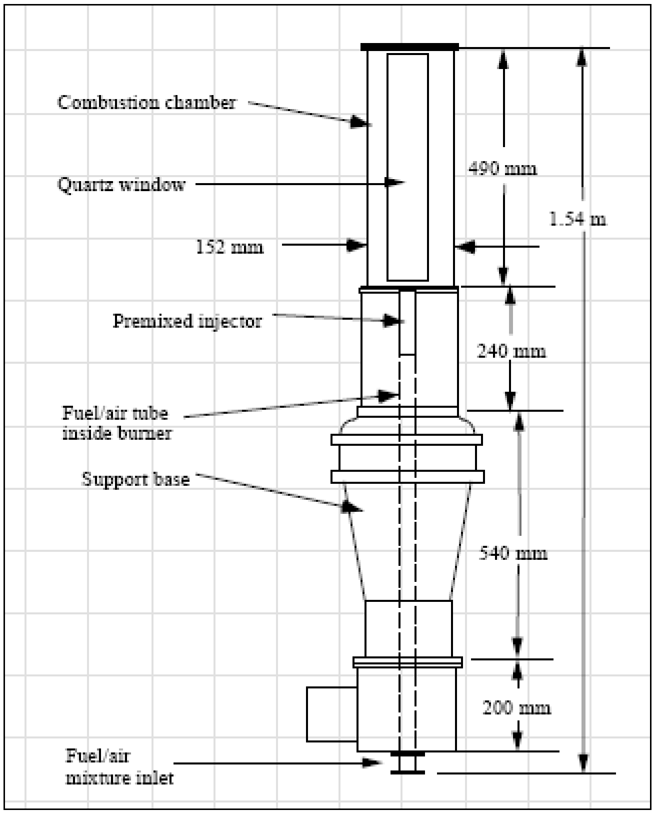

Figure 2-4. Schematic of the Laboratory-Scale Gas Turbine Combustor.

These data were obtained for a swirl-stabilized natural gas flame under four different operating conditions: high swirl (HS) and medium swirl (MS) at fuel equivalence ratios of 0.80 and 0.65. High swirl in this data set corresponded to a swirl number of 1.29, with medium swirl corresponding to a swirl number of 0.72. Table 2-3 contains a summary of the operating conditions for the combustor. The reactants enter the combustor well-mixed at ambient temperature and pressure.

Table 2-3. Operating conditions for the LSGTC.

	HS-0.65	**HS-0.80**	**MS-0.65**	**MS-0.80**
Air flow rate (slpm)	500	500	500	500
Natural gas flow rate (slpm)	35.6	43.8	35.6	43.8
Equivalence ratio	0.65	0.80	0.65	0.80
Swirl number	1.29	1.29	0.74	0.74

*Note: Standard conditions are referenced to 1 atm (101 kPa) and 70°F (21.1°C)

The data include velocity measurements made using laser Doppler anemometry (LDA) (Murray, 1998), temperature measurements made using coherent Anti-Stokes Raman spectroscopy (CARS) (Flores, 2003), and OH concentration measurements made using planar laser-induced fluorescence (PLIF) (Hedman, et al., 2002c). The principles and techniques of LDA, CARS, and PLIF are described in detail by Kohse-Höinghaus and Jeffries (2002), Chigier (1991), and Eckbreth (1996). These techniques provided near-instantaneous measurements at various locations in the LSGTC.

The velocity data were originally reported in the thesis of Murray (1998). Laser Doppler Anemometry (LDA) was used to measure localized velocities. A color separator and mirrors were used to select the two strongest wavelengths from a multi-frequency laser beam, 488 nm (blue) and 514.5 nm (green). The green beam was split into two beams in the horizontal plane, and the blue beam was split into two beams in the vertical plane. One green beam and one blue beam were passed through separate Bragg cells which allowed negative velocities to be obtained. The airflow in the combustor was seeded with 6-μm diameter hollow aluminum oxide spheres. The aerodynamic diameter of these particles was such that they followed the gas flow patterns, even in the recirculation zones. A particle traversing the probe volume produced two Doppler signals. The fringes of the blue beams gave Doppler signals for the axial velocity component and the fringes of the green beams gave the Doppler signals that corresponded to either the radial or tangential velocity component, depending on the orientation of the laser beams.

The temperature data for the LSGTC were originally reported by Flores (2003). The temperature data were obtained using a frequency doubled ND:Yag laser (532 nm) that supplied two pump beams. A portion of the laser energy was split off and used to excite the Stokes laser. A broadband, dual pyromethene dye laser was used to simultaneously excite the Raman frequencies of N_2, CO, O_2, and CO_2. Gas temperatures were determined from the N_2 CARS spectra. Accuracy of the CARS temperature measurements at higher temperatures was ±50 K.

The PLIF OH concentration data for the LSGTC were originally located in the research files of Flores (2003) and Hedman (2006). PLIF is based on tuning a dye laser to a wavelength that corresponds to an absorption peak of a particular species. When a molecule of that species passes through the laser beam, it absorbs the laser energy causing it to elevate to an electronically excited state. From this state, the molecule fluoresces and the fluorescent emission is recorded with an intensified charge coupled display (ICCD) electronic camera. The strength of the emission gives the species concentration at that particular location. PLIF images of OH provide detailed information regarding the instantaneous location of the flame front. This structural information is very useful in analyzing burner designs, understanding combustion phenomena, and validating combustion models.

Data analysis provided mean values, standard deviations, and probability density functions at locations throughout the LSGTC. The velocity, temperature and OH concentration data allow for observations about the flame structure and stability, as well as the effects of swirl and equivalence ratio. The velocity data showed the existence of two recirculation zones, a central recirculation zone and a side recirculation zone, which stabilized the flame. The temperature data showed the effectiveness of the recirculation zones, and helped identify the flame structure, including any instability and extinction. The OH concentration data provided insight into the flame front and its turbulent nature.

The LSGTC was originally modeled using the PDF transport model and a look-up table developed *in situ* (Cannon, et al. 1999). Chemical reactions were modeled using a 5-step chemical mechanism that included CO and NO chemistry. This model accurately predicted (within 15%) velocity, temperature, and species concentration profiles throughout most of the combustor. Discrepancies between predictions and measurements existed for CO species profiles, although correct trends and reasonable agreement were achieved (within 40%). This is in contrast to predictions made without the PDF model, which reported discrepancies as high as several orders of magnitude for CO. The modeling work of Cannon was performed previous to the final experimental work of Hedman and coworkers, so results were preliminary. In addition, species concentration measurements (O_2, N_2, CO, CO_2) were made using CARS, but these data (species concentrations) were later proven to be unreliable.

Originally, a goal of this PhD work was to model the complete data set of Hedman, et al. (2005). This proved to be beyond a reasonable scope for this project. The data of Hedman represent some of the most advanced data available on premixed, turbulent, natural gas combustion. However, the data were taken over a period of 10 years by several different students, and were located in various reports, papers, theses, and dissertations. A real need existed to compile the various data into a central location for future use by the CFD community in validation and verification of CFD codes.

2.6 Literature Summary

Previous research on solar conversion of CO_2 to CO was based on experimental work along with theoretical physics and chemistry, as well as some simple modeling. Detailed CFD modeling was needed to understand the performance of the prototype CO_2 converter. Such modeling could be used to identify potential ways to improve the performance of the CO_2 converter and attempt to quantify the impact of those changes. Modeling work should be an essential part in the development of this solar conversion process.

The research on coal combustion and gasification modeling focused on some of the most current techniques for modeling coal combustion and gasification processes. Previous research culminated in the development of PCGC-3. Data were identified to help verify and validate coal combustion modeling. This work focused on incorporating the advanced coal combustion submodels from PCGC-3 into STAR-CD, a commercial code.

Extensive experimental data, obtained previously in a BYU laboratory facility using advanced laser diagnostics, included velocity measurements, temperature measurements, and OH species concentration measurements. These data provide an excellent benchmark for gas turbine modeling. A need was identified to compile these data into a central location for easy access.

3. Research Objectives and Approach

This project had three tasks, all related to CFD modeling, and covering the three areas of CFD modeling identified in the introduction: code development and improvement, model application, and model evaluation. This section outlines the objectives of this project, and outlines the CFD modeling guidelines that were used in this research.

3.1 Objectives

The objectives of the three tasks were:

(1) Provide insights on how to improve a solar CO_2 converter using CFD modeling.

(2) Improve the capabilities of STAR-CD by incorporating the advanced coal submodels developed in PCGC-3 into STAR-CD.

(3) Provide for better evaluation of lean-premixed turbulent combustion models by assembling available advanced laser diagnostic data into one accessible location.

3.1.1 Solar CO_2 Conversion Modeling

This task involved the modeling and analysis of a high-temperature solar-powered CO_2 converter. The modeling results and analysis could be used to help make this process more economical. This project was divided into the following tasks:

(1) *Accurately model the original prototype CO_2 converter by comparing model predictions with the available experimental data.* Models were developed using PCGC-3, FLUENT, and STAR-CD. For all of these models, accuracy was determined by comparison of model predictions with the limited experimental data available (Traynor and Jensen, 2002).

(2) *Perform parametric studies on the CO_2 converter by varying the peak rod temperature (or radiative flux) and the inlet flow rate.* These predictions were used to better understand all important physical processes, and how they relate to converter performance.

(3) *Explore design alterations or operational adjustments based on CFD modeling that would improve the performance of the converter.* This included varying the rod shapes and locations, flow rates, converter pressures, various CO_2/He mixtures, and converter geometries. This was done to improve the process/equipment in an economical way.

3.1.2 Improved Coal Combustion Modeling Using STAR-CD

The objective of this task was to incorporate advanced coal combustion submodels into STAR-CD. These submodels included: (1) coal set-up and initialization subroutine, (2) simple coal reaction models (devolatilization, char oxidation, and vaporization), (3) the Chemical Percolation Devolatilization (CPD) model, and (4) the Carbon Burnout Kinetic (CBK) model. The main tasks associated with this project were:

(1) *Modify and implement the coal submodels developed for PCGC-3 into STAR-CD.* Modifications included adaptation of stand-alone models, alteration of code structure for interfacing with STAR-CD, or removing variable or solution redundancies from models.

(2) *Verify and validate each submodel by comparison between predictions and experimental data.* Verification occurred after implementation, and involved comparison between individual model predictions and experimental data. Validation of STAR-CD involved comparison between overall CFD predictions and the laboratory furnace data.

3.1.3 Premixed Turbulent Combustion Data Compilation

The objective of this task was to compile the laboratory-scale gas turbine combustor data for model validation. The task associated with this project was:

(1) *Compile all the data from the laboratory-scale gas turbine combustor into a central database for modeling and distribution.*

3.2 Modeling Approach

All modeling research was performed using several of the established guidelines of CFD modeling, including grid dependency studies, linear parametric variable studies, and, where appropriate, submodel evaluation studies. These studies are important to judge the accuracy and reliability of any simulation. They are also important in the analysis and evaluation of the predictions.

A grid dependency study consists of varying the number of grid cells in a model simulation to determine if the predictions from both simulations match. If the predictions vary significantly, a grid-independent solution has not been attained. If the predictions are almost identical, grid independence has been achieved. A grid independent solution is important because it is always the most accurate. Grid dependency studies were performed for both the solar CO_2 converter modeling and the coal combustion validation models for STAR-CD.

In addition to grid studies, submodel evaluation studies were also performed. These studies involve comparison between predictions made using two different submodels that describe the same phenomenon to evaluate their differences. Submodel evaluation studies typically have two distinct divisions. First, a submodel evaluation study will be performed to compare individual submodel predictions. An example of this part of submodel evaluation is the comparison of devolatilization predictions made using the one-step devolatilization model versus the CPD model. Both of these submodel predictions were compared to experimental devolatilization data. The second area of submodel evaluation studies involves overall CFD predictions. Two CFD simulations were performed using separate submodels, and their predictions were compared to each other and to experimental data to evaluate the overall submodel performance. This area also involves comparison of the effect of one submodel on the overall simulation when included versus when excluded. Submodel evaluation studies were performed for both the solar CO_2 conversion modeling project and the STAR-CD implementation project. Submodel evaluation studies included comparisons of FLUENT, STAR-CD and PCGC-3 predictions for the solar CO_2 converter modeling, and comparisons of the effects of different coal models. Submodel evaluation studies are especially important in showing improvements for the coal submodels that will be implemented into STAR-CD versus those already available in STAR-CD.

Parametric studies were also performed on the solar CO_2 converter. These studies involve altering some aspect of the model (for example boundary conditions) to analyze its effect on predictions, as well as to provide increased understanding of the process limitations. Parametric studies included varying the inlet flow rate of CO_2, the incoming radiative flux, and the zirconia rod temperature profile.

3.3 Modeling Methods

Several methods were used to help ensure an accurate solution for any model. These same methods were also used to help guarantee convergence. These methods included using higher-order differencing schemes, lowering of default convergence criteria, and adjusting under-relaxation factors.

Typical flow simulations solve the continuity, momentum, energy, and species continuity equations using the first-order upwind scheme. While the first-order upwind scheme is fairly accurate and converges more quickly than higher-order schemes, it lacks the numerical accuracy of the higher-order schemes like the Quadratic Upstream Interpolation for Convective Kinematics (QUICK) scheme (Leonard and Mohktari, 1990). For this reason, models are typically converged to an intermediate point using the first-order upwind scheme, and then converged further using a higher-order scheme. This method was used to converge cases for both modeling projects, using the QUICK scheme as the higher-order differencing scheme.

Another method that was used to facilitate accuracy is to lower the convergence criteria for the continuity, energy, momentum, or species continuity equations. It is most common to lower the maximum residual tolerance for both the continuity and energy equations. Default values for continuity and energy are generally lowered at least an order of magnitude. While this will increase computational time, it also makes the solution more accurate. Lowering the residual tolerance was used for both projects involving CFD modeling to make sure an accurate solution is achieved.

Adjusting the under-relaxation factors for certain variables is another way to ensure convergence to a solution. Adjusting under-relaxation factors also determines how fast a model simulation converges. Under-relaxation factors are lowered when a simulation is either diverging or oscillating between two values. Cases where under-relaxation factors are lowered include cases where stiffness exists between two or more coupled variables, for example when species concentrations and temperature are coupled through reaction kinetics.

4. Solar CO_2 Conversion Modeling Research

The objective of this task was to model the flow, temperature, and reactions occurring in the prototype solar collector/CO_2. Of particular interest are the heat transfer and reaction mechanisms involved, and the extent of photolysis that occurs in the prototype device. Modeling was performed using three CFD codes: FLUENT, STAR-CD, and PCGC-3. Each CFD code has its own advantages and disadvantages for this project. The main difference between the codes is the method of predicting species concentrations. FLUENT and STAR-CD calculations can use a variety of global reaction-rate equations (kinetic reaction rates, eddy break-up, etc.), whereas PCGC-3 calculations use a mixing-limited approach based on instantaneous local equilibrium calculated using the mixture fraction approach. PCGC-3 calculates species concentrations as a function of the mixture fraction. This approach has been used extensively for modeling turbulent diffusion flames. For this research PCGC-3 was able to predict heat transfer and equilibrium mole fractions of CO_2, CO, O_2, and O present at any point in the converter. PCGC-3 was used to compare equilibrium solutions with the reaction chemistry solution, especially in the heat-up region. PCGC-3 calculations were not useful in the cooling region, because CO quenching is inherently a non-equilibrium process. However the PCGC-3 source code was available, allowing modification to determine the extent of photolysis in the CO_2 converter.

This chapter describes modeling efforts to support the development of the solar CO_2 converter. Modeling of the prototype converter will be described first, followed by parametric studies, followed by converter improvement studies.

4.1 Initial Prototype Modeling

The first step in modeling the solar CO_2 converter was to model the prototype using the experimental operating conditions, and compare model predictions to available experimental data. This also involved determining a reasonable grid density, boundary conditions, and solution schemes and techniques.

4.1.1 Experimental Apparatus

As mentioned previously, Traynor and Jensen (2002) built a 6 m^2 solar collector along with a 6-inch long converter device in an effort to form CO from pure CO_2. The converter device consisted of a conical solar collection section lined with silver, with incoming solar flux focused on a zirconia rod located at the throat of the silver conical section. The zirconia rod was 8.12 cm long with a diameter of 0.724 cm. Downstream of the rod, the product gas was cooled and monitored. This exhaust section rapidly cooled the product gases to quench any reverse reactions of CO. The front end of the converter was sealed with a quartz window, which permitted sunlight to pass through but contained the CO_2 stream. The dimensions of the prototype apparatus are shown in Figure 4-1.

The solar flux to the zirconia rod from the convergent solar mirrors was estimated as the equivalent of 5000 suns of solar flux for the experiments performed. This solar flux heated the zirconia rod to extremely high temperatures. The temperature of the rod was determined experimentally at 5 locations along the rod and is shown in Figure 4-2. These temperatures were either directly measured using a Type K Thermocouple (below 1500 K), or were inferred from the known softening temperature of zirconia. Zirconia begins to soften between 2625 K (4265 ºF) and 2650 K (4311 ºF). Traynor and Jensen determined that the portion of the zirconia rod that extended into the silver funnel (before the throat) reached the softening temperature, based on the observation that, after a run, this portion of the zirconia rod was glazed. Jensen and Traynor used the more conservative softening temperature (2625 K) as the rod temperature for the glazed portion of the rod.

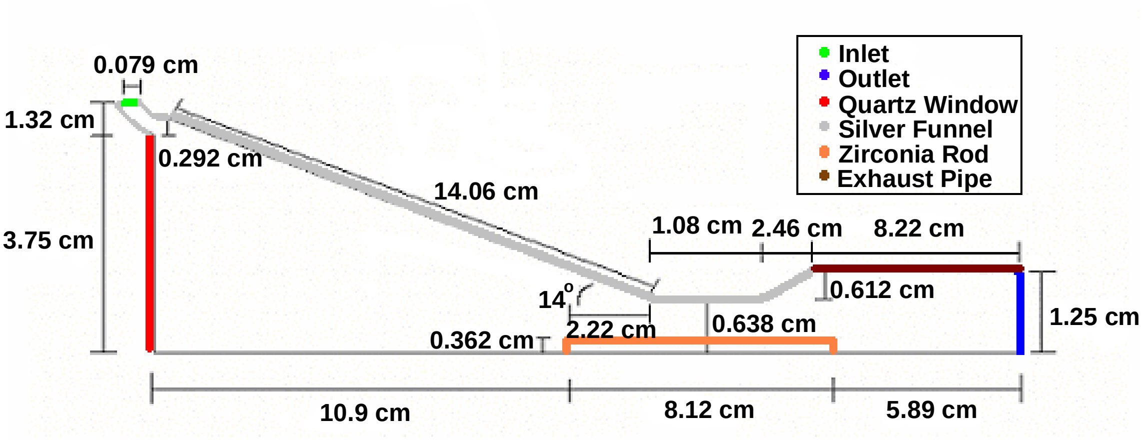

Figure 4-1. CO_2 converter prototype dimensions.

The prototype was operated at ambient pressure, assumed to be an absolute pressure of 1.0 atm. The operating inlet flow rate was assumed to be 10 L/min STP of pure CO_2 initially at 548 K, since some preheating of the CO_2 occurred before it entered the modeled section of the converter. Given the pressure and composition, this volumetric flow rate corresponds to a mass flow rate of 3.272×10^{-4} kg/s, assuming CO_2 behaves as an ideal gas. Exhaust gas exiting the reactor had measured concentrations that varied from 4 to 6 mol% CO.

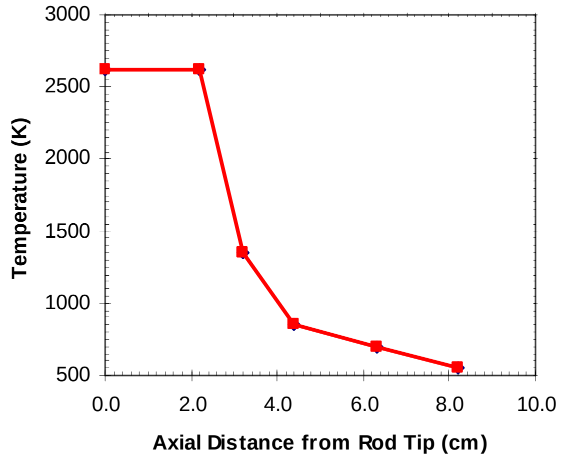

Figure 4-2. Experimentally determined zirconia rod temperature profile.

4.1.2 Theoretical Development

The development of the CO_2 converter model required research in many different areas, including reaction kinetics, equilibrium, specialized reactions, heat transfer, and material properties. Each of these areas is discussed in its own section. Results are discussed in Section 4.1.4.

4.1.2.1 Reaction Kinetics

Three reversible elementary reactions were assumed to take place in the reactor, listed previously in the Literature Review Section as Reactions 2-2 – 2-4. These reactions have rate constants that follow extended Arrhenius expressions. The pre-exponential factors (A), temperature exponents (b), and activation energies (E_a) for these six reactions are listed in Table 4-1. The rate coefficients for both the forward and reverse steps of Reactions 2-3 and 2-4, and the reverse step of Reaction 2-2 were taken from Tsang and Hampton (1986) while the kinetic parameters for the forward reaction of Reaction 2-2 were calculated from equilibrium assuming a simple Arrhenius expression (i.e., b=0).

Table 4-1. Kinetic parameters for the six elementary reactions.

Reaction	Pre-exponential factor (A)	b	Activation energy (E_a/R)
$CO_2 + M \rightarrow CO + O + M$	6.445×10^{10} $m^3mol^{-1}s^{-1}$	0	62600 K
$CO + O + M \rightarrow CO_2 + M$	6.167×10^{2} $m^6mol^{-2}s^{-1}$	0	1510 K
$CO + O_2 \rightarrow CO_2 + O$	1.686×10^{7} $m^3mol^{-1}s^{-1}$	0	26500 K
$CO_2 + O \rightarrow CO + O_2$	2.530×10^{6} $m^3mol^{-1}s^{-1}$	0	24000 K
$O_2 + M \rightarrow O + O + M$	1.807×10^{12} $m^3mol^{-1}s^{-1}$	-1	59380 K
$O + O + M \rightarrow O_2 + M$	1.886×10^{1} $m^6mol^{-2}s^{-1}$	0	-900 K

The reaction ($O + O + M \rightarrow O_2 + M$) has a negative activation energy due to its coefficients being calculated from equilibrium. There is also some disagreement over the coefficients for this reaction; Turns (2000) lists rate coefficients of $E_a = 0$ kJ/mo1, $A = 1.20\times10^5$ $m^6mol^{-2}s^{-1}$, and $b = -1$. The values of the rate constant (k) calculated using both sets of coefficients for this reaction agree to within a factor of 2 in the range of 300 K to 3000 K, as shown in Figure 4-3. Both sets of coefficients were also checked to ensure thermodynamic consistency, by comparing the calculated values of K_{eq} for this reversible reaction with data from the JANAF Thermochemical Tables (1998), as shown in Figure 4-4. As shown, both sets agree quite well with the JANAF data. Because both sets of parameters for the reverse step of Reaction 2-4 have calculated reaction rates that are similar in order of magnitude and agree with thermodynamic data, either could be used. The parameters of Tsang and Hampson were selected to maintain consistency with the other reactions.

Some other reactions were also considered, including the formation of soot, shown in Reaction 4-1.

$$CO \rightarrow C(s) + O \qquad \text{(Reaction 4-1)}$$

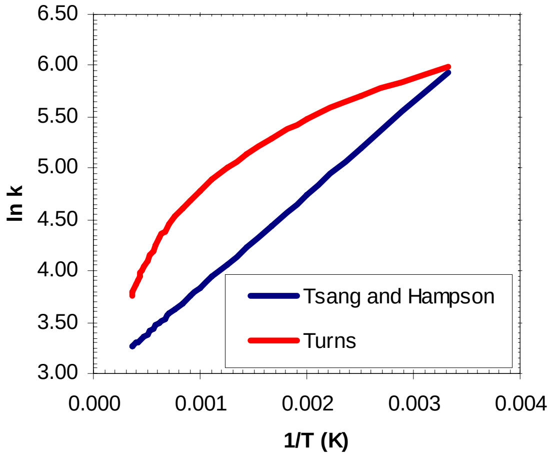

Figure 4-3. Comparison of reaction rates for the reaction O + O + M → O_2 + M.

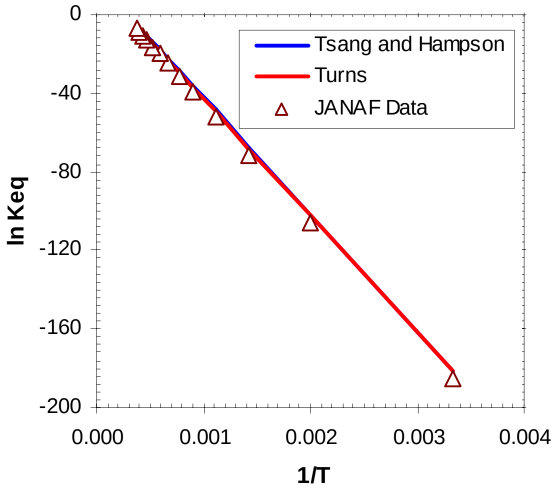

Figure 4-4. Kinetic and thermodynamic consistency check for the reaction O + O + M ↔ O_2 + M.

It was concluded that this reaction does not occur in the converter. This was based on both thermodynamic equilibrium considerations and experimental observations. Equilibrium calculations with the NASA-Lewis code (Gordon and McBride, 1971) and the CET-89 code show that no C(s) is formed at temperatures reaching 2900 K starting with pure CO_2. In addition, during all the experiments performed by Traynor and Jensen no soot was detected on the zirconia rod after a run or in the product gases sampled.

Using CHEMKIN II, the overall kinetic scheme (3 reversible reactions) was proven to be consistent with chemical thermodynamics. Consistency was shown by comparing calculated equilibrium constants and equilibrium compositions over a range of temperatures using the three reversible reaction mechanism, and values for equilibrium obtained from literature (JANAF Thermochemical Tables, 1998). These comparisons showed excellent agreement between calculations and literature values. Other sets of kinetic parameters (GRI, CET-89) showed similar results to the mechanism selected.

4.1.2.2 Thermodynamic Equilibrium

Another modeling approach used to predict the species mole fractions in the solar CO_2 converter is to assume thermodynamic equilibrium at all locations throughout the reactor. This method relates the local temperature to the equilibrium species mole fractions using the mixture fraction model. This approach assumes infinitely fast kinetics that proceed to equilibrium. The mixture fraction approach is widely used in combustion applications, which are mixing limited, and is the main turbulent reaction model used by PCGC-3. Modeling chemistry using the mixture fraction approach was only useful in the heat-up region, and provided a theoretical maximum CO conversion at various temperatures and locations. This mixture fraction approach was not useful in modeling the cool-down region because quenching was inherently a non-equilibrium process.

The thermodynamic equilibrium composition of all species as a function of temperature is shown in Figure 4-5 for an absolute pressure of 1.0 atm. This profile was created using the NASA-Lewis equilibrium code (Gordon and McBride, 1971) for 100% CO_2 at temperatures ranging from 300 K to 3000 K. Below 1500 K CO_2 is the only species present.

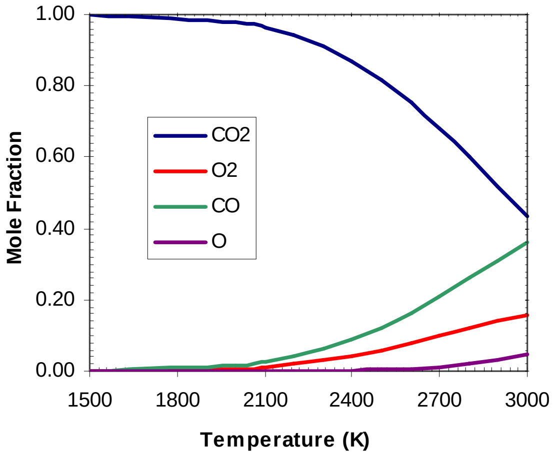

Figure 4-5. Equilibrium mole fractions of all species as functions of temperature.

4.1.2.3 Photolysis Reaction

The photolysis reaction was modeled in PCGC-3 to determine its significance in these experiments. The photolysis reaction is a function of CO_2 concentration, temperature, residence time, photon flux, and optical absorption cross-section (Jensen, et al., 1997). An approximate approach was used to determine the extent of photolysis. Equation 4-1 represents the fraction of CO_2 that is photolyzed in a specified time.

$$\frac{n_0 - n}{n_0} = 1 - \exp(-\sigma \phi t) \tag{4-1}$$

Equation 4-1 used the initial CO_2 molecules (n_o), the optical absorption cross section (σ), the photon flux (ϕ), and the residence time (t) to calculate the CO_2 molecules after photolysis (n). Equation 4-1 is based on an adaptation of Beer's Law for gas depletion, and only applies under conditions where photolysis is possible. The residence time was calculated based on the calculated velocities in each cell for the specified cell dimensions.

The optical absorption cross-section of CO_2 (σ) was calculated as a function of temperature based on the extrapolations of Jensen, et al. (1997).

$$\sigma(T) = 3 \times 10^{-12} \exp\left(\frac{-1.1 \times 10^{5}\, cal/mol}{RT} \right) \tag{4-2}$$

This extrapolation was determined using CO_2 spectroscopic data over the visible spectrum. The temperature in Equation 4-2 was defined as the temperature of the cell of interest, calculated from the CFD simulation.

The photon flux (ϕ) in Equation 4-1 was calculated based on the assumption that the solar radiation intensity in the area of interest was equal to the solar flux of 5000 suns. This was based on dividing the area of the reflecting mirrors by the cross-sectional area of the apparatus at the beginning of the zirconia rod. A typical value for solar radiation on a sunny day is 1000 W/m^2. This value was derived using the solar constant (1373 W/m^2) along with a 30% decrease due to atmospheric scattering and reflection (Siegel and Howell, 1992). This led to a solar intensity of 5,000,000 W/m^2 in the converter at the beginning of the zirconia rod. The peak spectral intensity of sunlight corresponds to a wavelength of roughly 0.53 μm, and this was assumed to be the average wavelength. Using this wavelength, the average photon energy was calculated using Planck's Law ($E=h\nu$). Dividing the solar intensity by the photon energy yielded an average photon flux of 1.33×10^{21} photons/cm^2-s. This method gave a conservative estimate of the extent of photolysis. The actual extent of photolysis may be larger due to the conservative values used in calculating the optical absorption cross-section and the photon flux.

4.1.2.4 Heat Transfer

To accurately model for the solar CO_2 converter, all modes of heat transfer were important: radiation, convection, and conduction. For the initial simulation, radiation was not explicitly modeled. Although radiation dominated the rod temperature profile, it was accounted for by using the experimentally determined zirconia rod temperature profile. This was based on the premise that the radiation flux directed at the zirconia rod caused it to heat up to the experimentally-determined temperature. Carbon dioxide was heated convectively as it flowed past the zirconia rod. Thus, at steady state, the solar radiation entering the converter is transferred to CO_2, with the zirconia rod being the intermediate.

Additional simulations were performed to predict the radiative heat transfer in the cone and on the zirconia rod. These simulations predicted the performance of the prototype using a solar flux boundary condition. The incoming radiation was assumed to have the properties of solar radiation, including an irradiation temperature of 5780 K.

4.1.3 Computational Modeling Details

In order to minimize computer time, the CO_2 converter was modeled using a two-dimensional axisymmetric geometry. All computational grids were constructed according to the dimensions found in Figure 4-1. A grid dependency study was performed using FLUENT 6.0 for this case by comparison of three parameters: zirconia rod heat flux, outlet temperature and CO mole fraction profiles. For this case three grids were constructed, a course grid, a ½ size grid, and a ¼ size grid. Predictions show that the ½ size and ¼ size grids gave similar results (within 2%) for the heat flux off the zirconia rod, as well as the outlet profiles of temperature and CO mole fraction. Predictions from the ¼ size grid were used in the results section. This grid had 18,256 grid cells, with grid cells packed preferentially into the high-temperature region and cool-down section. This grid is found in the Appendix. These same grids were also used to perform grid dependency studies for all other cases. The ¼ size grid was also used in the STAR-CD model. The computational grid for the PCGC-3 calculations was constructed using the same dimensions and boundary conditions with 10,800 grid cells. A grid dependency study was not performed on the PCGC-3 grid due to the time required to construct a grid.

The following solution algorithms and conditions were selected for use based on accuracy and computational efficiency. The prototype was assumed to operate in steady-state mode. The Reynolds number at the throat was calculated to be 91.4 using the properties of pure CO_2 at 2200 K and 1.0 atm with an inlet flow rate of 10 L/min, so the prototype operates in a laminar regime. In FLUENT and STAR-CD, the SIMPLE algorithm was used to model the pressure-velocity coupling (Patankar, 1980). In PCGC-3 the SIMPLER algorithm was selected to model the pressure-velocity coupling because it was the only algorithm available. The momentum, energy, and all species equations were solved in FLUENT using the first-order upwind scheme to begin convergence, followed by using the QUICK scheme to achieve final convergence. In STAR-CD all equations were solved using the 1st-order upwind scheme. PCGC-3 used a hybrid finite-volume method that combines central and upwind differencing schemes. For cases involving radiation heat transfer, radiation transport was solved using the discrete ordinates method with 4 Φ and 4 Θ divisions.

All input parameters for these computations were taken from experimental conditions. The zirconia rod temperature profile was taken from the temperature profile mentioned previously. This temperature profile was programmed into all three codes as a user-defined function. In PCGC-3 calculations, it was necessary to specify the convective heat transfer coefficient between the zirconia rod and the gas. Incropera and DeWitt (1996) list the Nusselt number (Nu) of an annulus at various inner to outer diameter ratios in fully developed laminar flow. These values were used to determine an expression for Nu at any distance from the rod tip (L), as shown in Equation 4-3.

$$Nu_D(L) = \begin{array}{ll} 6.95 - 0.4592\,L - 0.0428\,L^2 & 0.00 \le L \le 2.22 \\ 5.72 & 2.22 < L \le 3.30 \\ 5.72 + 0.4592(L-3.3) + 0.0428(L-3.3)^2 & 3.30 < L \le 5.76 \\ 7.06 & 5.76 < L \le 8.12 \end{array} \qquad (4\text{-}3)$$

This equation was incorporated as part of the zirconia rod boundary condition in the PCGC-3 calculations. The conic silver walls were modeled using adiabatic boundary conditions because it was anticipated that the silver funnel walls were in a region where the gas temperature did not significantly change (upstream of the rod) and the gas was at the same temperature as the silver funnel. The silver walls are involved in directing radiation towards the zirconia rod. The walls in the throat region and the exhaust pipe walls were modeled in FLUENT and STAR-CD using a constant temperature of 548 K. In PCGC-3, the exterior walls were modeled as adiabatic.

Fluid properties were also defined. Density was defined using the ideal gas law. The heat capacity was defined using a temperature-dependent piece-wise polynomial expression. The viscosity and thermal conductivity were defined using the kinetic theory of gases. Mixture properties were defined using mole-averaged species properties.

Many parameters and conditions were required to model radiative heat transfer. A value for the absorption coefficient of 0.001 m^{-1} was used for the CO_2 because there is little or no absorption for CO_2 below 2100 K (Jensen, et al., 1997). In addition, scattering was assumed to be negligible in the CO_2. The properties of the silver reflector cone were also necessary. Polished silver usually exhibits an overall reflectivity of between 75% and 85%. This was approximated with a gray emissivity of 0.15 and no diffuse reflection. No convection was assumed to take place between the gas and the silver. The properties of zirconia were provided by the manufacturer, Cotronics Corporation (1995). Important properties of zirconia include its thermal conductivity (3.0 W/m-K), its emissivity (0.95) and its absorption coefficient (0.95). The emissivity and absorption coefficient were estimated as nearly that of a black body because of the experimental observation that the zirconia rod glowed brightly upon reaching high temperatures.

The zirconia rod was modeled in FLUENT using the mixed radiation/convection option. Any radiation originating from the zirconia rod was presumed to be diffuse. The quartz glass window was modeled as a semi-transparent wall with a given incoming radiation flux and a thickness of 1 mm. The exhaust pipe in the cool-down region was modeled using the radiation/temperature option with a pipe temperature of 548 K. The exhaust pipe emissivity was assumed to be 0.30, based on the material of the pipe.

The photolysis calculations were performed in PCGC-3 in a post-processor mode for each cell after a converged fluid dynamic solution was achieved. The photolysis calculations were limited to those grid cells that were exposed to direct sunlight. These calculations were meant as an order of magnitude estimate due to the conservative values used in developing the photolysis model.

4.1.4 Initial Prototype Results and Discussion

Using the conditions and algorithms discussed in the previous section, each model was solved using the following system:

(1) Flow and heat transfer were predicted for a non-reacting flow case. These cases involved either the experimentally-determined rod temperature profile, or a specified incoming radiation flux.

(2) Species mole fractions were then predicted starting with the non-reacting flow results using (1) various reaction mechanisms in FLUENT and STAR-CD, or (2) the mixture fraction equilibrium approach in PGCG-3.

4.1.4.1 Non-Reacting Flow Case

Non-reacting cases were modeled using all three CFD programs to obtain a first approximation of the temperature and velocity profiles. Each model converged after roughly 3000 iterations. The codes predicted similar velocity and temperature profiles for the non-reacting case, varying by less than 5%. All three models predicted similar velocity profiles, with each predicting a maximum velocity of 8.05 m/s that occurs in the throat of the apparatus. The FLUENT velocity profile is found in the Appendix.

Figure 4-6 shows the predicted temperature profile obtained for the FLUENT model. The FLUENT model predicted local temperatures up to 2623 K with an average outlet temperature of 1140 K. The STAR-CD model predicted similar results to the FLUENT model. The PCGC-3 model also predicted local temperatures up to 2623 K with an average outlet temperature of 1200 K. The difference in the average outlet temperature was due to the differences in heat transfer in the cool-down region. All predictions show a small thermal boundary layer in the near vicinity of the zirconia rod, which grew with increasing axial distance into the converter. FLUENT and STAR-CD predicted a slightly larger thermal boundary layer in the throat and the expansion following the throat than PCGC-3. One possible reason for this difference was the design of PCGC-3, which was developed for turbulent flow, and under turbulent conditions, laminar thermal conduction is typically neglected.

From the non-reacting flow modeling it was concluded that the gas was not heated to any significant extent before reaching the zirconia rod. In addition, the flow patterns were fairly uniform in the region upstream of the rod. This enabled the computational grid to be tightened around the rod and the exhaust section in order to more closely study the key regions of the apparatus, while reducing the required number of grid cells upstream of the rod. The grid was redistributed so that the number of cells was basically unchanged, but the cells were packed more preferentially around the zirconia rod for additional resolution. This redistributed grid was used for all other simulations, with the exception of the radiative heat transfer models.

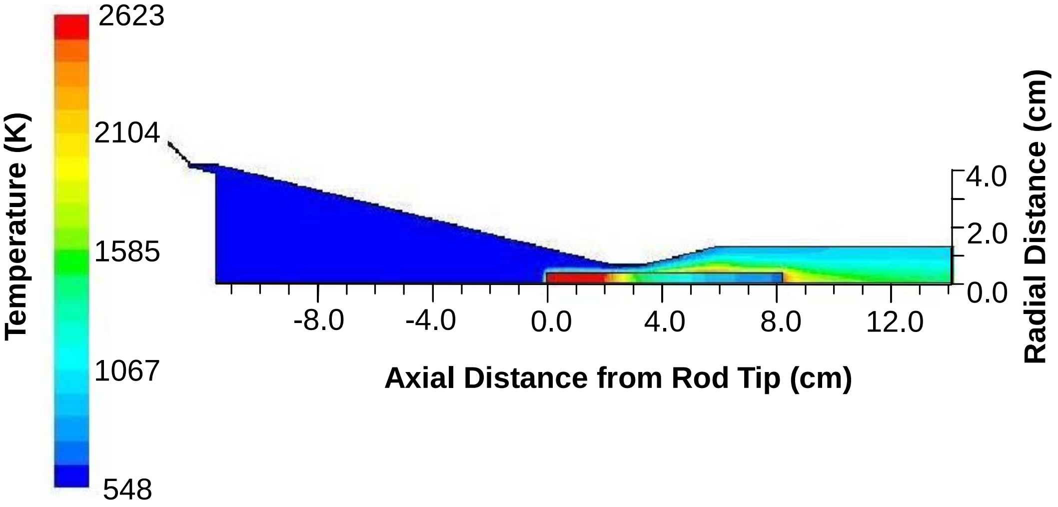

Figure 4-6. Predicted temperature profile for the non-reacting case from FLUENT.

4.1.4.2 Reacting Flow Modeling

The reaction-rate parameters previously listed were added to the FLUENT simulation by enabling the species transport model, selecting the "carbon monoxide/air" mixture option, choosing the volumetric reactions option, and entering all the reaction-rate parameters. It was necessary to eliminate H_2O and N_2 from the possible species because these species were not present in the converter. The O radical species was included in the mixture, with its properties taken from the JANAF Thermochemical Tables (1998). CO_2 was designated as the last species in the mixture because it was the most abundant, and its species continuity equation was not solved directly. Due to convergence difficulties, all species under-relaxation factors, and the energy under-relaxation factor were reduced to 0.10. In STAR-CD, reaction chemistry was activated, and the chemical kinetics option was selected. Under-relaxation factors for species and energy were lowered to 0.20. The same reactions with their reaction-rate parameters were inputted. In PCGC-3, the chemical equilibrium option was activated. It was also necessary to reduce the under-relaxation factors in PCGC-3 to between 0.3 and 0.5.

The FLUENT case required approximately 140,000 iterations to converge, while the PCGC-3 case converged after roughly 60,000 iterations. The STAR-CD case required 125,000 iterations to fully converge. The peak velocity predicted by all models for the reacting flow case was 8.1 m/s compared to 8.05 m/s for the non-reacting case. The maximum radially-averaged velocity in the throat was 5.8 m/s for all three cases.

The temperature profiles for the three cases are shown in Figure 4-7, Figure 4-8, and Figure 4-9. The temperature profiles for all three cases were similar in some regions. All models showed local temperatures reaching 2623 K. The predicted temperature

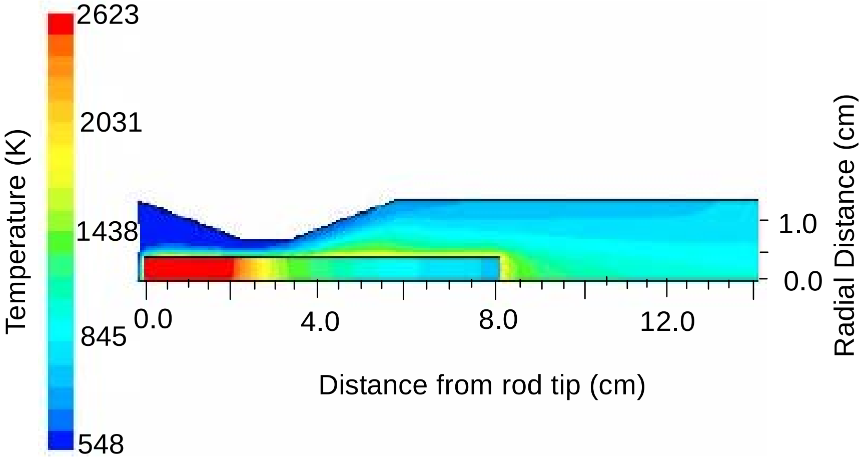

Figure 4-7. Predicted temperature profile using FLUENT.

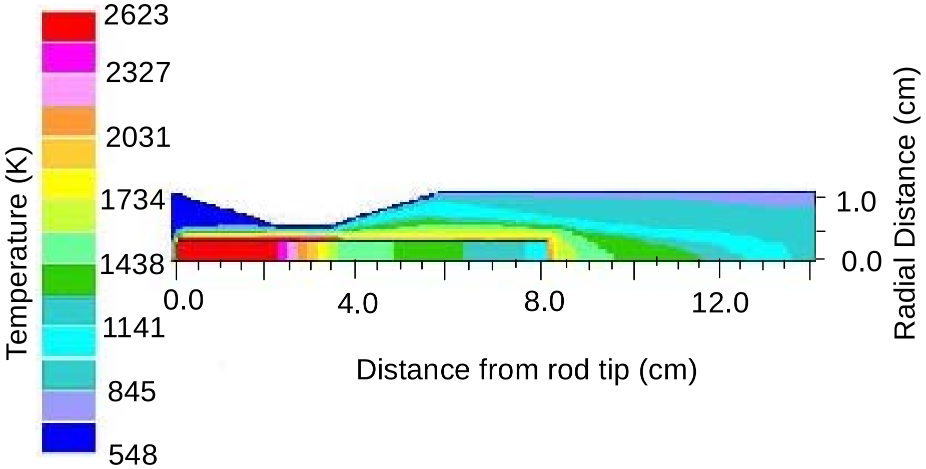

Figure 4-8. Predicted temperature profile using STAR-CD.

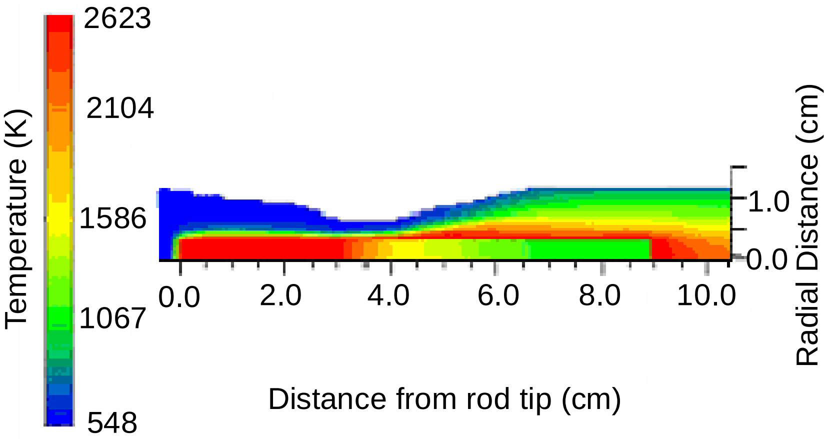

Figure 4-9. Predicted temperature profile using PCGC-3.

profiles showed a steep temperature gradient in the throat, with gas temperatures varying in the radial direction from 2623 K to 548 K. This temperature gradient may be partially responsible for the cooling of the gas downstream of the zirconia rod, as was noted by Traynor and Jensen (2002). In addition, all models show a "thermal boundary layer," a thin region of high-temperature gas located directly around the zirconia rod. The thermal boundary layer and the temperature gradient in the throat indicated that the majority of the CO_2 in the converter bypassed the highest temperatures. The models varied in the temperature directly behind the zirconia rod, with the PCGC-3 model predicting temperatures above 2400 K behind the rod, versus 1900 K for the other two models.

For purposes of interpretation of results, the predictions from each model were averaged in the radial direction. Figure 4-10 shows the area-weighted radially-averaged gas temperature versus axial distance from the rod tip for all three models. The FLUENT model showed a maximum average gas temperature of 1480 K and an average outlet temperature of 1130 K. The STAR-CD model showed similar results to the FLUENT model, with a maximum average gas temperature of 1460 K and an average outlet temperature of 1120 K. This was in contrast to the PCGC-3 model which showed a maximum average gas temperature of 1270 K. All three profiles were similar in the axial location of the onset and end of heating.

The temperature differences between the FLUENT and STAR-CD models and the PCGC-3 model may be due to the differences in convective heat transfer. In PCGC-3, the convective heat transfer coefficient and the rod temperature were specified, but in FLUENT and STAR-CD only the rod temperature was specified. Another reason for the difference was the turbulence assumed by PCGC-3. In turbulent flow, heat conduction in fluids is typically neglected because the molecular thermal conductivity is almost always overwhelmed by the turbulent thermal diffusivity. This led PCGC-3 to predict a steeper radial temperature gradient in the throat. This was especially noticeable when comparing the radial temperature profile in the throat predicted by the three models. In addition, there may be an effect of the endothermic heat of reaction on the predicted temperature, since PCGC-3 predicted a different extent of reaction than the FLUENT and STAR-CD models. The average temperature cooled down in both the FLUENT and STAR-CD models but not in the PCGC-3 model because the first two models used a constant wall temperature of 548 K (flux through the pipe) while adiabatic pipe walls (no flux) were assumed in PCGC-3. The exhaust pipe walls were modeled as adiabatic in PCGC-3 because the results from the quenching region were not used in analysis, and adiabatic boundary conditions typically converge more quickly. The cool-down section predictions from PCGC-3 were not used because the mixture fraction model is an equilibrium model, and the cool-down section was inherently a non-equilibrium process.

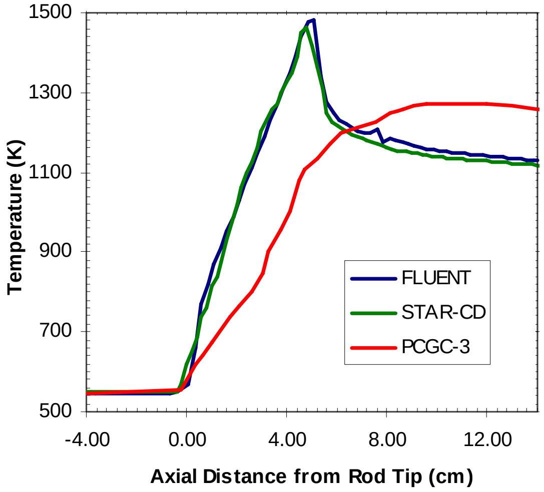

Figure 4-10. Predicted average temperature profiles for FLUENT, STAR-CD, and PCGC-3.

The modeled CO mole fraction profiles for the FLUENT, STAR-CD, and PCGC-3 models are shown in Figure 4-11, Figure 4-12, and Figure 4-13 (Note: different scales are used on each figure), with the radially-averaged CO mole fraction versus distance for all three models shown in Figure 4-14. Radially-averaged CO profiles, CO flow rates, CO conversions, and overall quenching efficiencies were calculated using mass-weighted radially-averaged values. These predictions varied quite significantly in the average amount of CO and the maximum concentrations of CO. FLUENT predicted a peak local CO concentration of 21.4 mol%, with a maximum radially-averaged CO concentration of 8.53 mol%. The FLUENT model predicted an outlet concentration of 4.79 mol% for this case, or 10.47 mg/s of CO in the outlet stream. This outlet amount corresponds to a quenching effectiveness factor (η), defined in Equation 4-4, of 53.9%.

$$\eta = \frac{\dot{m}_{CO\ out}}{\dot{m}_{CO\ peak}} \tag{4-4}$$

The product stream had a CO conversion of 5.03%, defined as the amount of CO exiting the reactor divided by the amount of CO_2 entering the reactor. The product CO represented a chemical conversion of 2.34%, where chemical conversion is defined as the change in enthalpy of the product stream versus the reactant stream at room temperature divided by the total solar energy entering the system, estimated at 4.5 kW.

The STAR-CD model predicted similar results as the FLUENT model, with a peak local CO concentration of 17.4 mol%, a maximum radially-averaged CO fraction of 8.83 mol%, and an average outlet composition of 4.85 mol%, or 10.62 mg/s of CO in the outlet stream. This corresponded to a quenching effectiveness factor of 54.2%.

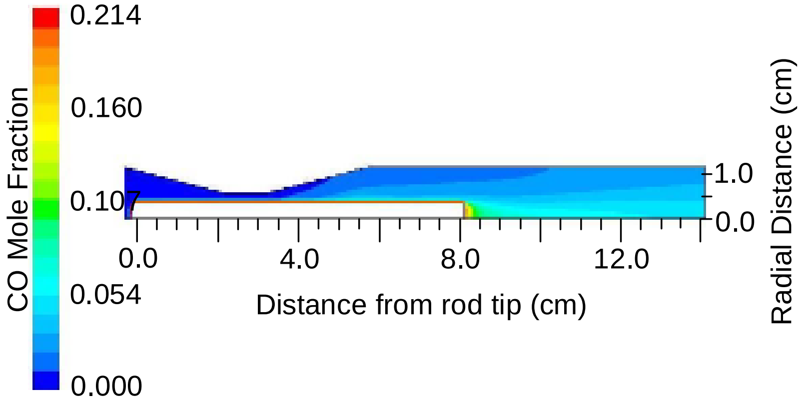

Figure 4-11. Predicted CO mole fraction profile using FLUENT.

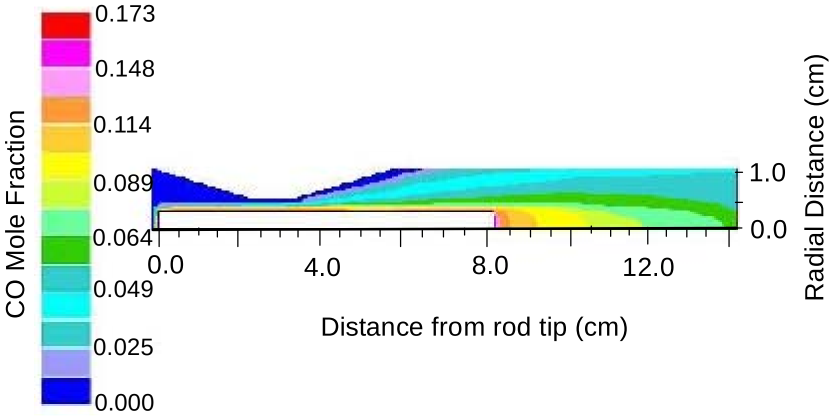

Figure 4-12. Predicted CO mole fraction profile using STAR-CD.

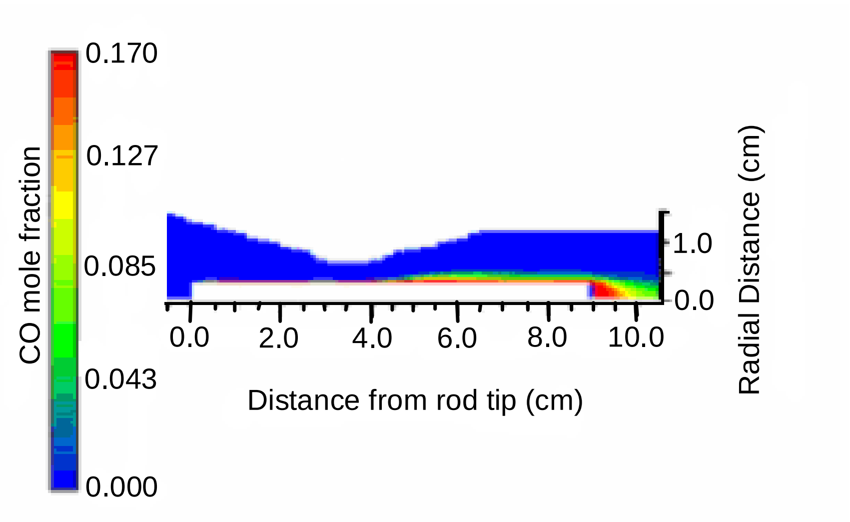

Figure 4-13. Predicted CO mole fraction profile using PCGC-3.

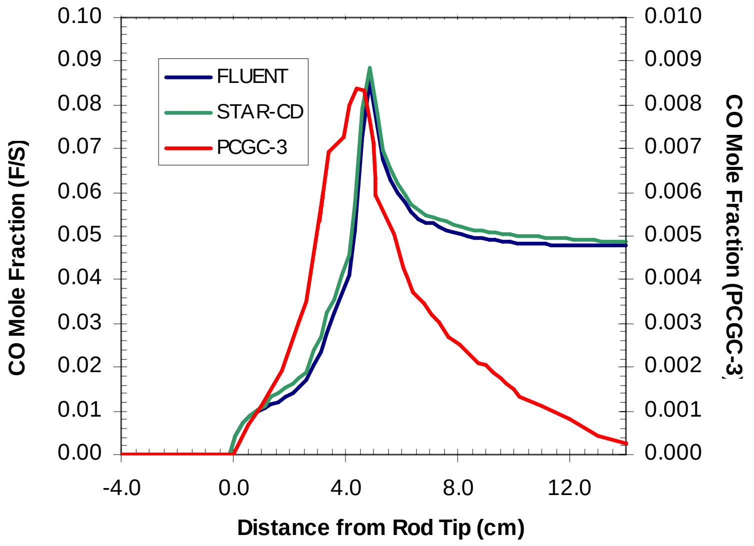

Figure 4-14. Predicted average CO mole fraction profiles for FLUENT, STAR-CD and PCGC-3.

PCGC-3 predicted local CO compositions of up to 17.0 mol% with a minute quantity of CO in the outlet stream. Both FLUENT and STAR-CD models accurately predicted the experimental outlet CO mole fraction, which was measured at between 4.0 and 6.0 mol% CO, while the PCGC-3 model did not accurately describe the downstream quenching. This was anticipated, and the post-rod results from the PCGC-3 models were not used in analyzing the prototype performance.

Both FLUENT and STAR-CD models predicted similar sizes for the radial layer of CO around the rod. Carbon monoxide radially diffusing outward into colder gas may be a factor in the size of these radial layers. Once in a colder environment, all reverse reactions of CO to CO_2 were negligible. Another factor in the size of the radial layers may be an effect of the expansion following the throat, which caused increased radial CO dispersion into colder gas. All three models predicted similar shapes with the CO mole fraction peaking at a distance of 5.0 cm from the rod tip. FLUENT, however, may have slightly over-predicted the CO mole fraction in several control volumes. This was most likely due to the code's inadequate numerical scheme when multiple kinetic reactions were considered. FLUENT 6.0 was designed to handle between 1 and 2 kinetic reactions. FLUENT 6.2 has remedied this short-coming. Because only a few control volumes predicted values above the equilibrium limit, it was not believed that this over-prediction had a significant effect on the outlet CO mol%. STAR-CD did not have the same problem with over-prediction of the CO mole fraction, and gave similar results to FLUENT.

The overall predictions from all three simulations are summarized in Table 4-2. This table shows that the STAR-CD and FLUENT models were accurate in modeling the prototype converter, while the PCGC-3 model failed to accurately predict performance.

Table 4-2. Summary of prototype modeling results.

	FLUENT	**STAR-CD**	**PCGC-3**	**Experimental Results**
Peak temperature (K)	2623	2623	2623	2625-2650
Peak Radially-Averaged Temperature (K)	1480	1460	1270	-
Peak Conversion (%)	9.32	9.66	0.91	-
Outlet Temperature (K)	1130	1120	1270	1123
Outlet CO (mol%)	4.79	4.85	0.02	4-6
$\dot{m}_{COout}$ (mg/s)	10.47	10.62	0.042	-
Outlet Conversion (%)	5.03	5.10	0.02	-
Chemical Conversion (%)	2.34	2.37	0.009	2-3

It was also insightful to examine the predicted O radical profile from the FLUENT model, which is shown in Figure 4-15. This profile showed that the oxygen radical only existed to any appreciable extent in a boundary layer around the rod, which corresponded to the high-temperature thermal boundary layer. This is important because the oxygen radical is important in the formation of CO. At temperatures above 2500 K the reaction rate for the reaction ($CO_2 + O \rightarrow CO + O_2$) is of the same magnitude as the reaction rate for the reaction ($CO_2 + M \rightarrow CO + O + M$) assuming equilibrium CO_2 and O radical concentrations. Both these reaction rates are three orders of magnitude greater than the kinetics for the reaction ($O + O + M \rightarrow O_2 + M$). This meant that, under these high-temperature conditions, the overall reaction of CO_2 to CO was increased by 70% with the O radical compared to a case where no O radical was present. This led to faster equilibrium conversion of CO under these high-temperature conditions.

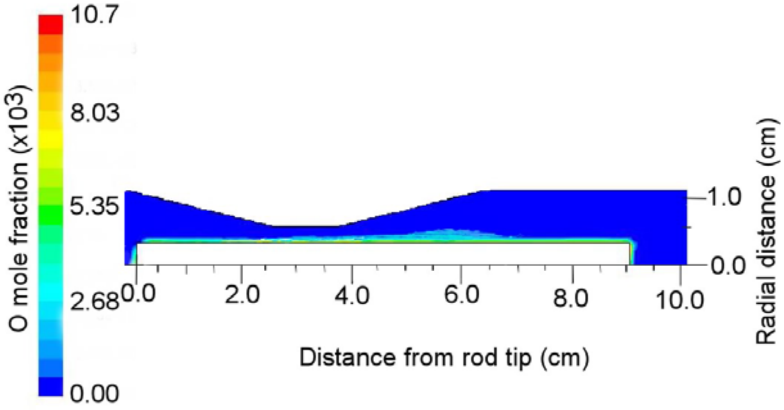

Figure 4-15. Predicted O radical mole fraction profile using FLUENT.

4.1.4.3 Photolysis Reaction Modeling

Because PCGC-3 predictions for temperature were reasonably good before the throat section, the photolysis reaction could be modeled using PCGC-3. The extent of photolysis was modeled with Equations 4-1 and 4-2 using a converged PCGC-3 solution. Using a converged solution was acceptable as a first approximation because photolysis did not affect either the flow or temperature predictions in the converter. Figure 4-16 shows the predicted CO conversion due to the photolysis reaction. These predictions showed that the photolysis reaction did not significantly contribute to the overall CO conversion, accounting for a maximum fraction of 1.74×10^{-3} mol% CO, or 0.037% of the amount from the thermal dissociation of CO_2. This was due to the high gas velocities and corresponding low residence times at conditions where photolysis occurs, i.e., temperatures greater than 2000 K and in the region of intense solar radiation (upstream of the throat). In addition only a thin high-temperature boundary layer was predicted in the region of direct solar radiation. Since the solar radiation traveled only a short distance in this high-temperature boundary layer before being absorbed by the zirconia rod, minimal photolysis occurred. The gas achieved the highest temperatures just downstream of the throat, and hence was not exposed to the direct solar flux.

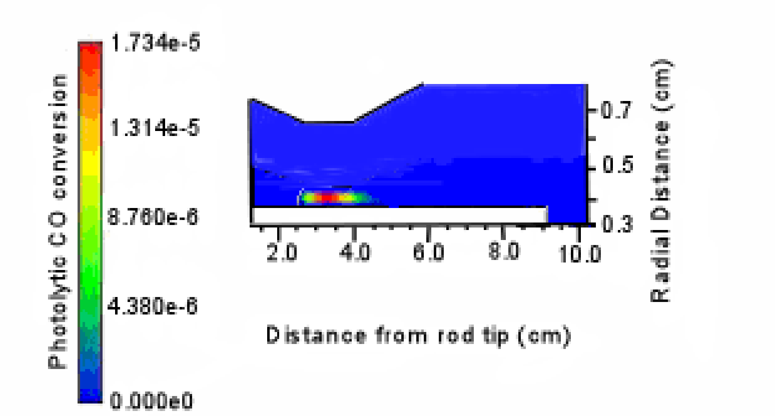

Figure 4-16. Predicted CO mole fraction due to photolysis reaction using PCGC-3.

4.1.4.4 Radiation Heat Transfer Modeling

The success of the original FLUENT and STAR-CD simulations (using the experimentally determined rod temperature profile as a boundary condition) led to efforts to more accurately model all modes of heat transfer: conduction, convection, and radiation. The radiation modeling had three purposes: 1) to provide a more accurate heat transfer model, 2) to validate the experimentally determined zirconia rod temperatures, and 3) to provide an estimate of the experimental solar flux that enters the converter. The solar flux in the model was estimated by varying the solar irradiation incident on the quartz window of the converter and comparing the predicted zirconia rod temperatures with the experimentally determined temperatures. Due to the complexity of the radiation modeling, all cases using radiation were non-reacting cases.

Three cases were modeled using FLUENT with different solar irradiation intensities. Two estimates of the solar irradiation intensities were from Traynor and Jensen (2002), who reported that between 4 and 5 kW of power entered the converter. Therefore, the first radiation case assumed an irradiation of 7.76×10^5 W/m^2, corresponding to 4 kW entering the converter, and the second radiation case assumed an irradiation of 9.70×10^5 W/m^2, corresponding to 5 kW entering the converter. The third case was based on a 100% efficient mirror/converter system. For the last case, a solar irradiation of 1200 W/m^2 (a high-end intensity on a sunny day) was reflected by the solar collector for a total solar power of 7.2 kW, corresponding to an irradiation incident on the glass of 1.40×10^6 W/m^2.

For comparison purposes, the predictions for velocities and temperatures for the non-reacting case described in Section 4.1.4.1 were compared to the predictions from the three radiation cases. The non-reacting case predicted a maximum velocity in the throat of 8.10 m/s. It also predicted local gas temperatures up to 2623 K, with a maximum radially-averaged gas temperature of 1490 K. It also predicted an average outlet gas temperature of 1150 K.

The predictions of the 4.0 kW solar flux case showed a maximum velocity of 7.91 m/s in the throat of the converter. The temperature profile for this case is shown in Figure 4-17. The maximum temperature occurring in the converter was predicted to be 2521 K with a maximum radially-averaged temperature of 1420 K and an average outlet temperature of 1100 K.

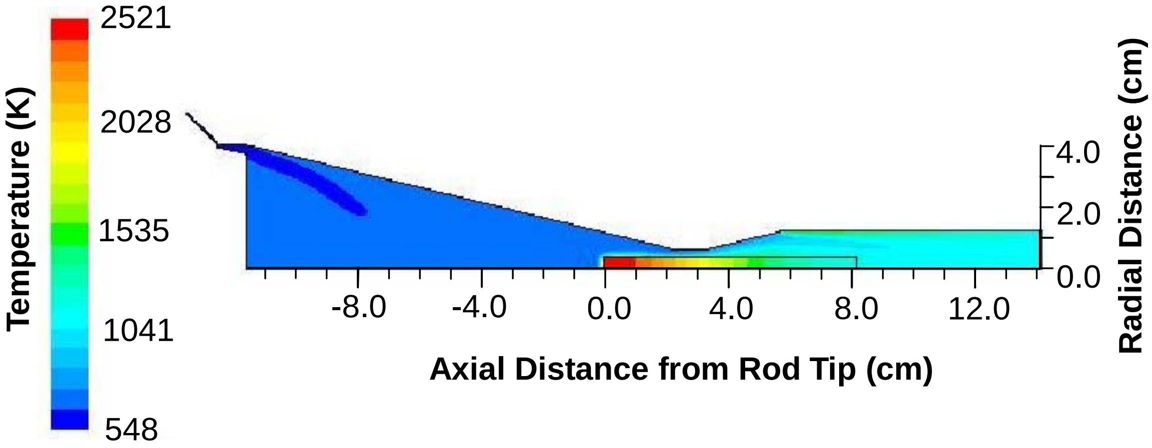

Figure 4-17. Predicted temperature profile for the 4.0 kW radiation case using FLUENT.

The predictions of the 5.0 kW solar flux case resulted in a maximum velocity of 8.43 m/s. The temperature profile for this case was similar to the 4.0 kW case, with predicted local temperatures ranging from 548 K to 2793 K. The maximum radially-averaged temperature was 1530 K, with an average outlet temperature of 1170 K.

The predictions of the 7.2 kW solar flux case showed a maximum velocity in the throat of 9.14 m/s. The maximum predicted temperature for this case was 3258 K, with a peak radially-averaged temperature of 1650 K and an average outlet temperature of 1290

K. The results for all three cases and the non-reacting case are summarized in Table 4-3. The complete modeling predictions for all radiation cases not shown above (all temperature profiles and a sample velocity profile) are found in the Appendix.

Table 4-3. Summary of the radiation cases.

Case	Maximum Velocity	Maximum Temperature	Maximum Average Temperature	Average Outlet Temperature
Assumed Temperature Profile	8.10 m/s	2623 K	1490 K	1150 K
4.0 kW Case	7.91 m/s	2521 K	1420 K	1100 K
5.0 kW Case	8.43 m/s	2793 K	1530 K	1170 K
7.2 kW Case	9.14 m/s	3258 K	1650 K	1290 K

The velocities in all three cases were in good agreement with the non-reacting case if the differences in maximum temperature were taken into account. This was anticipated because the apparatus operated in a laminar-flow regime in which velocity was affected by the physical dimensions of the apparatus and the fluid density in the throat region. Because CO_2 behaved as an ideal gas under the operating conditions, its density was inversely proportional to temperature.

The rod temperature profiles for all three cases, as well as the experimentally determined temperature profile are shown in Figure 4-18. All three cases gave temperature profiles that had similar shapes, varying only in the maximum temperature at the front of the rod. All three cases predicted an axial temperature variation along the rod of roughly 1400 K. As conjectured by Traynor and Jensen, solar power of between 4.0 kW and 5.0 kW entering the converter matched the experimentally determined temperature at the beginning of the rod. The temperature profiles generated from these cases appear to be more realistic than the experimental linear interpolation, especially in the high-temperature (greater than 1500 K) portion of the rod where direct measurements were not made. The high-temperature measurements were estimated based on the observation that this portion reached the softening temperature. It is likely that a flat temperature profile estimation is not as accurate as the modeled profile in this region. A more accurate simulation of the rod temperature could be performed if the temperature dependence of the thermal conductivity of zirconia was known.

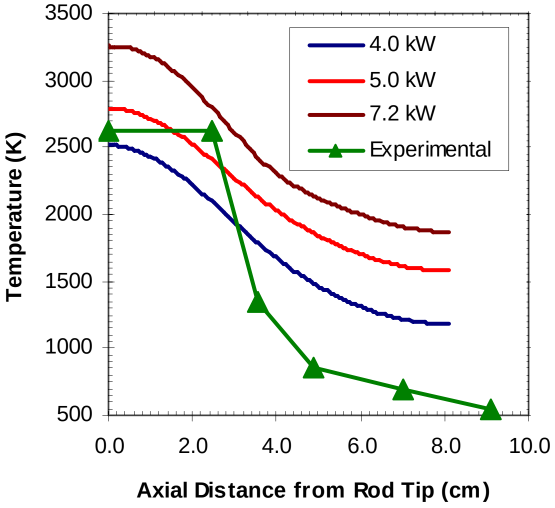

Figure 4-18. Predicted axial rod surface temperature profiles for three radiant fluxes.

The predicted gas temperature profiles for the three radiation cases compared favorably with those of the non-reacting case, judging by the maximum radially-averaged temperatures and the average outlet temperatures. One interesting note was that the three radiation cases predicted high-temperature gas near the exhaust pipe directly after the expansion. This was most likely due to diffuse radiation emission from the zirconia rod heating the exhaust pipe combined with the mixed radiation/convection boundary condition used to model the exhaust pipe. This boundary condition seemed applicable in modeling the prototype, but was unrealistic because it led to predictions of a hot exhaust pipe directly after the expansion. The high-temperature CO_2 (greater than 2100 K) in the near vicinity of the zirconia rod would absorb this diffuse radiation because its absorption coefficient was significant at these temperatures. This would increase the temperature of the CO_2 in the near-rod region. This phenomenon was not modeled for these cases.

4.1.5 Conclusions from Modeling the Prototype Converter

The FLUENT and STAR-CD prototype models accurately predicted outlet compositions of 4.79 mol% and 4.85 mol% for the solar-powered CO_2 converter, which compared favorably with the 4 to 6 mol% CO in the product stream measured by Traynor and Jensen (2002). These models accurately matched the experimentally measured outlet temperature. The use of three reversible reactions accurately described the chemistry. Both the FLUENT and STAR-CD models predicted that all significant reactions occurred in the small thermal boundary layer directly around the zirconia rod. This meant that the majority of the flow bypassed the highest temperatures in the converter.

The PCGC-3 model was fairly accurate in describing the heating of the CO_2 (within 15%) but this equilibrium-based code was not able to predict the quenching in the post-rod section. It also predicted lower radial heat conduction and CO dispersion, which led to a smaller thermal boundary layer and a smaller radial CO thickness. A modified version of PCGC-3 predicted that there was no significant direct photolysis with this converter configuration, which was due to the small thermal boundary layer and the fact that the location of the high-temperature gas did not coincide with the location of the direct solar flux. In this device, the largest high-temperature region was just downstream of the region of high solar flux.

Modeling the solar converter using FLUENT with a solar irradiation boundary condition was accurate in approximating the experimentally determined zirconia rod temperature profile and gas temperature profiles from the non-reacting case. Differences between the radiation model and the original model were due to (1) uncertainties in high-temperature zirconia properties, and (2) failure to accurately model high-temperature CO_2 radiation properties. The radiation model also validated the conjecture of Traynor and Jensen (2002) that the solar power entering the converter was between 4.0 and 5.0 kW.

4.2 Parametric Modeling Studies

To understand the limitations of the converter, parametric modeling studies were performed. Trend analysis was performed using FLUENT to investigate the extent of CO_2 conversion at higher zirconia rod temperatures and various CO_2 flow rates. CO2 conversion was evaluated by the outlet CO conversion for each case. For one study, the assumed maximum rod temperature was increased by 200 K compared to the experimentally determined rod temperature profile. Both the original and the parametric rod temperature profiles are shown in Figure 4-19. This rod temperature profile would be possible to achieve experimentally by increasing the mirror area, but this would necessitate a replacement material for zirconia which softens between 2625 K and 2650 K. For the other parametric study, the inlet flow rate of 10.0 slpm was varied by a factor of 2 while keeping the rod temperature profile the same. In addition, comparative cases were run varying both the flow rate and rod temperature profile. In all, five parametric cases were modeled, with each case summarized in Table 4-4.

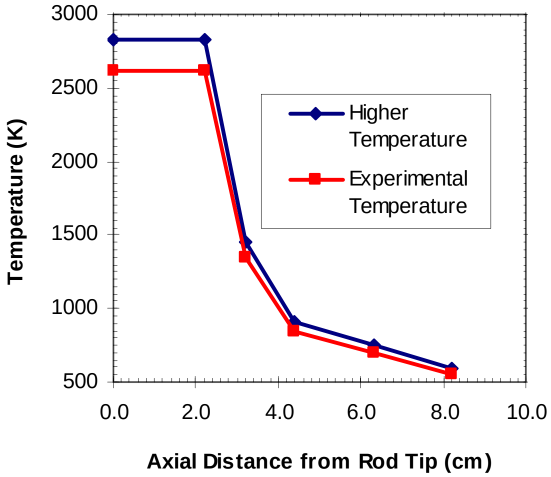

Figure 4-19. Zirconia rod temperature profile for the high-temperature parametric cases.

Table 4-4. Results and conditions for the parametric cases.

	CO_2 flow rate (slpm)	**Peak rod temperature (K)**	**Peak T_avg (K)**	**Peak CO_avg (mol%)**	**Outlet T_avg (K)**	**Outlet CO_avg (mol%)**	$\dot{m}_{COout}$ **(mg/s)**
Base Case	10.0	2623	1480	8.53	1130	4.79	10.5
Case 1 (High Temp)	10.0	**2823**	1530	11.9	1160	5.92	12.9
Case 2 (High Flow)	**20.0**	2623	1280	1.72	1040	1.07	4.63
Case 3 (Low Flow)	**5.0**	2623	1610	10.9	1140	6.15	6.71
Case 4 (High Flow, High Temp)	**20.0**	**2823**	1330	7.18	1080	3.64	16.1
Case 5 (Low Flow, High Temp)	**5.0**	**2823**	1680	14.3	1100	7.01	7.74

4.2.1 Simplified Theoretical Calculations

The parametric modifications will impact the calculated performance of the CO_2 converter by altering the residence time, reaction kinetics, equilibrium, and heat transfer. Some individual effects (residence time, heat transfer, etc.) can be illustrated with simple calculations, showing trends between conditions. These calculations are based on correlations or simplified models. These simplified calculations are discussed here. CFD modeling is necessary to calculate the combined effects of multiple competitive phenomena. The CFD results are discussed in Section 4.2.2.

4.2.1.1 Temperature

Increasing the temperature of the zirconia rod alters conversion by increasing the peak temperature in the reactor. To approximate the effects of changing the peak temperature on the reaction rates, 1-D premixed laminar, reacting flow calculations were performed using CHEMKIN II (Kee, et al., 1992, Kee, et al. 1996). These premixed calculations were based on a mechanism of the three reversible reactions found in Reactions 2-2 – 2-4. These calculations were performed for pure CO_2 at 2623 K and 2823 K to determine the reaction time to equilibrium. These calculations predicted reaction times to equilibrium of 22.8 ms and 10.1 ms for 2623 K and 2823 K. The decrease in time to equilibrium was the result of increased reaction kinetics at higher temperatures.

Increasing the peak temperature alters the equilibrium concentrations of the product mixture. Equilibrium CO compositions at 2623 K and 2823 are 17.3 mol%, and 27.1 mol%; a 56.6% increase in the CO composition.

These theoretical results show that increasing the peak rod temperature can increase conversion by increasing reaction kinetics and equilibrium conversion in the high-temperature region. Because of temperature gradients in the high-temperature region and quenching of the product mixture, CFD modeling was necessary in order to predict the overall impact of increasing the rod temperature on the performance of the converter.

4.2.1.2 CO_2 Flow Rate

Varying the flow rate alters conversion by changing the residence time in the high-temperature region, defined as the part of the apparatus from the beginning of the zirconia rod to the start of the throat. This region corresponds to the hottest portion of the rod. For example, reducing the flow rate would increase conversion in the high-temperature region. While reducing the flow rate may increase conversion of CO from CO_2, it may also decrease the outlet amount of CO due to a lower inlet flow rate. To estimate the residence time in the high-temperature region, an average temperature of 1500 K was assumed throughout this region. This was the maximum radially-averaged gas temperature predicted by the base case FLUENT model. This estimation led to a calculated high-temperature residence time of 5.57 ms for the original operation of the converter (10.0 slpm), with the half-flow parametric case corresponding to a residence time of 11.1 ms, and the double-flow parametric case having a residence time of 2.78 ms.

To approximate the effects of high-temperature residence time, 1-D premixed laminar, reacting flow calculations were also performed using CHEMKIN II (Kee, et al., 1992, Kee, et al. 1996). The premixed calculations were performed for pure CO_2 at 2623 K for the previously calculated residence times. This was done by specifying the length of the reactor and changing the flow rate to correspond to the appropriate residence time. The goal of these calculations was to determine the minimum residence time at which equilibrium could be reached, as well as the theoretical maximum conversion to expect at various residence times. These calculations showed that the original operation of the converter led to a product with 10.1 mol% CO in the high-temperature region, versus 14.8 mol% for the low-flow parametric case. A residence time of 22.3 ms, which corresponded to a flow rate of 2.5 slpm, led to a product with 17.0 mol% CO, very close to the equilibrium value of 17.3 mol% at 2623 K. While these calculations neglected temperature gradients and velocity gradients that would exist in the converter, they showed that the high-temperature region is important for the conversion of CO_2 to CO. These calculations also showed that decreasing the flow rate caused increased conversion in the high-temperature region of the converter.

Decreasing the flow rate also causes an increase in the residence time in the cool-down region. Premixed calculations were also performed to quantify the impact of this region on the CO conversion. Equilibrium product mixtures at 2623 K were cooled to 1200 K over the same reactor volume with a linear cooling temperature profile using different residence times. This approximates different volumetric flow rates of product gases being quenched in the same volume. Calculations were performed for three residence times that correspond to the original prototype operation (10.0 slpm), the low-flow parametric case (5.0 slpm), and the 2.5 slpm case.

These calculations showed that the quenching was less effective for the lower flow rates. This was evident by comparison of the quenching effectiveness factors for the three flow rates. The 10.0 slpm case had a quenching effectiveness factor of 37.6%, versus 26.8% for the 5.0 slpm case and 19.0% for the 2.5 slpm case. Quenching was less effective under these conditions because heat transfer is a function of distance, and not residence time. This meant that for higher flow rates, if the cooling profile was the same, more heat transfer occurred in the fluid, since more fluid was cooled. In addition, this increased heat transfer occurred in a shorter residence time, which caused the cooling to be more non-equilibrium than for a lower flow rate.

These theoretical results showed that lowering the flow rate increased conversion by increasing the residence time in the high-temperature region. These results also showed that quenching effectiveness decreased for lower flow rates. In addition, lower flow rates corresponded to a lower outlet amount of CO. These competing effects can be quantified using CFD modeling, which will predict their combined impact on the performance of the converter.

4.2.2 Parametric Studies using CFD Modeling

To study the effects of temperature and flow rate, five parametric cases were modeled using CFD, as shown in Table 4-4. These cases varied the flow rate and/or the rod temperature. Grid-dependency studies were performed for each parametric CFD case, with each study showing grid independence for the ¼ size grid. Each case was set up using the same algorithms and parameters as the original (base) case, except for the parameter of interest (flow rate/temperature).

4.2.2.1 High Temperature

FLUENT predictions of velocity for the high-temperature case (Case 1) varied only slightly from the initial case, with a maximum velocity of 8.19 m/s occurring in the throat, versus 8.10 m/s for the base case. This occurred because the ratio of the maximum zirconia rod temperatures was only 1.076, accounting for slightly higher velocities in the high-temperature case. The temperature profile predicted by FLUENT for Case 1 was similar to that predicted for the base case, with a steep radial temperature profile around the rod and similar cooling downstream of the rod, effectively quenching reverse reactions of CO. This model predicted a maximum radially-averaged gas temperature of

1530 K, a difference of 50 K versus the original converter model. The model also predicted an outlet temperature of 1160 K. Thus an increase of 200 K in the rod temperature produced an increase of 50 K in the peak average gas temperature. This was due to the fact that the thermal boundary layer of the rod was thin compared to the throat diameter.

This case predicted local CO concentration of up to 30.5 mol%, with a peak radially-averaged CO concentration of 11.9 mol%, and an average outlet CO concentration of 5.92 mol%. This corresponds to an outlet CO flow rate of 12.9 mg/s and a quenching efficiency of 50.2%. Increasing the zirconia rod maximum temperature by 200 K increased the outlet CO by 23%. This model predicted that adequate quenching was still achieved when the rod temperature was increased, but the quenching was less efficient compared to the base case because the product mixture spent a greater cooling time at high temperatures (>2000 K) where reverse reactions were significant. Complete profiles of temperature and CO mole fraction for this case, and the other parametric cases, are found in the Appendix. This parametric case showed that increasing the peak zirconia rod temperature by 200 K increased the outlet CO conversion by 23% due to increased kinetics and higher equilibrium conversion in the high-temperature region.

4.2.2.2 High flow

The high-flow case (Case 2) was modeled using the experimentally-determined rod temperature profile, and predicted a peak velocity in the throat of 14.5 m/s, compared to 8.10 m/s for the base case, which is not quite double. Predicted local gas temperatures in this case were as high as 2623 K, with a peak radially-averaged gas temperature of 1280 K and an outlet temperature of 1040 K.

Maximum local CO composition of 21.4 mol% was predicted for this case, with a peak radially-averaged CO composition of 1.72 mol%, and an average outlet CO composition of 1.07 mol%, or 4.63 mg/s of outlet CO. The outlet amount of CO represented a 56% decrease relative to the base case. This decrease in outlet CO was due to a combination of lower temperatures and decreased residence time in the high-temperature portion of the converter. The lower temperatures were the result of more CO_2 being heated. The quenching efficiency increased because of decreased residence time in the cool-down region due to higher velocities in the converter. Additionally, the majority of the gas was already at a lower temperature, so reverse reactions of CO to CO_2 were further reduced. This parametric case showed that doubling the flow rate decreased the outlet CO conversion by 56% versus the base case due to decreased residence time in the high-temperature region.

4.2.2.3 Low Flow

The low-flow case (Case 3) was also modeled using the experimentally determined zirconia rod temperature profile, resulting in a peak velocity of 4.04 m/s, a maximum local gas temperature of 2623 K, and a maximum local CO composition of 21.4 mol%. A peak radially-averaged gas temperature of 1610 K was predicted for this case, with an average outlet temperature of 1040 K.

The model also predicted a peak radially-averaged CO composition of 10.9 mol%, with an outlet CO concentration of 6.15 mol%, or 6.71 mg/s of CO in the outlet stream. This represents an overall CO conversion of 6.44%, an increase of 28% compared with the base case. The outlet amount of CO was a 36% decrease in the total amount of CO exiting the converter relative to the base case. The low-flow parametric case showed that CO conversion increased by 28% versus the base case, due to increased residence time in the high-temperature region.

4.2.2.4 High Flow-High Temperature

The high-flow high-temperature case (Case 4) was modeled using the high-temperature zirconia rod temperature profile. All predictions for this case are shown in Table 4-4. The predictions for this model showed that increasing both the rod temperature and flow rate increased the amount of exit CO, but reduced the outlet CO conversion. This was due to a combination of higher temperatures and higher flow rates. Higher temperatures in the thermal boundary layer increased equilibrium conversion to CO. Higher flow rates meant more gas was being heated/cooled and decreased residence time in the converter. This case predicted a 24% decrease in CO conversion versus the base case, and a 350% increase versus the high-flow parametric case (Case 2). This was due to increased kinetics (good) offset by decreased high-temperature residence time (bad).

4.2.2.5 Low Flow-High Temperature

The low-flow high-temperature case (Case 5) was modeled using the same temperature zirconia rod temperature profile as the previous case. All predictions for this model are found in Table 4-4. These predictions showed less outlet amount of CO versus the base case. This was due to less total gas passing through the reactor. The predicted outlet amount of CO increased by 15% versus the low-flow case, due to the higher zirconia rod temperatures. The low-flow, high-temperature case predicted 48% and 18% increases in CO conversion versus the base case and the low-flow parametric case (Case 3), due to increasing both the reaction kinetics and high-temperature residence time.

4.2.3 Parametric Studies Conclusions

The important results from the parametric cases are summarized in Figure 4-20. The parametric studies led to several conclusions about converter performance. All parametric cases showed a high-temperature thermal boundary layer of roughly the same thickness (≈ 0.6 mm). This boundary layer thickness represented an area average of only 17% of the throat area. This meant that the majority of the flow never reached high temperature. The second conclusion was that adequate quenching was possible if the rod temperature were increased. CO conversion was found to be a function of both flow rate (residence time) and temperature (reaction kinetics and equilibrium conversion).

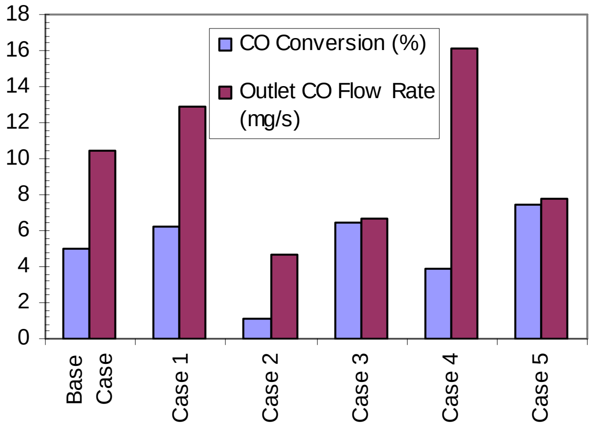

Figure 4-20. Summary of the parametric cases.

4.3 Converter Improvement Studies

For this technology to be viable, the total energy obtained from this process (usable heat + chemical energy) must be much greater than the energy necessary to run the process (pumps, separation equipment, etc.). The economic success of the solar CO_2 converter depends on maximizing conversion to CO with minimal overhead cost.

Maximizing exit CO conversion also enables more cost-effective separation of product CO and O_2 from CO_2. Rough estimates show that this process would be economically sound if 12% CO conversion were achieved.

To increase the conversion, new design methods and operational modes were postulated and evaluated. It seemed reasonable to test the ideas with CFD models before expensive design changes were made and tested experimentally. Improvement was determined based on 1) increased predicted overall conversion to CO, and 2) increased outlet CO flow rate with similar overall conversion. Converter improvements were classified as either (a) design modifications or (b) operational adjustments. Examples of design modifications included altering the shape, diameter, and location of the zirconia rod, and altering the cool-down region. Examples of operational adjustments included altering the inlet flow rate, adjusting the operating pressure, and diluting the CO_2 with helium. Adjustments made included (1) lowering the flow rate to increase CO conversion, (2) decreasing the exhaust/cooling pipe diameter to increase the cooling rate, (3) adding helium to increase heat transfer in the apparatus, (4) increasing the zirconia rod diameter to increase the high-temperature surface area, and (5) increasing the converter operating pressure to increase reaction kinetics. A different lowered flow rate (6 slpm) than analyzed for the parametric modeling studies (5 slpm) was studied because this flow rate corresponded to a proposed experimental flow rate for the converter.

Modeling was also performed on another converter design proposed for scaled-up operation. Each design or operational adjustment was based on some concept or theory that was researched from a theoretical standpoint. In addition, CFD modeling was performed to attempt to quantify the overall effect of these adjustments. The remainder of this section will present simplified theoretical calculations explaining some important phenomena (heat transfer, reaction kinetics, etc.) for each design adjustment, followed by CFD modeling results of each suggested improvement.

4.3.1 Converter Improvement-Simplified Theoretical Calculations

Any adjustment made to the converter, whether an operational change, such as changing the flow rate or operating pressure, or a physical change, such as changing the rod diameter, is expected to impact converter performance through a combination of interactions including fluid flow, heat transfer, reaction kinetics, thermodynamic equilibrium, and reactor residence time. Some of the effects of these adjustments are illustrated with simple calculations, showing trends between conditions. CFD modeling was necessary in order to calculate the combined effects of multiple competitive phenomena. Results from these modeling predictions are discussed in Section 4.3.2.

4.3.1.1 Effects of Pipe Diameter Reduction

Decreasing the cool-down pipe diameter from the original diameter (D_{exit}) in Figure 2-1) to that of the throat diameter causes the convective heat transfer coefficient in the cool-down section to increase by a factor of almost 2. The two heat transfer coefficients (for diameters of 2.5 cm and 1.276 cm) were calculated using the internal laminar flow correlation for a constant wall temperature found in Equation 4-5 (Incropera and DeWitt, 1996).

$$Nu_D = \frac{hD}{k} = 3.66 \qquad (4\text{-}5)$$

The two cases have the same cooling heat transfer because the surface area in the quench region of the base calculation is a factor of 2 larger than for a quench region with the throat diameter, which compensates for the differences in heat transfer coefficients.

The real benefit of reducing the cool-down section diameter is a reduced residence time in the cooling region. 1-D premixed calculations were performed using CHEMKIN II to quantify this effect. These calculations were performed for the same flow rate (10.0 slpm) and the same temperature profile as the original. These calculations showed an outlet CO composition of 11.6 mol% for the narrow exhaust pipe case, versus 6.89 mol% for the original base case. These results show quenching is more effective for the narrow pipe, judging by the increased quenching effectiveness factor; 65.0% versus 37.6% for the original design. The quenching is more effective because heat transfer is a function of surface area rather than residence time. This means that the same amount of heat transfer takes place for flows with higher velocities, but this heat transfer occurs in a shorter residence time. These shorter residence times improve quenching because reaction rates are a function of residence time.

When flows are expanded to increased volume, sometimes adiabatic expansion effects cause changes in the temperature and pressure. Adiabatic expansion effects for the cool-down section of the converter were calculated to cause an insignificant increase in both pressure and temperature (less than 1%) under the operating conditions studied. The expansion would be more beneficial if a large pressure drop occurred, causing rapid cooling behind a shock wave. Modeling results from the original prototype showed that the expansion had a positive impact by increasing radial dispersion of CO into cooler gas where all reverse reactions of CO to CO_2 were negligible. The 2-dimensional effects of radial dispersion were not included in the above theoretical calculations.

These theoretical calculations showed that decreasing the exhaust pipe diameter reduces the residence time in the quenching region, positively impacting converter performance if the same wall temperature profile was used. At the same time, no post-rod expansion of the exhaust stream may result in reduced conversion due to slower radial dispersion of CO into cooler gas. These competing effects can be quantified with CFD modeling.

4.3.1.2 Effects of Rod Shape and Diameter

From the original modeling of this converter, it was concluded that a "thermal boundary layer," defined as a thin region of high-temperature gas (>2000 K) located directly around the zirconia rod, was the location where all significant CO-forming reactions occurred. These modeling results also showed that this thermal boundary layer only changed slightly as the flow was increased or decreased, since the majority of the thermal boundary layer is located in a low-velocity region upstream of the throat. One way to increase the effect of the thermal boundary layer is to increase the high-temperature surface area of the zirconia rod. A larger rod surface area in the high-temperature region corresponds to a greater thermal boundary layer area. This can possibly be achieved by increasing the diameter of the zirconia rod, changing its shape, or adding features to the rod that increase its surface area (such as fins). This could also be accomplished by making the zirconia into a porous material.

Increasing the zirconia rod diameter would increase the high-temperature boundary layer area proportional to the rod diameter increase. Adding features to the zirconia rod would also increase the high-temperature surface area, and may also increase the mixing in the high-temperature region. Increased mixing would increase conversion due to greater heat transfer and increased CO_2 passing through the thermal boundary layer. Unfortunately, it was shown experimentally that any fine features on the zirconia rod crack and break off during the rapid heating experienced during converter startup, due to thermal expansion effects. Therefore, increasing the rod diameter seemed to be the easiest practical way to increase the hot surface area.

Changing the rod diameter impacts multiple variables including velocity and temperature. Since no simple theoretical calculations will accurately quantify the overall effect of this design modification, CFD modeling is needed to predict the effect of this design change on the performance of the converter.

4.3.1.3 Cool-Down Section Modifications

One proposed modification to the cool-down section was to have the hot product gases impact a cold plate, changing the flow direction. This cold plate would be located directly past the high-temperature region, shielded from high solar flux, and cooled with water or cold gas. This proposed modification was also intended to reduce the reverse reactions of CO to CO_2 by immediately contacting the high-temperature product gases with a cold environment. This design change also attempted to increase the heat transfer from the hot gases to the cool wall by causing the flow to become more turbulent through multiple changes of direction. Turbulent heat transfer is usually 2 to 3 times greater than the laminar heat transfer for developed internal flow (Incropera and DeWitt, 1996). In addition to increasing the heat transfer, turbulent flow provides for better mixing. Better mixing and greater cooling would result in more effective quenching of the product gas mixture. A side effect of this modification would be a greater pressure drop through the apparatus as a result of several changes in flow direction (Bird, et al., 2002), although this should not cause any problems. This proposed design change would alter both the flow and the heat transfer. Accessing the comparative impact of this design modification requires CFD modeling.

4.3.1.4 Effects of Increasing the Operating Pressure

A change in the total system pressure is expected to impact the conversion by affecting heat transfer, equilibrium, reaction kinetics, and reactor residence time. Increasing the pressure from 1.0 atm to 2.0 atm, while keeping the volumetric flow rate constant (same average velocity in the converter, double the mass flow rate), increased the convective heat transfer coefficient in the high-temperature region by 41%. These two heat transfer coefficients were calculated using an external flow flat plate correlation, due to a lack of correlations for longitudinal flow over a cylinder (Incropera and DeWitt, 1996). This correlation (shown in Equation 4-6) is appropriate because it most accurately represents the flow of CO_2 over the high-temperature portion of the zirconia rod.

$$Nu_L = \frac{hL}{k} = 0.66\,\mathrm{Re}^{\frac{1}{2}}\,\mathrm{Pr}^{\frac{1}{3}} \tag{4-6}$$

Increasing the pressure to 2.0 atm, while keeping the mass flow rate constant (reducing the volumetric flow rate by 50%), has little effect on the convective heat transfer coefficient in the high-temperature region, since the increase in density is compensated by a decrease in velocity, so that the Reynolds number remains the same.

Increasing the pressure has minimal effect on the heat transfer between the high-temperature gas mixture and the cool pipe walls. This occurs because the laminar convective heat transfer coefficient for developed internal flow with constant wall temperature is only a function of the pipe diameter and gas thermal conductivity, as shown previously in Equation 4-5.

Increasing the pressure changes the thermodynamic equilibrium mole fractions of the $CO_2/CO/O_2/O$ mixture at high temperatures. This effect follows LeChatelier's Principle, which states that as pressure increases gas-phase equilibrium favors the state with fewer total gas-phase moles (Sandler, 1999). In other words, for the overall reaction $CO_2(g) \rightarrow CO(g) + \frac{1}{2} O_2(g)$, a pressure increase would cause an equilibrium shift towards the reactant CO_2. This effect is seen in Figure 4-21, which shows thermodynamic equilibrium mole fractions of CO, starting from pure CO_2, at varying pressures for the range of temperatures seen in the solar CO_2 converter. The equilibrium calculations were performed using the NASA-Lewis equilibrium code (Gordon and McBride, 1971).

Increasing the pressure also impacts the reaction kinetics in the converter. Increasing the pressure increases the concentrations of each species, and hence increases the kinetic rates of each reaction and causes them to approach equilibrium more quickly. This is beneficial in the high-temperature region, but a drawback in the cool-down region.

The last effect of increasing the pressure, for a constant total mass flow rate of gas, is a corresponding increase in the reactor residence time due to increased density. An increase in reactor residence time is expected to increase conversion in the high-temperature region but reduce the quenching effectiveness of the cool-down section.

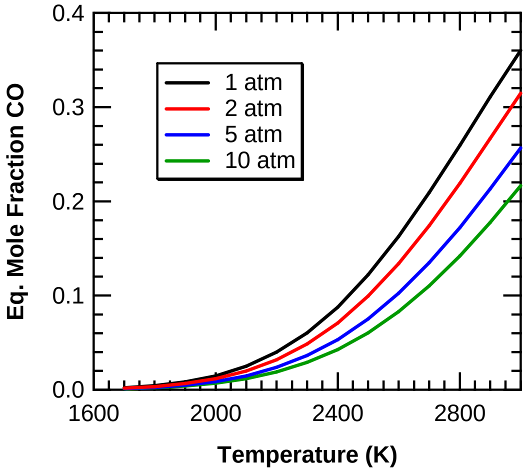

Figure 4-21. Thermodynamic equilibrium CO mole fractions versus temperature for various pressures.

In summary, increasing the pressure will cause changes in heat transfer, equilibrium, reaction kinetics, and reactor residence time, with competitive effects on the CO conversion. CFD modeling was therefore necessary to determine the combined effects of increasing the pressure.

4.3.1.5 Effects of Helium Addition

The thermal conductivity of He is 5.5 times higher than that of CO_2, which could increase the heat transfer from the hot zirconia rod to the surrounding gas in the high-temperature region and also from the hot product gas to the cool pipe walls (Incropera and DeWitt, 1996). Pure helium has a 53% higher convective heat transfer coefficient than pure CO_2 in the heating section of the apparatus, based on the external flat plat correlation (see Equation 4-6), assuming the same volumetric flow rate for both cases. In order to maintain a constant volumetric flow rate for the helium case, the overall mass flow rate must be reduced. Mixtures of 50/50 mol% CO_2/He and 75/25 mol% CO_2/He mixtures have 30% and 13% greater convective heat transfer coefficients in the heating region than pure CO_2. In the cooling region, helium has a 550% greater convective heat transfer coefficient than pure CO_2, based on the internal laminar flow correlation with constant wall temperature discussed previously. Mixtures of 50/50 mol% CO_2/He and 75/25 mol% CO_2/He mixtures have 340% and 220% greater convective heat transfer coefficients in the cooling region, respectively, than pure CO_2 using the same internal flow correlation. There is a clear incentive to use helium to increase heat transfer.

Helium dilution also changes the thermodynamic equilibrium mole fractions of all species. Dilution of CO_2 with 25 mol% He causes the equilibrium CO mole fraction to decrease from 17.3 mol% to 14.3 mol% at peak converter temperatures (2623 K).

The addition of helium also impacts the reaction kinetics, since the helium dilutes the CO_2, causing a decrease in the rate of all reactions involving CO_2. Premixed calculations for the same volumetric flow rate show that reaction rates are only slightly lowered as a result of dilution. Calculations for pure CO_2 and 75/25 mol% CO_2/He show similar reaction times to equilibrium at high temperatures ($\approx$20 ms) for both cases, and similar quenching efficiencies for both cases using the same cooling temperature versus distance profile. The cooling calculations do not account for the higher heat transfer from the mixture due to the addition of helium.

Adding helium will impact the conversion of CO_2 to CO by affecting the heat transfer and overall amount of CO_2 in the reactor. It would also slightly affect reaction kinetics, although the differences between the pure CO_2 and the CO_2/He mixture are more the result of dilution than of differences in reaction kinetics. Therefore, CFD modeling is needed in order to evaluate the overall impact of He addition to the CO_2 in the converter.

4.3.1.6 Simple Theoretical Calculations Conclusions

These simplified theoretical calculations and 1-D model results show that each proposed adjustment has the potential to improve the converter performance. Each adjustment impacts one or more of the following: heat transfer, reaction kinetics, equilibrium, and reactor residence time. Because all these phenomena are coupled, CFD modeling was necessary to calculate their overall effect on converter performance.

4.3.2 Converter Improvement CFD Studies

Each suggested converter improvement required CFD modeling in order to accurately quantify the overall impact on CO conversion in the converter.

4.3.2.1 Improvement Modeling Details

FLUENT calculations were performed using the same grid used in previous modeling studies in cases where operational adjustments were made. For design modifications, the converter geometry was altered, but the grid size and number of grid cells remained roughly the same. In all, four geometries with associated grids were used for predictions: (1) the original geometry; (2) a geometry with no expansion following the throat; (3) a geometry with a larger diameter rod and no expansion following the throat; and (4) a geometry with a conic zirconia surface and an impaction plate directly after the zirconia cone. For the last geometries, grid independence was determined using grids with similar dimensions to the ½ and ¼ size grids from the original geometry. These grids predicted fairly similar results for outlet CO mole fraction and outlet temperature. Simple schematics of these four configurations are shown in Figure 4-22.

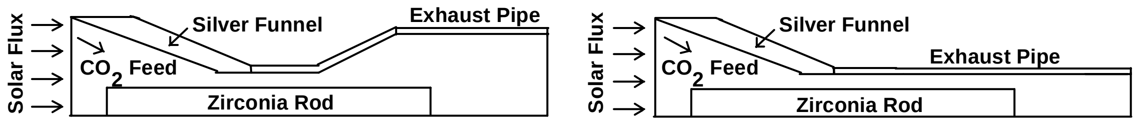

(a) Base geometry (b) No expansion after throat

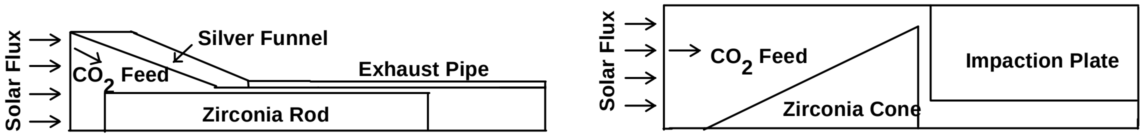

(c) Thicker rod (d) Conical geometry

Figure 4-22. Simple geometric configurations for the improvement cases studied.

Eight simulations were performed to examine the effectiveness of all suggested improvements. The input parameters that vary from case to case are shown in Table 4-5, along with the overall modeling results for each case. All other input parameters and submodels were described previously in Section 4.1.3.

Table 4-5. Inputs and results for CFD cases modeled for improvement studies.

	Base Case (10 slpm)	Case 6 (6 slpm)	Case 7 (Pipe Diam)	Case 8 (Fat Rod)	Case 9 (2 atm)	Case 10 (2 atm, 2x)	Case 11 (25% He)	Case 12 (Conic Rod)
Geometric configuration (Figure 4-22)	a	a	b	C	a	a	a	b
CO_2 flow rate (slpm)	10.0	6.0	6.0	6.0	6.0	12.0	6.0	10.0
Apparatus operating pressure (atm)	1.0	1.0	1.0	1.0	2.0	2.0	1.0	1.0
Inlet composition (% CO_2/He)	100	100	100	100	100	100	75/25	100
T_avg at throat (K)	1480	1590	1590	1650	1530	1490	1640	1610
CO_avg at throat (mol%)	8.53	10.4	10.4	11.9	11.0	9.69	8.22	9.50
Peak CO Conversion (%)	9.32	11.6	11.6	13.5	12.3	10.7	11.9	10.5
Outlet T_avg (K)	1130	1030	970	940	970	930	970	1170
Outlet CO_avg (mol%)	4.79	5.85	6.47	7.20	4.47	5.05	4.66	5.15
Conversion to CO (%)	5.03	6.22	6.91	7.76	4.68	5.32	6.52	5.44
Quenching Efficiency (%)	53.9	53.5	59.5	57.3	38.0	49.6	54.6	51.7
$\dot{m}_{COout}$ (mg/s)	10.47	7.77	8.64	9.70	5.85	13.29	6.11	11.3

For all cases involving the zirconia rod, the rod temperature profile was assumed to have the same temperature profile as the original operating condition (see Figure 4-2). While design modifications and operational adjustments undoubtedly will influence the zirconia rod temperature profile, standard experimental operation of the converter involved heating the portion of the zirconia rod that extends into the silver funnel up to the softening temperature of the zirconia. This was achieved experimentally by varying the number of individual solar mirrors focused on the rod, and thus varying the incoming radiation energy. Therefore, it was assumed for all modeling cases that any portion of zirconia upstream of the throat was at the softening temperature of zirconia (2623 K).

The original zirconia rod temperature profile downstream of the throat was also used for all cases. This downstream temperature profile was based on the detailed radiation modeling efforts discussed previously which predicted similar rapid axial cooling of the zirconia rod downstream of the throat for various incoming radiation fluxes, consistent with the experimentally determined rod temperature profile.

For the cone and impaction plate model, the temperature of the zirconia cone exposed to the solar flux was assumed to be 2623 K using the same arguments presented above. The unexposed side of the zirconia cone was assumed to be adiabatic, and the impaction plate was modeled as a constant temperature boundary of 800 K.

Non-reacting flow calculations were performed to obtain a first approximation of the temperature and velocity profiles for each case by running only the continuity, momentum, and energy equations for 1000-2000 iterations. The chemistry was then activated, and the case was run to convergence. All under-relaxation factors were reduced to 0.1 to avoid convergence problems. Most cases required 80,000-150,000 iterations to converge because of the low under-relaxation factors. The modeling results from the eight representative simulations are discussed in the following sections.

4.3.2.2 Flow Rate

The results presented in the Parametric Studies Section indicated that lowering the CO_2 flow rate to 5.0 slpm increased the conversion of CO_2 to CO. A flow rate of 6.0 slpm was studied for this analysis because experimental results were available for this flow rate. The temperature predictions for the two cases showed peak local gas temperatures of 2623 K, corresponding to the hottest portion of the zirconia rod. Figure 4-23 shows the predicted radially-averaged temperature profiles for both the base case and Case 6 (6 slpm). The temperature profiles were similar in both shape and relative magnitude. The peak average temperature was predicted to be 1480 K for the base case and 1590 K for Case 6. The average outlet temperature predicted for the base case was 1130 K versus 1030 K for Case 6. Overall heat transfer from the rod to the gas and from the gas to the exhaust pipe was predicted to decrease from the base case to Case 6, but this was counteracted by lower velocities and longer residence times. The overall impact of both these phenomena was a higher average peak temperature and a lower average outlet temperature predicted for Case 6 versus the base case.

Peak local CO compositions of up to 21.4 mol% were predicted in both cases. Figure 4-24 shows the predicted radially-averaged CO mole fraction profiles for both cases; a peak average CO concentration of 8.53 mol% was predicted for the base case and 10.4 mol% for Case 6. An outlet CO concentration of 4.79 mol% was predicted for the base case, with 5.85 mol% in Case 6. These predictions show that peak CO conversion was increased in the high-temperature region of Case 6 by 24.4%. Outlet conversion of

CO was also increased by 23.7% to a value of 6.22% for Case 6. The quenching efficiencies were similar for the two cases: 53.8% for the base case versus 53.5% for Case 6. Although the outlet conversion increased for Case 6, the outlet amount of CO produced was 25.8% less (i.e., 7.77 mg/s for Case 6 versus 10.47 mg/s for the base case). These predictions agree with trends in experimental results obtained after this modeling work was performed. The experimentally measured CO concentrations in the product increased to 6.2 ± 0.8 mol% (from 5.0 ± 1.0 mol%) when the flow rate was reduced to 6.0 slpm from 10 slpm (Jensen, 2005).

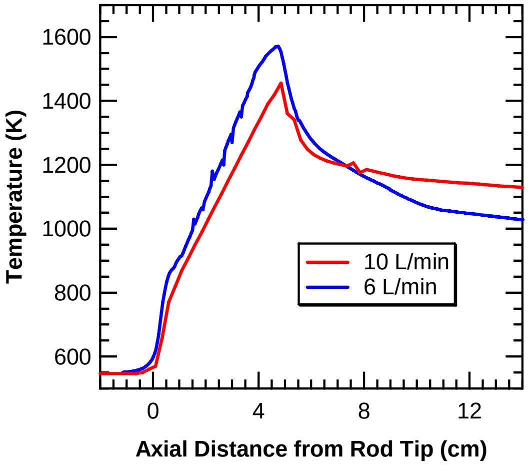

Figure 4-23. **Predicted average temperature profiles for base case (10 splm) and Case 6 (6 slpm).**

These predictions show that decreasing the flow rate to 6.0 slpm caused the converter to be more effective in the high-temperature region while only slightly reducing the effectiveness of the quenching. These effects were directly related to the residence times in both regions. While this reduced flow increased the outlet conversion of CO, it decreased the overall amount of CO produced. All these predictions agreed with experimental results taken after the fact. This case predicted that reducing the flow rate from 10 slpm to 6 slpm increased CO conversion by 24%.

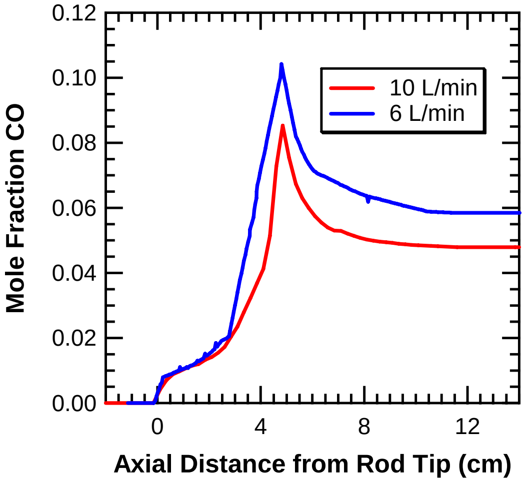

Figure 4-24. Predicted average CO mole fraction profiles for base case (10 slpm) and Case 6 (6 slpm).

4.3.2.3 *Effects of Pipe Diameter Reduction*

A comparison of Case 7 (no expansion following the throat) with Case 6 illustrates the effect of changing the exhaust pipe inside diameter from 2.50 cm to 1.27 cm. The throat diameter was 1.27 cm, so Case 6 had an expansion in the cool-down region while Case 7 had a straight pipe in this region (see Figure 4-22(b)). Both of these cases used an inlet flow rate of 6.0 slpm. Predicted radially-averaged temperature and CO mole fraction profiles for Cases 6 and 7 are shown in Figure 4-25 and Figure 4-26. Both temperature and CO mole fraction predictions showed no significant differences between the two cases upstream of the exhaust pipe diameter change. Both cases have identical peak temperature and CO mole fraction that occur upstream of the exhaust section. The gases cooled more quickly in the reduced exhaust diameter case (Case 7). The predicted average outlet gas temperature decreased from 1050 K for Case 6 to 970 K for Case 7. From the highest temperature region to the outlet, Case 7 dissipated 10.7% more heat than Case 6. This increased cooling also led to a greater predicted outlet CO composition, 6.47 mol% in Case 7 versus 5.85 mol% in Case 6. This corresponds to an 11.2% increase in CO conversion for Case 7 versus Case 6. The quenching efficiency predicted for Case 7 was 59.5%, versus 53.5% for Case 6.

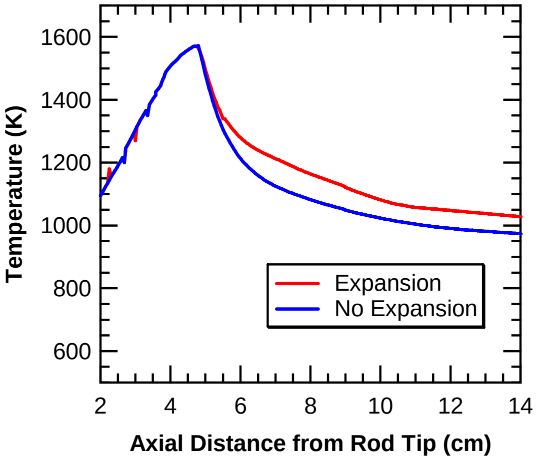

Figure 4-25. Predicted average temperature profiles for Cases 6 and 7.

These modeling predictions showed that narrowing the exhaust pipe diameter slightly increased the heat transfer from the $CO_2/CO/O_2$ product mixture to the exhaust pipe. In addition, the narrowed pipe diameter decreased the residence time in the quenching region. Decreasing the residence time in the cooling region reduced the impact of reverse reactions of CO to CO_2. Both these factors combined to provide better quenching that led to increased CO mole fractions in the product. The increased radial dispersion of CO into colder environments caused by the expansion in the original converter did not appear to significantly affect quenching. CFD simulations predicted that reducing the exhaust pipe diameter while maintaining the flow rate caused a 13% increase in CO conversion.

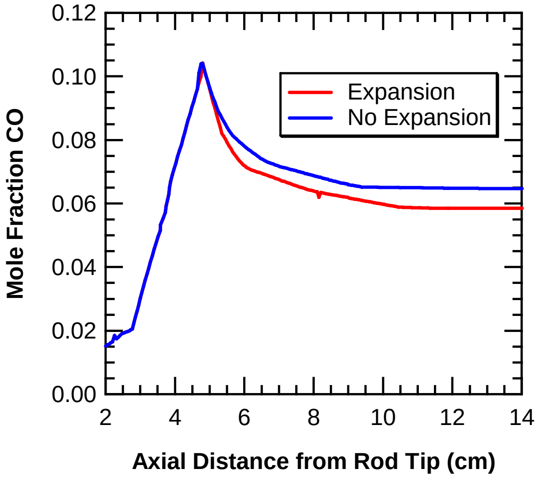

Figure 4-26. Predicted average CO mole fraction profiles for Cases 6 and 7.

4.3.2.4 Larger Zirconia Rod Diameter

The effects of increasing the zirconia rod diameter, and hence narrowing the annulus for the gas passage, are shown by comparing Cases 7 and 8. The increase in rod diameter caused an increase in the thermal boundary layer area. The original zirconia rod had a diameter of 0.724 cm, while the thicker modeled rod had a diameter of 1.143 cm. Both Case 7 and 8 had a narrow exhaust pipe with an inside diameter of 1.27 cm. To achieve accurate radial profiles of temperature and CO mole fraction in the throat, the grid size through this narrow annulus was decreased by a factor of 5 in the radial direction. This model was run with an inlet flow rate of 6.0 slpm, corresponding to the proposed operation of this new converter design.

The predicted temperature profile and the CO mole fraction profile for Case 8 had local maxima of 2623 K and 21.6 mol%. The predicted high-temperature thermal boundary layer for Case 8 was 0.62 mm, which was close to the annular gap of 0.63 mm in the throat section. There was still a steep radial thermal gradient in the throat section. Predicted radially-averaged temperature and CO mole fraction profiles for Case 8 are shown in Figure 4-27. These profiles have similar shapes and relative maxima to those of the base case, as well as to profiles for the other cases previously discussed. Both the average temperature and average CO mole fraction profiles predicted for Case 8 showed higher maxima than any other case (1650 K and 11.9 mol%, respectively).

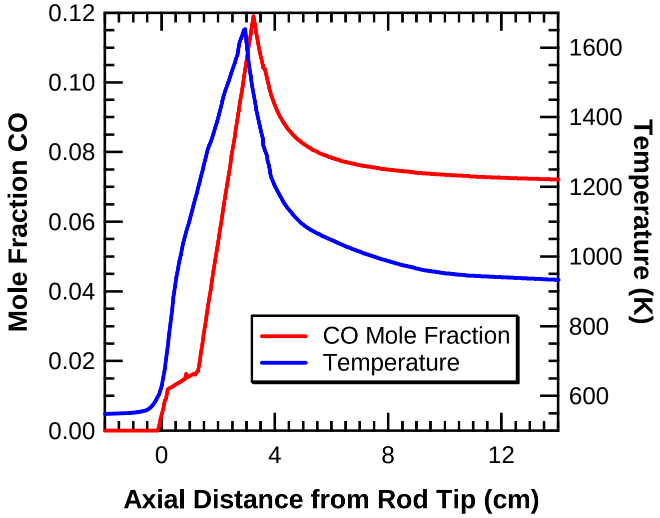

Figure 4-27. Predicted average temperature and CO mole fraction profiles for Case 8.

The profiles also showed that cooling starts at an earlier axial rod location for this case versus other cases. This was due to the decreased annular distance between the hot zirconia rod and the cool throat walls, providing more immediate cooling. The model predicted an average outlet temperature of 940 K and an average outlet CO composition of 7.20 mol%. The outlet CO represents a conversion of 7.76%, with a quenching efficiency of 57.3%. The conversion of CO from CO_2 increased by 12.3% compared to

Case 7. The quenching efficiency for Case 8 was slightly lower than for Case 7 due to increased reverse reaction kinetics during the initial stages of quenching that resulted from increased CO concentrations. The quenching efficiency was positively impacted by higher velocities in the narrow annulus which led to an increased convective heat transfer coefficient. Experimental results, obtained after the modeling, supported the modeling predictions for this case as well. Experimental outlet CO concentrations of between 7.75± 0.75 mol% were observed using a larger diameter zirconia rod operating at 6.0 slpm (Jensen, 2005).

Several factors led to increased conversion for Case 8 versus Case 7. First, the larger diameter rod led to greater thermal boundary layer area. This increased both the average temperatures and CO mole fractions. Second, the larger diameter rod caused higher velocities in the annular section of the device which led to greater cooling heat transfer in that section, as well as an increased pressure loss. Both the higher heat transfer and reduced residence time in the cool-down section positively impacted quenching. These modeling results agree with the experimental results for this case. Predictions for this case showed that increasing the zirconia rod diameter would increase CO conversion by 12% versus the reduced diameter case (Case 7).

4.3.2.5 Effects of Increased Operating Pressure

Two cases were modeled to show how changing the pressure affects converter performance. The operating pressure was set to 2.0 atm for both of these cases. The first high-pressure case (Case 9) had the same mass flow rate as Case 6. The second high-pressure case (Case 10) had a volumetric flow rate of 12 slpm to achieve similar velocities and residence times as Case 6. The radially-averaged temperature profiles for

Cases 9 and 10 were compared with those from Case 6 in Figure 4-28, with all cases similar in shape. The temperature profiles for Cases 6 and 9 were expected to be similar, based on the simplified calculations (from Section 4.3.1.4) that showed that increasing the pressure while maintaining the same mass flow rate should have no effect on the overall heat transfer. However, lower radially-averaged maximum temperatures were predicted for Cases 9 and 10 than for Case 6 (1590 K for Case 6, 1530 K for Case 9, and 1490 K for Case 10), which was most likely due to increased reaction kinetics at higher pressures. This meant more energy was driving the endothermic reaction of CO_2 to form CO and less energy was heating the gas. This same phenomenon in reverse caused the higher pressure cases to cool less quickly in the post-rod region. The predicted temperatures for Case 10 were lower than Case 9 throughout the reactor. This was also expected since the increase in heat transfer due to increased velocity was more than counteracted by the higher mass flow rate.

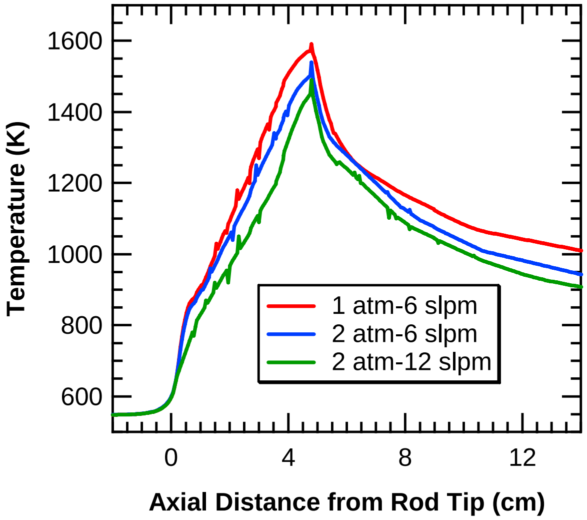

Figure 4-28. Predicted average temperature profiles for Cases 6, 9, and 10.

The CO mole fraction predictions for all three cases were also compared to analyze the impacts of pressure on the reaction kinetics and equilibrium. The predicted radially-averaged CO mole fraction profiles are shown in Figure 4-29. An outlet CO concentration of 5.85 mol% was predicted for Case 6, with 4.47 mol% for Case 9 and 5.05 mol% for Case 10. These outlet CO compositions correspond to outlet CO mass flows of 7.77 mg/s CO for Case 6, 5.85 mg/s CO for Case 9, and 13.29 mg/s CO for Case 10. A higher peak radially-averaged CO composition was predicted for Case 9 than for Case 6 (12.3 mol% versus 11.6 mol%). This increase was due to the increased reaction kinetics at higher pressure that causes higher initial production of CO. This increased production of CO also corresponds to the lower average temperatures seen in Figure 4-28 for Case 9. The increased residence time at high temperatures also enabled increased production of CO. Unfortunately the peak production of CO in this case was not preserved because of inefficient quenching due to increased kinetics of the reverse reactions of CO to CO_2, and increased residence time in the cooling region. Case 9 had a quenching effectiveness factor of 38.0% versus 53.5% for Case 6.

A lower peak radially-averaged CO composition was predicted for Case 10 than for Case 9 (10.7 mol% versus 12.3 mol%). This was due to the decreased residence time in the heating region in Case 10 that resulted in lower conversion of CO from CO_2. The outlet amount of CO was greater for Case 10 than Case 9 because the flow rate was twice as high. In addition, the decreased residence time in the cooling region reduced the impact of the reverse reactions of CO to CO_2. The quenching effectiveness factor for Case 10 was 49.6% compared to 38.0% for Case 9. These predictions showed that increasing the flow rate and the internal pressure resulted in a higher outlet amount of

CO. A 71.0% increase in the outlet mass flow rate of CO was predicted for Case 10 compared to Case 6.

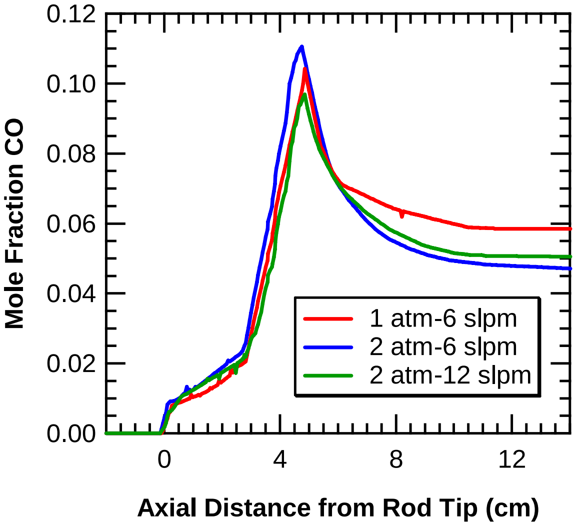

Figure 4-29. Predicted average CO mole fraction profiles for Cases 6, 9, and 10.

In summary, these predictions showed that increasing the pressure can increase the amount of CO produced, depending on the flow conditions. This increased CO production came as the result of faster overall reaction kinetics and increased heat transfer due to higher pressure. Higher pressure also caused faster reverse reaction kinetics and lowered equilibrium conversion which, in some cases, counteracted the increased reaction rates and heat transfer and resulted in lower overall CO yield. These predictions did not include the possibility of cooling the hot gases by quickly reducing the pressure using a sudden expansion or a shock. This would be an effective way to increase the amount of CO preserved, especially at higher pressures. These predictions showed that operating the converter at 2 atm and 12 slpm (Case 10) would increase the outlet amount of CO by 71% versus the 1 atm-6 slpm case (Case 6).

4.3.2.6 Helium Addition

The addition of helium was modeled in Case 11, with 25 mol% He in the inlet stream. This addition of helium corresponded to a lower overall mass flow rate (0.152 g/s versus 0.196 g/s for Case 6) in order to maintain a volumetric flow rate of 6.0 slpm. The predicted peak local temperature for Case 6 was 2623 K, and the peak local CO concentration was 17.1 mol%. The predicted radially-averaged temperature and CO mole fraction profiles are shown in Figure 4-30. These profiles were similar in shape and relative magnitudes to the other cases. The predicted maximum average temperature was higher for Case 11 than Case 6 (1640 K versus 1590 K), while the predicted outlet temperature was lower for Case 11 than Case 6 (990 K versus 1050 K). These temperature predictions correspond to greater heat transfer in both the heating and cooling regions, as expected with helium.

The peak radially-averaged CO conversion predicted for Case 11 was 11.9%, 2.6% higher than that predicted for Case 6, and the 6.52% outlet CO conversion predicted for Case 11 was 4.8% higher than for Case 6. The quenching efficiency increased to 54.6% for Case 11 (versus 53.5% for Case 6), meaning more effective quenching of the product mixture. The lower predicted peak and outlet CO compositions (8.22 mol% and 4.66 mol%) and lower outlet CO flow rate (6.11 mg/s) predicted for this case, versus Case 6, were the result of dilution of the CO_2 with He. Dilution with He did not affect reaction kinetics, in line with the theoretical analysis.

These predictions showed that the addition of helium increased heat transfer in the converter, causing better heating and cooling. This increase in heat transfer increased both the peak and outlet conversion of CO_2 to CO, but decreased the exit flow rate of CO, due to dilution of the CO_2 by the He.

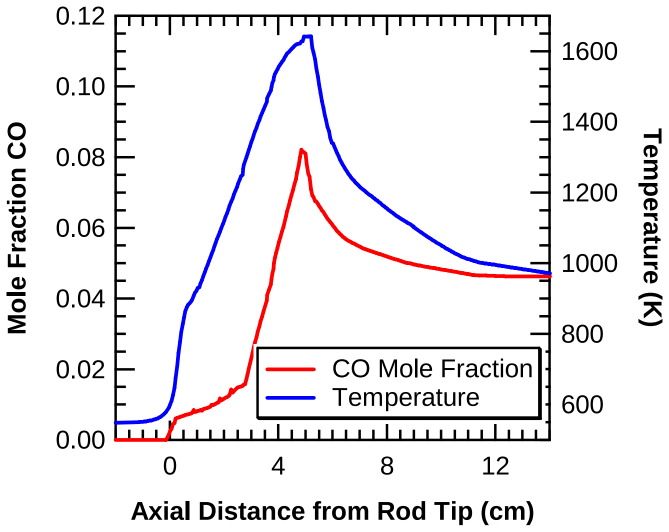

Figure 4-30. Predicted average temperature and CO mole fraction profiles for the 25 mol% He Case.

4.3.2.7 Conic Rod and Impaction Plate

A completely new geometry was modeled for Case 12. The idea behind this geometry was to increase the high-temperature surface area in order to convert more CO_2 in the thermal boundary layer. A second-generation converter was built by Jensen (2004) with a honeycomb type zirconia section exposed to the same high solar flux as the original converter. The honeycomb section was built from different cone-like surfaces drilled into a cylinder of zirconia, with exit holes at the tip of the cone-like void spaces. All zirconia surfaces exposed to the solar flux were assumed to be heated to 2623 K. Just behind this honeycomb zirconia, a cold impaction plate maintained at 800 K quenched the product mixture.

Model predictions for this geometry were performed for a flow rate of 10 slpm. For this flow rate, the Reynolds number in the throat was estimated to reach 2500, using the properties of CO_2 at 2200 K. This is close to the critical Reynolds number for internal flow of 2300, so this converter was assumed to operate in the turbulent flow regime. Laminar kinetic rates were still assumed because of the nature of the reaction scheme and the numerical difficulty of treating turbulence-chemistry interactions. The k-ε turbulence model was used to model the turbulent flow.

Figure 4-31 shows both the temperature and CO mole fraction profiles for this geometry. Because of the more complex geometry, average radial or axial profiles are not shown. The peak gas temperature was predicted to be 2623 K, with a peak CO composition of 21.6 mol%. An average outlet temperature of 1170 K was predicted, with an average outlet CO composition of 5.15 mol%. This outlet CO concentration corresponds to 12.2 mg/s, a 16.5% increase in the outlet amount of CO versus the base case. The outlet temperature was greater than all other cases because the impaction plate wall was modeled as 800 K. The predicted radially-averaged gas temperature and CO concentrations at the throat were 1610 K and 10.5 mol%. If these values represent the peak values, this converter has an overall quenching efficiency of 51.5%. It is anticipated that the outlet flow rate of CO and quenching efficiency would increase if the impaction plate temperature were decreased to a temperature (548 K) more representative of the other modeled cases.

The modeling predictions show that this conical design increased CO conversion due to greater high-temperature surface area of the conic zirconia surface, and better quenching by impaction with a cool wall. This geometry would have to be extended to three dimensions to more fully represent the honeycomb structure of the zirconia actually used experimentally by the Los Alamos Renewable Energy Corporation.

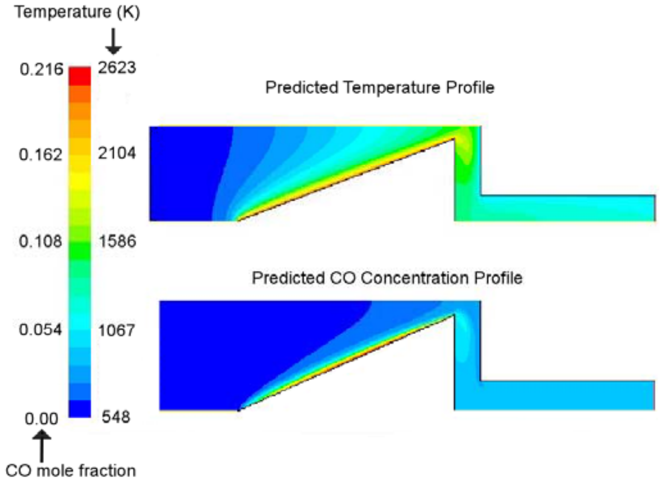

Figure 4-31. Predicted temperature and CO mole fraction profiles for Case 12.

4.3.3 Summary and Conclusions from Converter Improvement Studies

A summary of the results of the CFD simulations is presented in Figure 4-32. The outlet CO flow rate ($\dot{m}_{COout}$) and CO conversion were functions of the heat transfer to the gas, the kinetic rates of formation in the hot boundary layer of the solar-heated surface, and the rapid quenching in the cooling region to minimize the reverse reactions. The overall CO conversion was shown to be a strong function of residence time (especially in the high-temperature region), and average gas temperature. Cases with the highest average gas temperatures in the throat and highest residence times in the high-temperature region had the greatest CO conversions. In addition, reducing the residence time in the cooling region (while maintaining similar cooling rates) increased CO conversion by reducing reverse reactions of CO to CO_2.

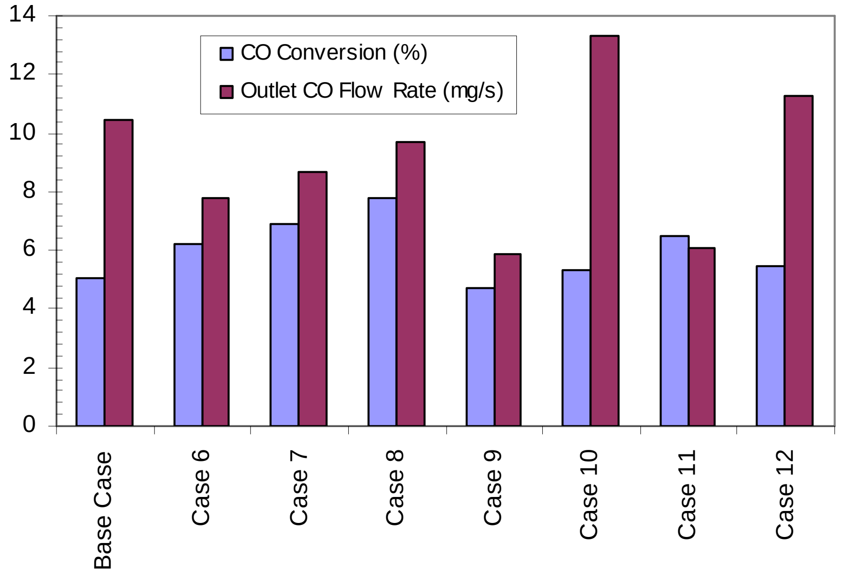

Figure 4-32. Summary of the prototype improvement studies.

Lowering the flow rate increases conversion but lowers the outlet CO flow rate. The use of a smaller cooled exit tube increased CO conversion, as did the use of a larger rod diameter (and corresponding smaller annulus at the throat). The use of helium increased heat transfer but lowered the outlet CO flow rate due to dilution of the CO_2 with He. Increasing the pressure by a factor of 2 was beneficial as long as the inlet mass flow rate increased by a factor of 2 as well, although lower quenching rates were predicted at increased pressure. The geometry change to increase the high-temperature surface area using a conical-type honeycomb showed promise for increasing conversion as well.

Several of these design modifications and operational adjustments have already been implemented experimentally (Jensen, 2005), and have increased the conversion of CO from CO_2, in agreement with predicted model trends. Continued efforts, both experimentally and computationally, are needed to achieve the CO conversion necessary to make this process economically viable.

4.4 Conclusions

The modeling work on the solar CO_2 converter prototype was successful in simulating the experimental conditions, based on agreement between predicted results and experimental results of outlet CO mol% and outlet temperature. Radiation modeling showed that the incoming radiative flux heated the zirconia rod, which then convectively heated the CO_2. CFD modeling also showed that the converter could be improved by several modifications, including increasing the zirconia rod diameter, decreasing the overall flow rate, increasing the operating pressure, decreasing the cool-down pipe diameter, and modifying the cool-down section. Several of these modifications (increasing zirconia rod diameter, decreasing overall flow rate, and decreasing cool-down pipe diameter) have already been made to the converter by Jensen and have proven to increase CO conversion, in line with CFD predictions. All this was done in an effort to improve the performance of the converter to make this process economically viable, which has the potential to provide fuel (H_2 or CO) and/or electricity without the production of greenhouse gases. The work on the solar CO_2 converter provides the first complete CFD model of a solar-energy-to-fuel-reactor.

5. Improved Coal Modeling Using STAR-CD

The objective of this research was to implement the advanced PCGC-3 coal submodels into STAR-CD, verify the accuracy of each submodel individually, and validate the overall accuracy of the combined submodels by comparison with experimental data. The implemented coal submodels include the coal setup and initialization subroutine, the basic coal reactions submodels, the CPD model, and the CBK model. It was initially proposed to implement the soot formation model, the deposition model, and the NO_X formation model into STAR-CD. Due to time constraints, these coal submodels were not implemented, and are not discussed in this section.

5.1 Implementation of Coal Submodels

Three devolatilization models were implemented into STAR-CD: the one-step devolatilization submodel (Anthony, et al., 1975), the two-step devolatilization submodel (Kobayashi, et al., 1976), and the CPD submodel (Grant, et al., 1989). The one-step submodel from PCGC-3 is similar to the one-step submodel already available in STAR-CD, but it contains a volatiles/char split parameter which is used to describe the reaction of coal to both volatile matter and char. Two char reaction submodels were also implemented: the nth-order char reaction submodel (Smith, et al., 1994), and the CBK moubdel (Hurt, et al., 1998). The nth-order submodel is similar to the 1st-order submodel except it allows for any reaction order of oxygen. In addition, the nth-order submodel also includes gasification reactions of char with CO_2 and H_2O.

The implementation of all the coal submodels involved modifying FORTRAN programs originally developed for PCGC-3. In two cases (CPD model and CBK model), stand-alone FORTRAN submodels provided the most updated code and were modified for implementation. General modifications included removing redundant variables that were passed from the STAR-CD CFD simulation, altering the output, and altering the structure of the submodel code to enable it to efficiently interface with STAR-CD. The following models were modified for implementation into STAR-CD:

- Coal setup and initialization subroutine,
- Water vaporization model,
- One-step devolatilization model,
- Two-step devolatilization model,
- Chemical percolation devolatilization (CPD) model,
- Nth-order char reaction model,
- Char burnout kinetic (CBK) model.

The modifications made to the submodels for implementation are described in this section. Copies of the FORTRAN code for these submodels, along with input and output files associated with the submodels are included in the CD included with this dissertation.

5.1.1 Coal Setup and Initialization Subroutine

This subroutine (originally taken from PCGC-3) was altered to remove redundant variables already available in STAR-CD, including the compositions determined from ultimate and proximate analysis. In addition, several comment statements were added to the code to assist in proposed future modifications. Future modifications that have been suggested include making all the setup and initialization variables available in GUI format, like other input variables used by STAR-CD, rather than requiring an additional input file. Several warning and error statements were also added to the code to facilitate proper model development.

5.1.2 Water Vaporization Model

This model did not require any major modifications. The only modifications were adjusting the code so that inputs and outputs could be passed between the submodel and STAR-CD. Inputs from STAR-CD include bulk water concentration, gas and particle temperatures, fraction of moisture in the particle, particle diameter, and time step. This model calculates the final fraction of moisture in the particle, and the vaporization rate.

5.1.3 One-step Devolatilization Model

This model did not require extensive modifications. Two modifications were made to this model. The first involved the addition of a time-step adjustor. The purpose of this time-step adjustor was to increase/decrease the time step for the calculation of devolatilization depending on the conditions. This devolatilization time step was independent of the overall time step given by STAR-CD. If devolatilization representing more than 5% of the total coal was predicted, the time step for devolatilization was reduced by 50%. If devolatilization of 0.5% or lower was predicted, the time step was increased by 20%. This modification enabled multiple devolatilization time steps to be taken for each overall time step supplied by STAR-CD. The overall devolatilization yields were calculated using the sum of all individual devolatilization time steps. The other modification made to this model was to adjust the model to allow inputs from STAR-CD. Inputs needed for this model include the devolatilization kinetic parameters (obtained from the initialization and setup subroutine), the coal conditions at the beginning of the time step, the particle temperature, and the overall particle time step. The model calculates the coal conditions at the end of the time step assuming a constant temperature over the entire time step. Important coal conditions calculated by this model are the fraction of coal that devolatilized during the time step, the fraction of coal that reacted to form char during the time step, and the remaining fraction of unreacted coal.

5.1.4 Two-step Devolatilization Model

This model required the same changes as the one-step devolatilization model. A time-step adjustor was added to this model, with the same adjustment conditions as the one-step model. This model required an additional set of reaction-rate parameters for the second devolatilization reaction of coal. The two-step model calculates the same parameters as the one-step model (fractions of volatiles, char, and unreacted coal).

5.1.5 Chemical Percolation Devolatilization (CPD) Model

The CPD model was modified for implementation into STAR-CD. This was more complex than the simple devolatilization models, since the most advanced CPD model was a stand-alone version. The stand-alone version was developed for a single temperature history, particle size, and coal type. This code also had an algorithm for determining appropriate time steps. Modifications made to the CPD model for implementation purposes included: (1) alteration of the time-step algorithm, and (2) various code alterations that enable interchange between the CPD model and STAR-CD. The modified code can be found on the CD that accompanies this dissertation.

The modifications made to the time-step algorithm allowed for the calculation of devolatilization during an overall particle time step given by STAR-CD. The stand-alone version of the CPD model used an independent devolatilization time step, which was adjusted depending on volatiles fraction and labile bridge fraction, to insure accuracy. The same conditions (>5% or <0.5%) were used for adjusting the time step as those used in the one-step and two-step devolatilization models. If the devolatilization time step was less than the overall time step, multiple time steps were calculated for the CPD model to return the overall devolatilization rate during the particle time step given in STAR-CD.

The alterations made to the stand-alone CPD model included separating it into two distinct subroutines: an initialization subroutine and a reaction subroutine. The initialization subroutine is called at the introduction of a new particle and initializes all the necessary devolatilization parameters. The devolatilization behavior of the particle is then calculated using the reaction subroutine throughout its history. The CPD model was also modified so that the temperature, pressure, initial coal conditions, and overall time step could be passed between STAR-CD and the CPD model. The CPD model calculates and returns the final coal conditions at the end of the time step, including the fraction of coal that devolatilized during the time step, the fraction of coal that formed char during the time step, and the fraction of coal that remains unreacted. Other variables are also calculated using the CPD model, including the light gas and tar fractions of the volatiles and the evolution of the nitrogen during devolatilization. These variables are not currently used by STAR-CD, but may be used in the future because of their importance in calculating coal-derived NO_X and soot formation.

5.1.6 Global Nth-order Char Reaction Model

This model required little change for successful implementation. The only changes to this model were interfacing the model with STAR-CD. Parameters for this model that come from STAR-CD include the bulk concentrations of oxygen, water, and CO_2, the bulk temperature, the particle diameter, the particle temperature, the particle char fraction, and the overall reaction time step. The kinetic parameters for all char reactions, as well as the particle pore area coefficient (ζ), come from the setup and initialization subroutine. This model calculates the fraction of char that oxidized, and the final char conditions (diameter and remaining char fraction).

5.1.7 Char Burnout Kinetic (CBK) Model

The most updated CBK model was a stand-alone code, known as CBK-8. This model calculates burnout based on an iterative method that solves for three variables: the oxygen concentration at the particle surface, the particle temperature, and the char oxidation rate. This iterative approach is unnecessary for calculating char oxidation in CFD simulations because the particle temperature is solved using the overall energy equation. Due to the similarities between the global nth-order char reaction model and the CBK model, it was decided that complementing the global nth-order char reaction model with the three additional subroutines of the CBK model would be the best option. The thermal annealing subroutine, the ash inhibition subroutine, and the reaction effectiveness subroutine were added to the nth-order char reaction model as distinct subroutines. This required the addition of several parameters to the nth-order model, and some minor changes to the calculation of the char reaction rate. This model calculates the total char reaction rate, the fraction of char remaining, and the final char diameter.

5.2 Verification of Coal Models

Verification of model predictions are important because they demonstrate that a model can accurately describe a physical process or variable. Typically, verification involves comparison between the predictions of a single model and experimental data collected for the actual process or variable being modeled. For the coal models, experimental data are available for devolatilization, char oxidation, and char gasification. All of the models that were implemented were verified previously, but, because all the submodels were altered for implementation, all submodels were verified again. This verification is to show agreement with experimental data, as well as to show that the submodels alterations did not affect its calculations.

5.2.1 Verification of Devolatilization Models

All three devolatilization models were tested for accuracy by comparing the implemented model predictions with data taken by Gibbins-Matham and Kandiyoti (1988). The experimental data contain temperature-volatiles histories for two heating rates, 1000 K/s and 1.0 K/s, for a Pittsburgh No. 8 Coal, and were measured in a wire mesh apparatus. The 1-step model used the devolatilization reaction-rate parameters of Solomon, et al. (1986), with the volatile-char split parameter (Y) calculated by the overall volatile content of the coal as determined by proximate analysis. The 2-step model used the devolatilization reaction-rate parameters and volatile-char spilt parameters of Ubhayakar, et al. (1977). All necessary reaction-rate constants for these models are found in Table 5-1. The CPD model used the reaction-rate constants and coal structural parameters of Fletcher and Kerstein (1992) for a Pittsburgh No. 8 Coal. Table 5-2 contains the structural parameters used by the CPD model for a Pittsburgh No. 8 Coal.

Table 5-1. Reaction-rate parameters for coal devolatilization.

Model	Reaction	Y	A_{rxn} (1/s)	E_{rxn} (kJ/mol)	σ_{rxn} (kJ/mol)
1-Step Model	Reaction 1	0.60	4.3×10^{14}	2.29×10^{2}	
	Reaction 1	0.40	3.7×10^{5}	7.36×10^{1}	-
2-Step Model	Reaction 2	0.80	1.5×10^{13}	2.51×10^{2}	-
	Bridge Scission	-	2.6×10^{15}	2.32×10^{5}	7.53
	Gas Release	-	3.0×10^{15}	2.51×10^{5}	33.9
CPD Model	Cross-linking	-	3.0×10^{15}	2.72×10^{5}	-
	HCN Release		9.0×10^{17}	4.18×10^{5}	7.14×10^{4}

Table 5-2. CPD model structural parameters for a Pittsburgh No. 8 Coal.

Parameter	Value	Description
p_0	0.62	Initial fraction of intact bridges
$\sigma + 1$	4.5	Coordination number (average attachments per cluster)
$M_{cluster}$	294	Average cluster molecular weight (g/mol)
m_δ	24	Average side-chain molecular weight (g/mol)
c_0	0.0	Initial fraction of char (non-reactive) bridges

The predictions of volatiles released at a heating rate of 1000 K/s for the 1-step, 2-step, and CPD models are shown in Figure 5-1, along with the experimental data. Figure 5-2 shows the same predictions and data for a heating rate of 1 K/s. The predictions of all three devolatilization models show good agreement with the experimental data for the 1000 K/s case. As expected, the CPD model appears to agree more closely with the data than the one-step or two-step devolatilization models, and accurately predicts devolatilization from onset to completion. For this high heating rate, both the one-step and two-step models accurately predict the overall volatiles released from the coal, but predict that devolatilization starts at a higher temperature than seen experimentally. For the 1 K/s heating rate, all three models do not accurately predict the total volatiles released from the coal, although all three models agree within 15% of the experimental data. The CPD and two-step models appear to agree more closely with the experimental data than the one-step model. These verification results also showed that the implementation did not affect the devolatilization predictions.

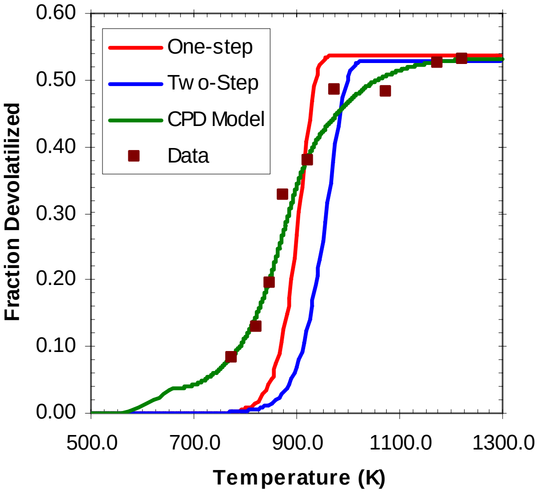

Figure 5-1. Fraction volatiles released versus temperature for a heating rate of 1000 K/s.

The most important devolatilization prediction is the overall amount of volatiles released from the coal, and all three devolatilization models appear to accurately predict overall devolatilization, especially at the high heating rate. It is more important to accurately predict devolatilization for high heating rates versus low heating rates because typical heating rates in a pulverized coal utility boiler are of the order of 10^5 K/s. The CPD model is the model that is recommended for accuracy in modeling devolatilization, but is slightly more computationally intensive than the other two devolatilization models.

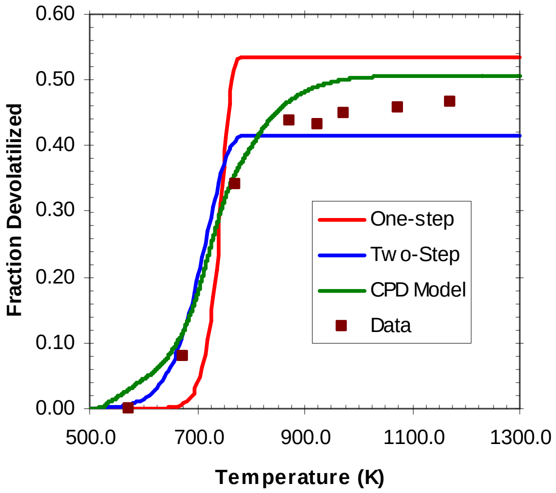

Figure 5-2. Fraction volatiles released versus temperature for a heating rate of 1 K/s.

5.2.2 Verification of Char Oxidation Models

The global nth-order char reaction model and the char burnout kinetic (CBK) model were also tested for accuracy. Accuracy was determined by comparison of model predictions with data from Hurt, et al. (1998). Data were obtained for a variety of chars, and give mass loss versus time for a given constant temperature. These char oxidation experiments were performed using air (21% O_2, 79% N_2) at 1000 K. The global nth-order char reaction model had reaction-rate parameters for the three char reactions from Goetz, et al. (1983). These kinetic parameters are found in Table 5-3 for a high-volatile C bituminous coal, consistent with the experiments performed using Illinois #6 coal char.

Both models used the input parameters (temperature, pressure, bulk species concentrations) given in the experiments for a 55-µm char particle. In addition, the global nth-order model assumed a pore surface area coefficient (ζ) of 1.0. The predictions for the two models and the experimental data are found in Figure 5-3.

Table 5-3. Kinetic parameters for the three char reactions.

Reaction	Pre-exponential Factor (m/K^{b}s)	Temperature Exponent (b)	Activation Energy (kJ/mol)	Reaction Order (n)
Char + $O_2 \rightarrow CO_2$	1.03	1.0	7,490	1
Char + $CO_2 \rightarrow 2\ CO$	1160	1.0	26,000	1
Char + $H_2O \rightarrow CO + H_2$	42,600	1.0	31,600	1

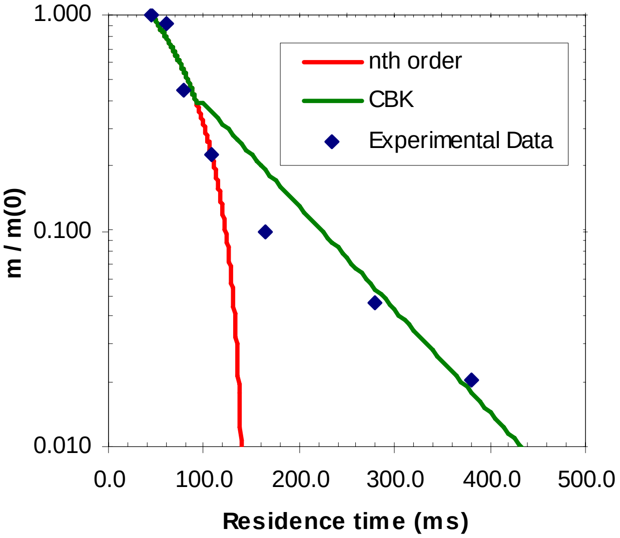

Figure 5-3. Burnout predictions for the global nth order and CBK models.

Both models were fairly accurate (within 5% below 90% burnout) in modeling the majority of burnout, but the CBK model better predicted late-stage burnout ($m/m_0<0.10$, or 90% burnout), as it was designed to do. This was due to the ash inhibition and thermal annealing models specifically designed to predict late-stage burnout. The global nth-order char reaction model predicted complete burnout of the char in 140 ms, while the CBK model predicted 99% burnout in 430 ms. Because both models are fairly accurate in modeling the majority of char combustion burnout (0-90% burnout), both models could be used in modeling coal combustion. The CBK model is most useful in cases where predictions of carbon in fly ash are important.

5.3 Validation of Coal Submodels

The implemented models were tested to prove the capability of the overall code by modeling a pulverized coal reactor using STAR-CD. This validation was performed by modeling an apparatus where experimental data were available. This validation was performed by testing all five implemented models in three validation cases: 1) one-step devolatilization model and global nth-order char reaction model, 2) two-step devolatilization model and global nth-order char reaction model, and 3) CPD model and CBK model. The coal setup subroutine and the water devolatilization model were used in all cases. This validation was not meant to be an exhaustive analysis of the apparatus, but, rather, to demonstrate the enhanced capabilities of STAR-CD to more accurately predict coal combustion. These validation cases were also compared with a case modeled using the original STAR-CD coal combustion models (1-step devolatilization and 1st-order char oxidation). In all, four cases were used in these validation results.

5.3.1 Computational Modeling Setup and Details

Several entrained flow coal combustion experiments were performed in the Controlled Profile Reactor (CPR) at BYU (Sanderson and Germane, 1993, Tree, et al., 1998). This apparatus, shown in Figure 5-4, consists of a down-fired cylindrical combustion chamber 240 cm long and 80 cm in diameter. At the top of the apparatus, coal and air were injected into the combustion chamber using a variable swirl burner. All combustion chamber walls were heated electrically to maintain as constant a wall temperature as possible throughout the reactor. This facility was designed to burn several varieties of fuel including natural gas, coal, and biomass.

These experiments were performed using a variety of coals. For the case that was modeled, experiments were performed by Sanderson, et al. (1993) using Utah Blind Canyon Coal. Sanderson also performed proximate and ultimate analyses on this coal, with results shown in Table 5-4 (1993). Several parameters were varied during these experiments including the swirl, equivalence ratio (secondary air flow rate), and particle size. One of these experiments was modeled for validation purposes. This experiment had inlet conditions summarized in Table 5-5. These experiments have been previously validated by Tree, et al. (1998). The purpose of this section is not to validate the experimental data, but to validate the implemented coal submodels using STAR-CD.

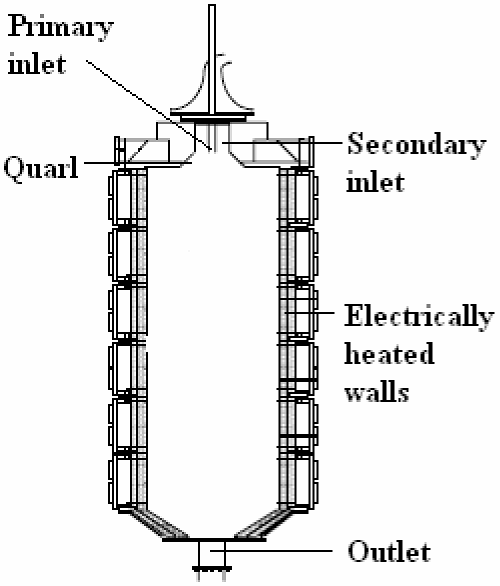

Figure 5-4. Schematic for the Controlled Profile Reactor (CPR).

Table 5-4. Ultimate and proximate analysis of Utah Blind Canyon coal.

Proximate Analysis (mass %, as received)	
Moisture	8.54
Ash	13.25
Volatile	39.35
Fixed Carbon	38.86
Heating Value (kJ/kg)	5476
Ultimate Analysis (mass %, dry basis)	
Carbon	69.13
Hydrogen	5.18
Oxygen	9.37
Nitrogen	1.34

Table 5-5. Inlet conditions for the coal validation case.

Inlet Parameter	Value
Coal Flow Rate (kg/s)	0.00317
Primary Air Flow Rate (kg/s)	0.00417
Primary Air Temperature (K)	289
Secondary Air Flow Rate (kg/s)	0.03528
Secondary Air Temperature (K)	533
Mass-mean particle size (μm)	55
Swirl Number	1.4
Equivalence Ratio	1.15

The combustor was modeled using a two-dimensional geometry, accounting for the symmetry of the combustor. A grid dependency study was performed by comparison of the predicted outlet temperature profile. For this case two grids were constructed, a course grid and a ½ size grid. Predictions for both grids gave similar results (within 2%) for the outlet temperature profile. Due to long convergence times, only the coarse grid was used for all results. This grid had 22,134 grid cells, with grid cells packed preferentially into the near-burner region and around the quarl.

The combustor was assumed to operate under steady-state conditions. The RNG k-ε turbulence model already available in STAR-CD was selected to predict turbulence in the reactor, with all constants having their default values. The SIMPLE algorithm was used to model the pressure-velocity coupling. The momentum, energy, and all species equations were solved using the first-order upwind scheme. Fluid properties (density, viscosity, thermal conductivity, heat capacity) were all defined using temperature-dependent expressions.

The inlet conditions were taken from the experiment. It was necessary to calculate the inlet gas velocities of the primary and secondary streams. The primary gas had a downward axial velocity of 26.6 m/s, with the secondary gas having a downward axial velocity of 7.96 m/s and a tangential velocity of 11.14 m/s. Coal particles were assumed to enter the combustor at the same velocity as the primary gas. The size of all coal particles was assumed to follow a Roslin-Ramler distribution curve with a mean of 55 μm and a standard deviation of 7 μm. The quarl and the top combustor wall were modeled using adiabatic boundary conditions because they were lined with a thick layer of refractory. The side combustor walls were modeled as having a constant temperature of 800ºC maintained by electrical heaters.

It was also necessary to define a gas-phase "species" that represents the volatiles released from coal during devolatilization. The important properties of this fictional molecule are its elemental composition, enthalpy, heat capacity, and molecular weight. All other properties are assumed to be those of air. The elemental composition of the volatiles is determined by assuming that all of the hydrogen and oxygen in the coal are released as volatiles, leaving char that consists of only carbon (and inert ash). For the Utah Blind Canyon coal, the volatiles have the simplified molecular formula

($CH_{2.333}O_{0.264}N_{0.043}$) and an average molecular weight of 18.87 g/mol. The volatiles are assumed to react in the gas phase according to Reaction 5-1.

$$\text{Volatiles} + 0.153\, O_2 \rightarrow 0.583\, CH_4 + 0.417\, CO + 0.021\, N_2 \qquad \text{(Reaction 5-1)}$$

This reaction was modeled using the eddy dissipation model, described in the Literature Review Section (2.1.3), with mixing parameters found in Table 5-6. This simplified volatiles reaction had an assumed heat of reaction (ΔH_r) of 0.0 kJ/kmol. This was accomplished by calculating an appropriate heat of formation and heat capacity for the volatiles "species" so that the heat of reaction remains negligible under devolatilization conditions (temperatures between 300 K and 1200 K).

Three global gas-phase reactions were also modeled using the eddy dissipation model. These reactions, and their mixing parameters, are also found in Table 5-6. The "use products" designation in Table 5-6 is an option that specifies whether product concentrations are used in determining the reaction rate.

Table 5-6. Gas-phase reactions modeled for the validation cases.

Reaction	A	B	Use Products
Reaction 5-1	30.0	10.0	No
$CH_4 + \frac{1}{2} O_2 \rightarrow CO + 2 H_2$	11.0	2.75	Yes
$CO + \frac{1}{2} O_2 \rightarrow CO_2$	2.1	0.53	Yes
$H_2 + \frac{1}{2} O_2 \rightarrow H_2O$	3.1	0.75	Yes

5.3.2 Validation Results and Discussion

Predictions from the four simulations are found in Figure 5-5, Figure 5-6, Figure 5-7, and Figure 5-8. These results show temperature, O_2, CO_2 and volatiles predictions,

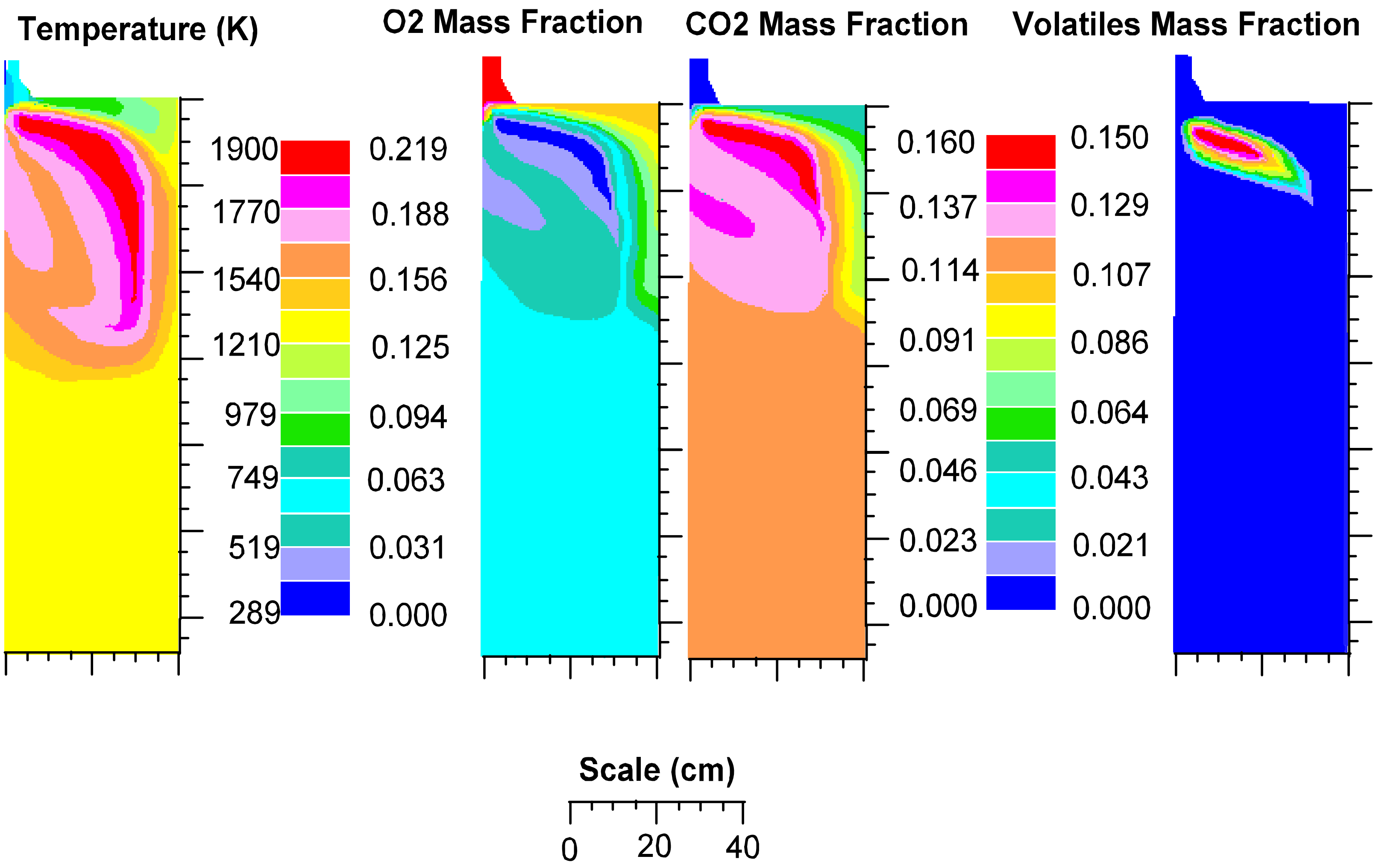

Figure 5-5. Predicted temperature, O_2, CO_2, and volatiles profiles using the original STAR-CD coal submodels.

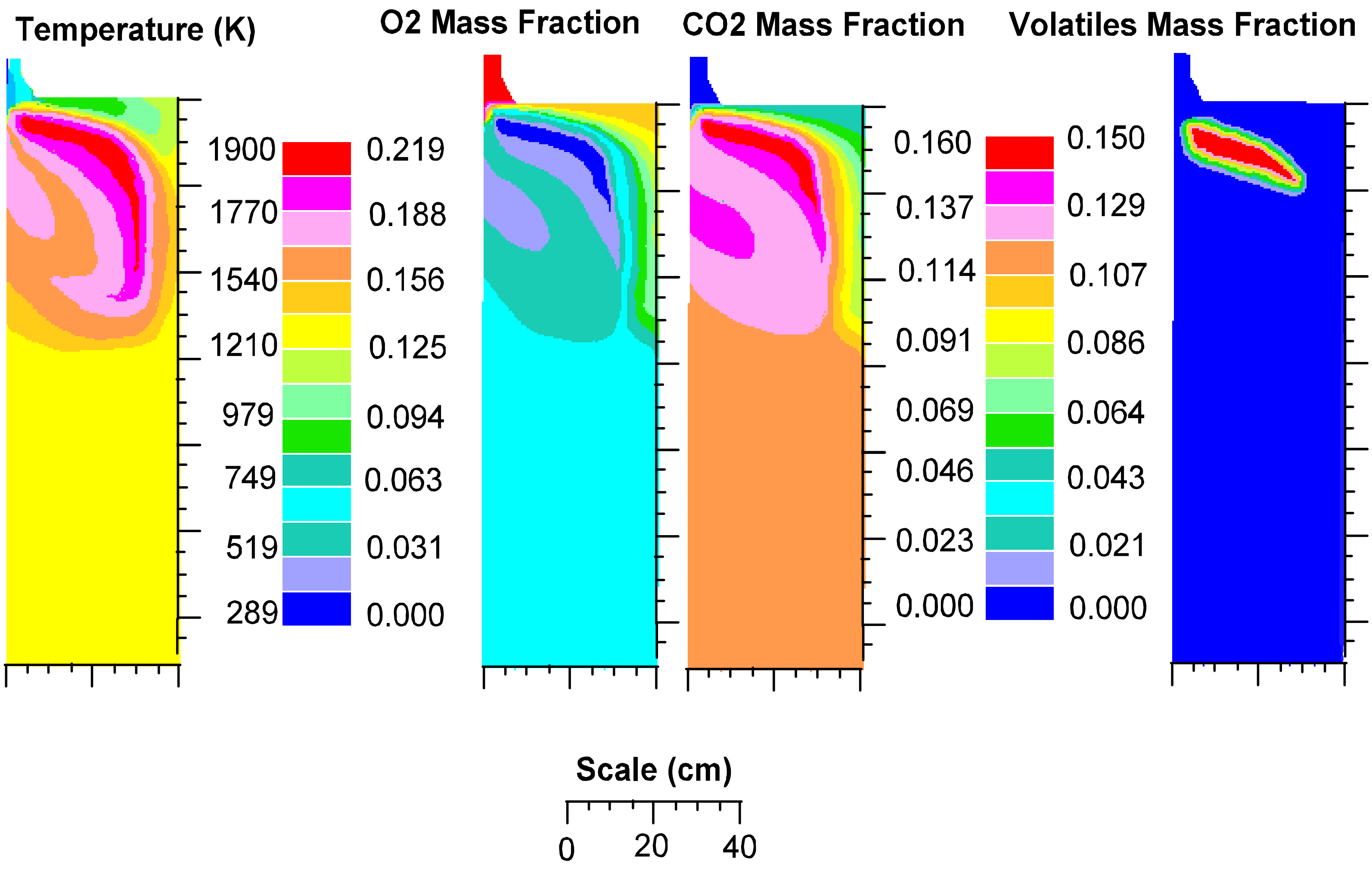

Figure 5-6. Predicted temperature, O_2, CO_2, and volatiles profiles using the one-step devolatilization model and global nth-order char oxidation submodels.

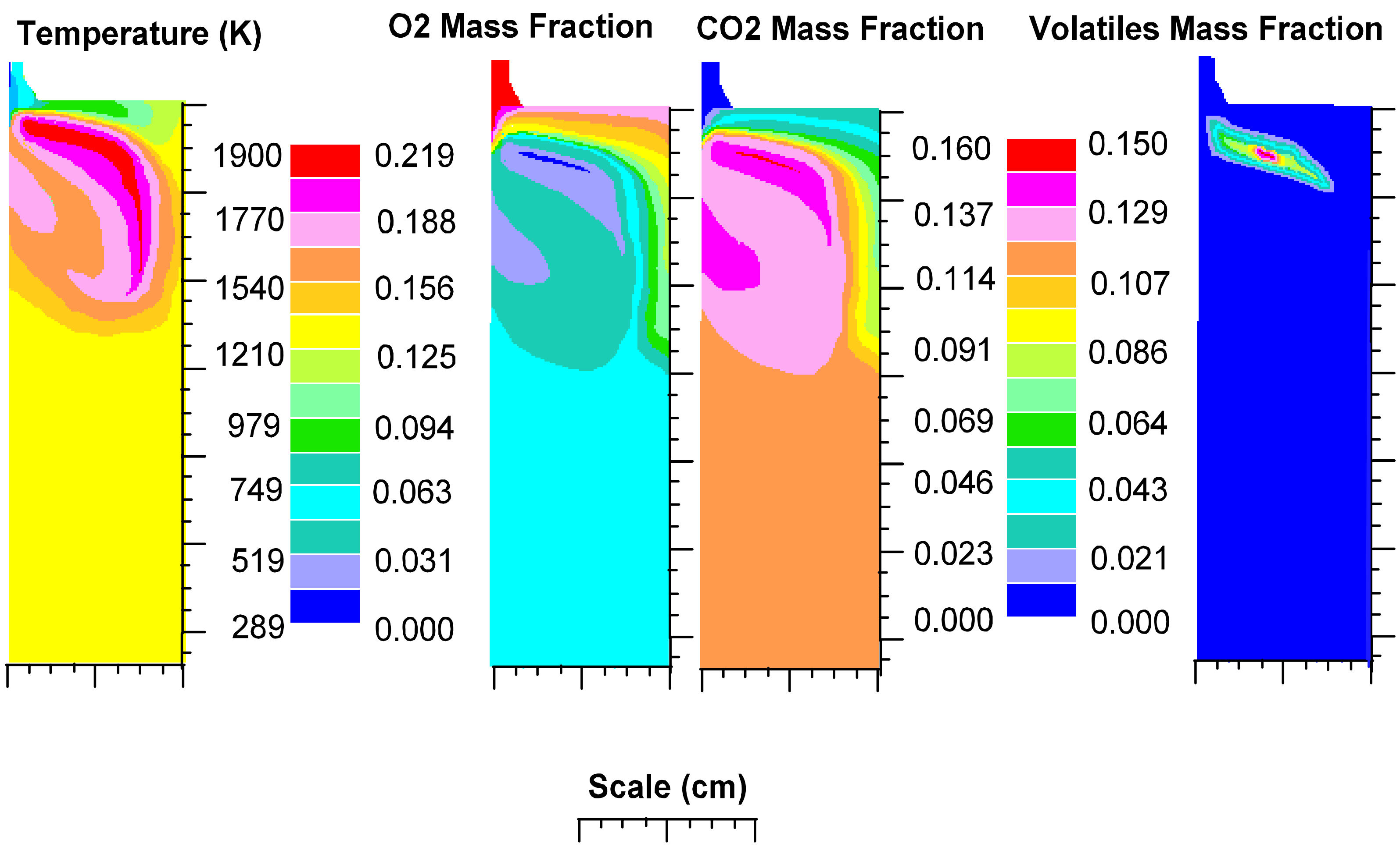

Figure 5-7. Predicted temperature, O_2, CO_2, and volatiles profiles using the two-step devolatilization model and global nth-order char oxidation submodels.

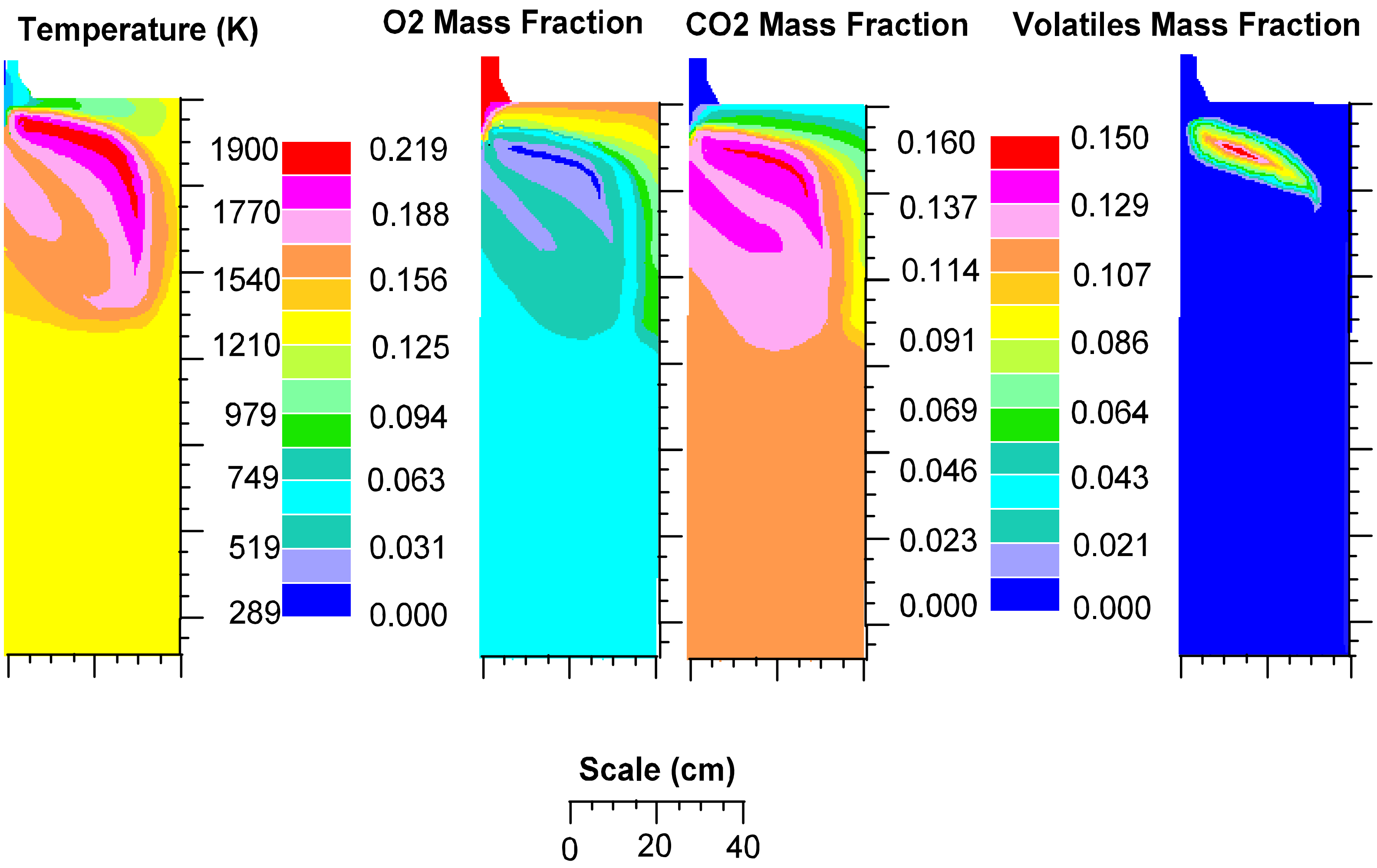

Figure 5-8. Predicted temperature, O_2, CO_2, and volatiles profiles using the CPD and CBK submodels.

and were normalized for comparison purposes. These results show good agreement with each other. All profiles have similar relative maxima and minima.

5.3.2.1 Velocity Predictions

Velocity predictions were quite similar for all four cases, so only the velocity vector profile using the original STAR-CD coal submodels is shown in Figure 5-9. All velocity profiles showed the existence of both central (CRZ) and side recirculation zones (SRZ). The CRZ was predicted at axial distances of 30-50 cm. All profiles showed fairly uniform flow starting at an axial distance of 70 cm, consistent with the experimental data. Experimental data show an central recirculation zone at axial distances between 20-60 cm, followed by fairly uniform temperatures (Tree, et al., 1998).

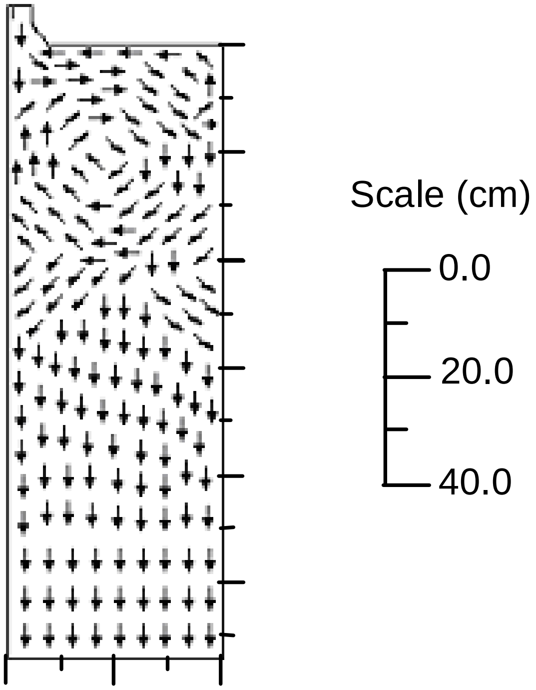

Figure 5-9. Predicted velocity flow field for the CBR using the original STAR-CD models.

5.3.2.2 Temperature Predictions

All temperature profiles show an intense flame which spreads toward the side walls by the swirl of the secondary stream. The predictions also show a relatively condensed flame front due to the effectiveness of the central recirculation zone (CRZ), which recirculated high-temperature gases to the flame front. All predictions showed a relatively short axial reaction zone (≈60 cm) followed by fairly uniform temperatures. This was in agreement with experimental data which showed fairly uniform temperature and species profiles starting at an axial distance of 75 cm. The original STAR-CD coal model predicted the highest peak local temperature, 2103 K. This value varied quite significantly from the other models, whose prediction of peak temperature showed better agreement with each other. The one-step devolatilization-global nth-order char oxidation model predicted a peak temperature of 1945 K. The two-step devolatilization-global nth-order char oxidation model predicted a peak temperature of 1910 K, with a peak volatiles fraction of 17.6%. The CPD-CBK model predicted the lowest peak temperature, 1905 K.

Predicted centerline axial temperature profiles, shown in Figure 5-10, showed decent agreement between all model predictions and experimental data. The three PCGC-3 models predicted similar temperatures and agreed within 3% of each other. The original STAR-CD coal model had a similar shape to the other models, but predicted higher centerline temperatures throughout the reactor. This was most likely due to over-prediction of devolatilization in the flame front. All models under-predicted the size and effectiveness of the central recirculation zone, and predicted lower temperatures than seen experimentally. There could be several reasons for this under-prediction. The most likely cause was the k-ε turbulence model, which typically under-predicts recirculation zones in swirling flows (Sloan, et al., 1986). Under-prediction of recirculation led to lower predicted recirculation temperatures for all models.

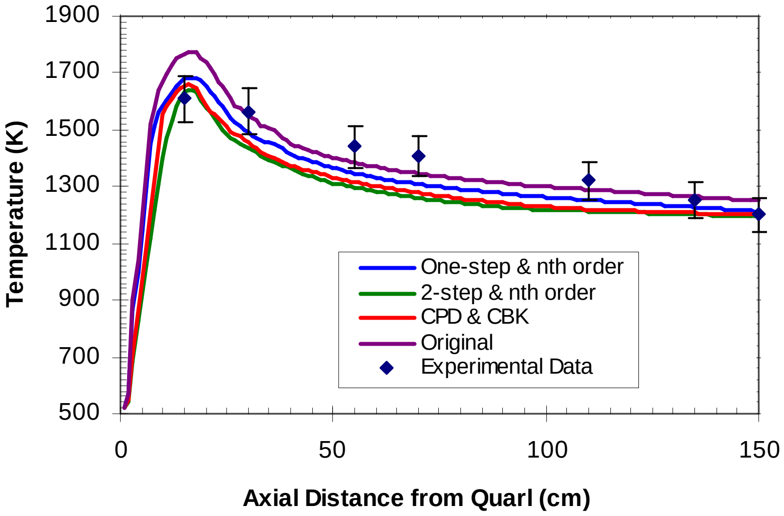

Figure 5-10. Predicted and measured centerline temperatures in the CPR.

All models also over-predicted peak centerline temperatures. This was most likely due to no soot formation submodel being used for these predictions. Including a soot formation model has been shown to lower peak flame temperatures by as much as 300 K (Fletcher, et al., 1997). The eddy-dissipation model (Magnussen and Hjertager, 1976) has also been known to over-predict combustion reactions in the flame-front region, causing over-predicted temperatures. The temperature predictions from the three new STAR-CD models agreed within 10% of all the experimental temperatures, with the original STAR-CD model agreeing within 15% of the experimental temperatures.

Predicted radial temperature profiles at two axial locations (15 cm and 150 cm) were also compared with experimental data. The first axial location (15 cm) was taken to correspond to a location within the flame front region, and its temperature profile is found in Figure 5-11. The flame-front radial profile showed a wide range of temperature predictions, with peak radial values varying from 2008 K for the original STAR-CD coal model to 1820 K for the CPD-CBK model. All models failed to accurately match the experimental data, but did capture the correct radial trends in this region, a slight decrease followed by an increase while moving outward which peaks at a radial distance between 22 and 25 cm. The temperature then decreased until it reached the wall temperature (800ºC). This over-prediction was most likely due to the causes mentioned previously, specifically lack of a soot formation model and over-prediction of gas-phase combustion by the eddy-dissipation model.

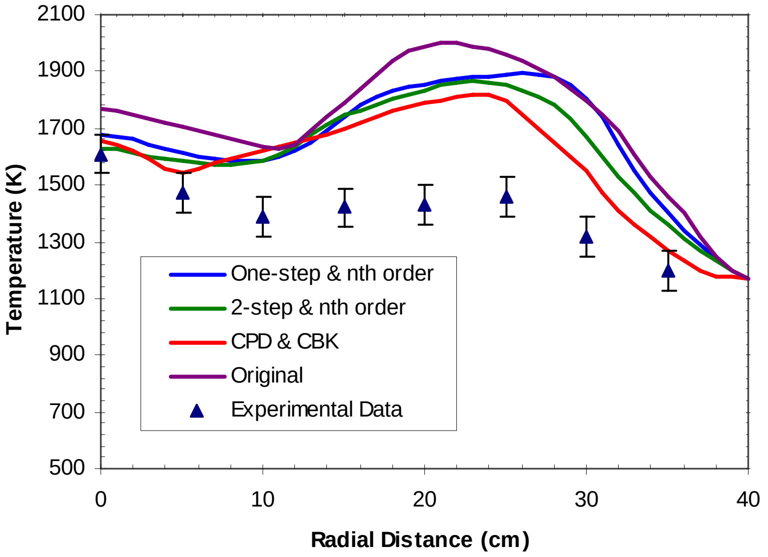

Figure 5-11. Predicted and measured radial temperatures at an axial distance of 15 cm.

The second radial temperature profile (150 cm) was taken to correspond to a location downstream of the intense flame region, and showed fairly uniform radial temperatures that ranged from 1100 K to 1200 K, as seen in Figure 5-12. This profile showed good agreement (<5%) between all model predictions, as well as between most model predictions and experimental data. The predictions from the original STAR-CD coal model were the most inaccurate (7.5% error). This was most likely due to the higher peak temperatures predicted earlier in the reactor. All other models predicted temperatures that varied by at most 4% from the experimental data.

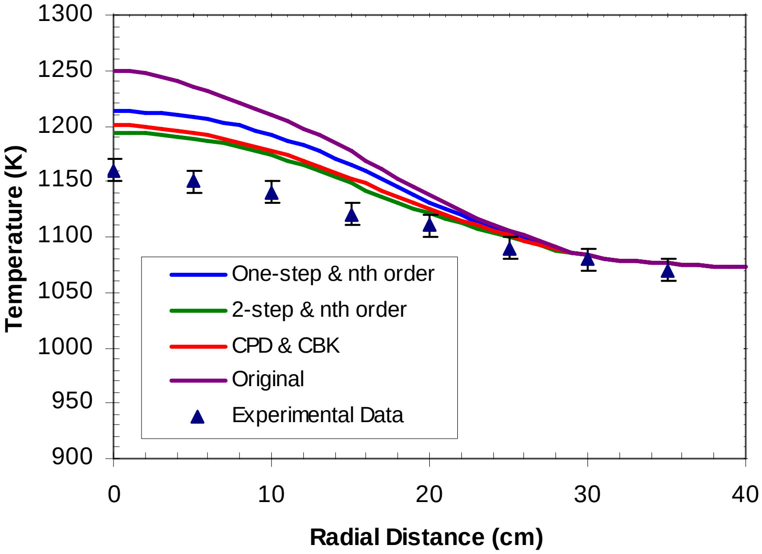

Figure 5-12. Predicted and measured radial temperatures at an axial distance of 150 cm.

5.3.2.3 Species Predictions

The O_2, CO_2, and volatiles predictions from all four validation cases were also in good agreement with one another. All cases predicted O_2 compositions between 0.3 mol%, which occurred in the highest temperature portion of the flame, and 21.9 mol%, which occurred in both inlets prior to the onset of combustion. Predicted peak CO_2 compositions ranged between 16.0 mol% (2-step devolatilization-global nth-order char oxidation submodel case) and 19.2 mol% (original STAR-CD submodels case), and occurred in the highest temperature areas of the flame. The shapes of all volatiles profiles were also quite similar, with peak volatiles concentrations corresponding to the highest temperature portions of the reactor. The original STAR-CD model predicted the highest peak volatiles fraction, 23.2%. The one-step devolatilization-global nth-order char oxidation model predicted a peak volatiles fraction of 17.3%. The two-step devolatilization-global nth-order char oxidation model predicted a peak volatiles fraction of 17.6%. The CPD-CBK model predicted the lowest peak volatiles fraction, 16.8%.

Predicted centerline axial oxygen profiles, shown in Figure 5-13, also showed excellent agreement between models, as well as with experimental data. All four CFD predictions showed similar oxygen profiles and agreed to within 3% of experimental O_2 data, and predicted centerline exit oxygen mass fractions of between 4.5-4.6%, compared with an experimentally measured value of 4.61%. All models predicted steeper declines in oxygen during the initial stages of combustion than seen experimentally (between 0 and 30 cm). All models also predicted low-oxygen zones between 20 and 40 cm, which corresponded to the central recirculation zone seen in both the velocity and temperature profiles. This agreed with the experimental data, which showed the low-oxygen zone (and thus the central recirculation zone) occurring between 30 cm and 60 cm. The differences between predictions and data were probably due to a combination of the k-ε turbulence model and the eddy dissipation model.

Predicted radial oxygen profiles at two axial distances (15 cm and 150 cm) were also compared with experimental data. The first axial location had predicted and measured radial O_2 profiles shown in Figure 5-14. All models under-predicted oxygen at this axial distance, but did capture the correct radial trends in this region, with oxygen decreasing to a minimum at 8-12 cm, and then increasing the remainder of the radial distance. The reason that all models under-predicted the oxygen concentrations at this location was the coupling of the oxygen continuity equation with the energy (temperature) equations. Over-predicted temperatures led to increased reaction rates (both gas-phase and particle-phase), which lowered oxygen concentrations in this area.

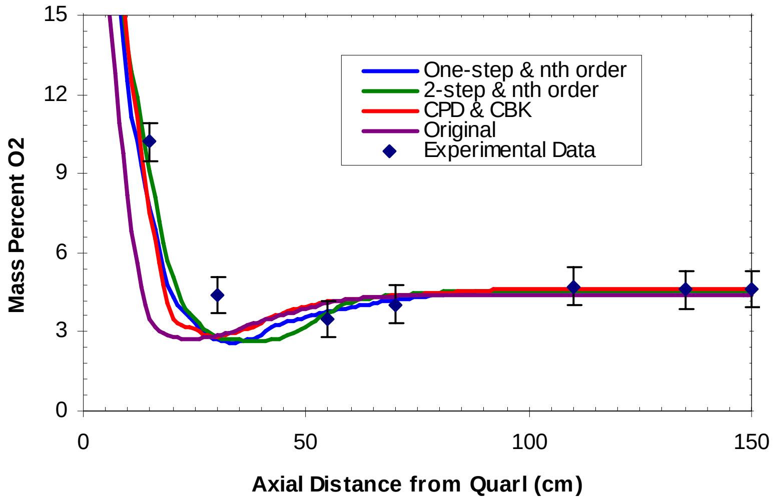

Figure 5-13. Predicted and measured centerline oxygen concentration profiles in the CPR.

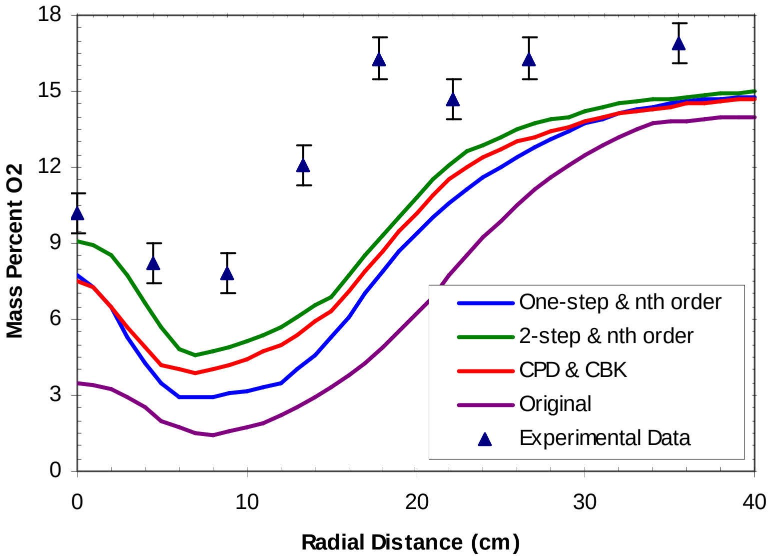

Figure 5-14. Predicted and measured radial O_2 concentrations at an axial distance of 15 cm.

The second radial oxygen profile (150 cm) was taken to correspond to a location downstream of the intense flame region, and showed fairly uniform radial oxygen concentrations that ranged from 4.4% to 4.7%, as seen in Figure 5-15. All model predictions showed excellent agreement (<1%) with each other and experimental data. The radially-averaged O_2 predictions from the original STAR-CD case were the lowest (4.5% O_2) while the CPD-CBK case predictions were the highest (4.7% O_2), and both agreed well with experimental O_2 concentrations of 4.7%.

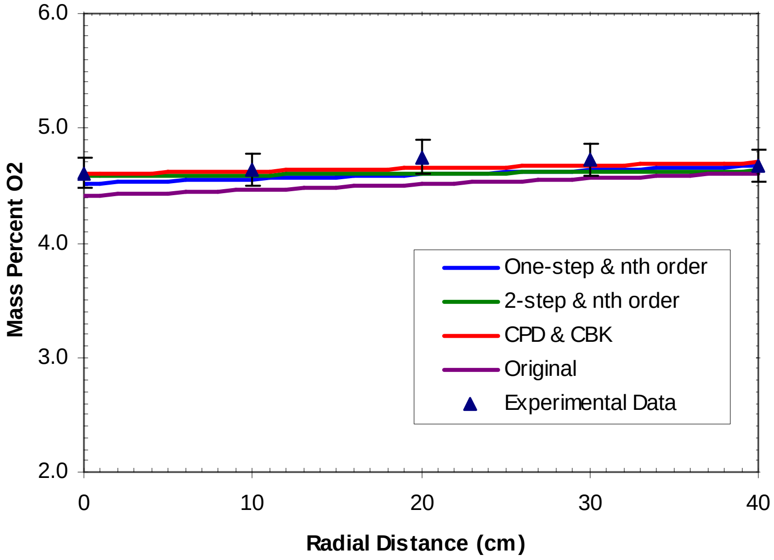

Figure 5-15. Predicted and measured radial O_2 concentrations at an axial distance of 150 cm.

5.3.2.4 Burnout Predictions

The original STAR-CD model predicted overall char burnout in the reactor of 97.8%. The one-step and two-step devolatilization-global nth-order char oxidation models predicted char burnout of 97.1% and 96.7%, respectively, while the CPD-CBK model predicted char burnout of 96.2%. All these predictions were in line with experimental data, which showed an average overall char burnout of 95.9% in the reactor. All models agreed with the experimental char burnout within 2% on a relative scale.

The centerline char burnout profile, shown in Figure 5-16, showed good agreement between model predictions and experimental data. All four CFD cases predicted similar burnout profiles and agreed within 5% of each other, and within 15% of all experimental data. It appears that the data point at 70 cm may be inaccurate. If this data point is neglected, predictions and data varied by less than 5%. The burnout profiles show devolatilization (0-20 cm) followed by char oxidation (20-150 cm).

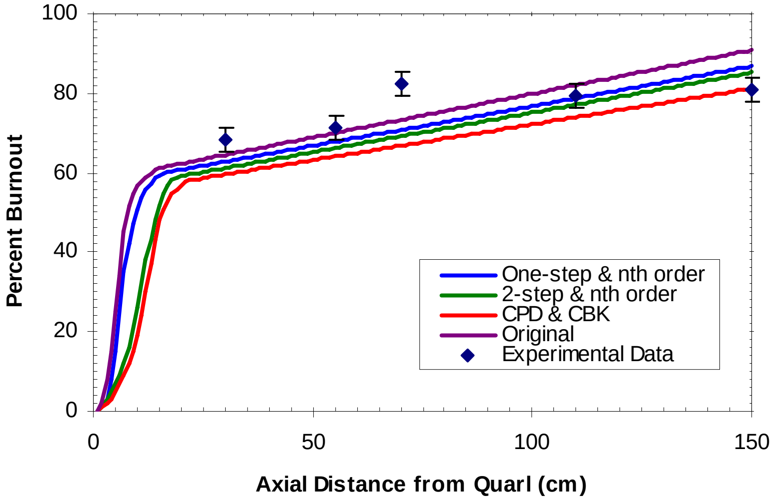

Figure 5-16. Predicted centerline burnout for the CPR.

Predicted radial burnout profiles at two axial distances (30 cm and 150 cm) were also compared with experimental data. The first axial location (30 cm), taken to correspond to a location within the flame front, is shown in Figure 5-17. The second axial location (150 cm) was taken downstream of the intense flame region, and is shown in Figure 5-18. All predicted burnout profiles were fairly similar, and showed good agreement with each other and with experimental data. The one-step and two-step-global nth order models were in the best agreement with each other, as expected because both models use the global nth-order char oxidation model.

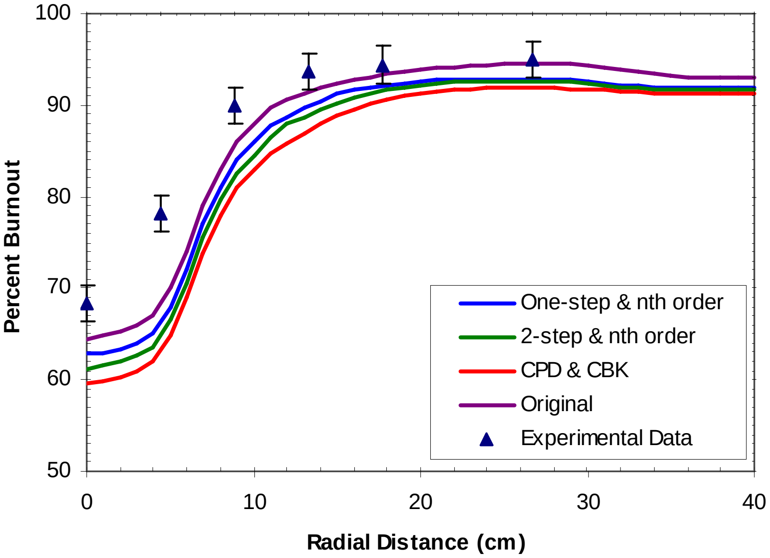

Figure 5-17. Predicted burnout at an axial distance of 30 cm.

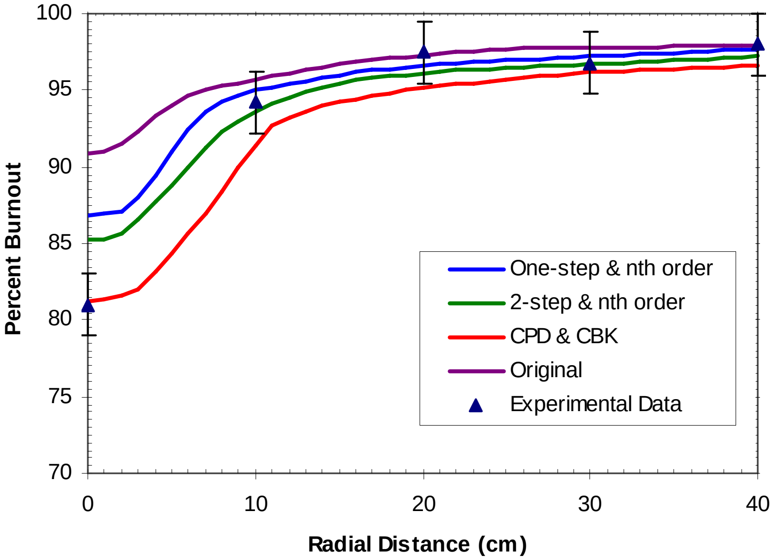

Figure 5-18. Predicted burnout at an axial distance of 150 cm.

5.3.3 Summary of Validation Case

All predicted results from all four cases were in good agreement (within 25%) with the experimental data. The three cases with the newly implemented coal submodels agreed more closely with each other, although there were some discrepancies between these modeling results and the experimental data. There were some instances where the predictions made using the original STAR-CD coal submodels agreed more closely with the experimental data, but, overall, the newly implemented submodels matched the experimental data better then the original STAR-CD submodels.

In addition, the CPD submodel provides additional parameters for tar and coal-nitrogen evolution that have not been implemented into STAR-CD. These parameters are important in calculating soot formation (tar evolution) and NO_x formation (coal-nitrogen release). If these parameters, calculated using the CPD submodel, are utilized in STAR-CD, they should improve the soot formation and NO_x formation submodels available in STAR-CD.

5.4 Conclusions

The implementation of the coal subroutines and submodels into STAR-CD was successful based on verification of the individual coal submodels and validation of the overall CFD code for modeling coal combustion. Both verification and validation predictions were in good agreement with experimental data. Predictions made using the updated submodels more closely agreed with experimental verification data than the original STAR-CD submodels. Improvement of between 25-40% was achieved (based on outlet temperatures and outlet species concentrations) using the PCGC-3 coal submodels versus the original STAR-CD coal submodels in modeling the BYU Controlled Profile Reactor. These verification and validation cases showed that the updated submodels increased STAR-CD's capability to accurately model coal-related systems. This improved accuracy will allow for better analysis and application of CFD for use in coal combustion and gasification, which will, in turn, enable the power generation industry to increase efficiency and reduce emissions in coal-fired commercial facilities through CFD modeling and analysis. This increased accuracy should also increase industry use of STAR-CD in other modeling applications.

6. Premixed Turbulent Combustion Modeling

The objective of this project was to compile the laboratory-scale gas turbine combustor data for modeling and distribution. The laboratory-scale gas turbine combustor (LSGTC) temperature data were originally taken by Hedman, et al. (2002a), with the LSGTC velocity data taken by Hedman, et al. (2002b), and the OH concentration data taken by Hedman, et al. (2002c). Because these data were taken by different researchers over the course of several years, they were originally located in several different places and formats.

6.1 Laser Doppler Anemometry (LDA) Velocity Data

The LDA velocity data consisted of axial, radial, and tangential velocity measurements at over 500 locations throughout the combustor. Typically, only two components of velocity (either axial-radial or axial-tangential) were available for each location in the combustor. The data were available in the following formats: 1) files that contained individual instantaneous velocity measurements at locations throughout the combustor; 2) files that contained statistical representations (means, standard deviations, and PDF's) of the instantaneous velocity data at locations throughout the combustor; and 3) files that had 2-D color plots of velocity measurements.

The first files were not included in the data compilation because they contained only the instantaneous velocity measurements at a specific location. The more useful information about each location was located in the second file type, which contained statistics derived from the instantaneous measurements. These files contained means, standard deviations, and probability density functions of axial, radial, and tangential velocity at each location. These files were reformatted into Microsoft Excel files, with one file for each case (4 total). The 2-D color plots were originally CANVAS drawings. These files were reformatted as Adobe PDF files so that they could be more accessible on the internet. A sample color profile from the data is found in Figure 6-1.

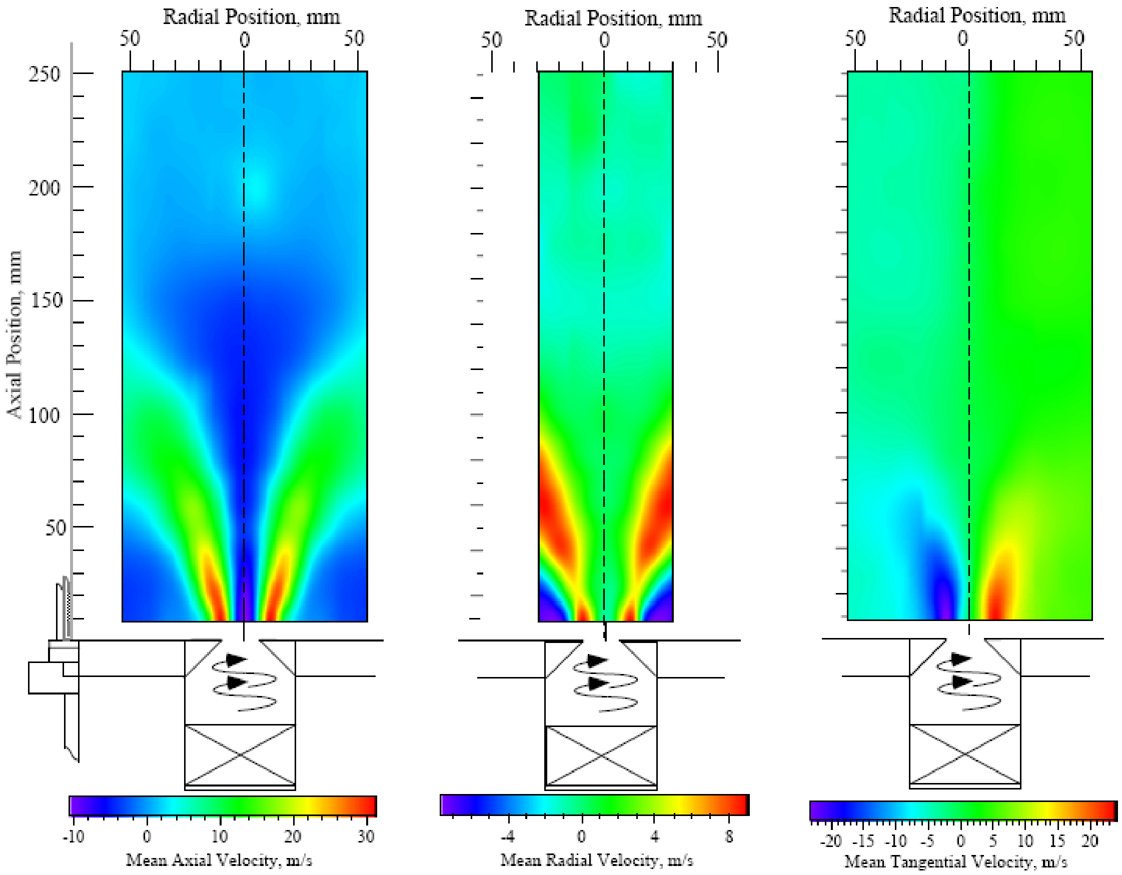

Figure 6-1. Profiles of mean axial, radial, and tangential velocity for the MS-0.65 Case.

6.2 Coherent Anti-Stokes Raman Spectroscopy (CARS) Temperature Data

The CARS temperature data consisted of temperature measurements at over 500 locations throughout the combustor. The data were available in the following formats: 1) files that contained individual instantaneous temperature measurements at locations throughout the combustor; 2) files that contained statistical representations (means, standard deviations, and probability density functions) of the instantaneous temperature data at locations throughout the combustor; 3) files that contained 1-D plots of mean temperatures in the axial and radial directions at various locations in the reactor; and 4) files that had 2-D color plots of temperature measurements.

The first files were not included in this compilation because these data were more concisely described in the second file type, which contained statistics (means, standard deviations) derived from the instantaneous measurements. The statistical files also contained probability density functions showing the distribution of instantaneous temperatures at each measurement location. The files that contained the statistics were combined into one MS-Excel file describing all four cases. The 1-D plots of mean axial and radial temperatures were reformatted as MS-Word documents, one for each case. The file showing the 2-D color plots of mean temperature for all cases was originally a CANVAS drawing. This drawing was reformatted as an Adobe PDF document to be more easily accessible and is shown in Figure 6-2. In addition, an Adobe PDF document also contains 2-D color plots of the standard deviation of temperature for all four cases.

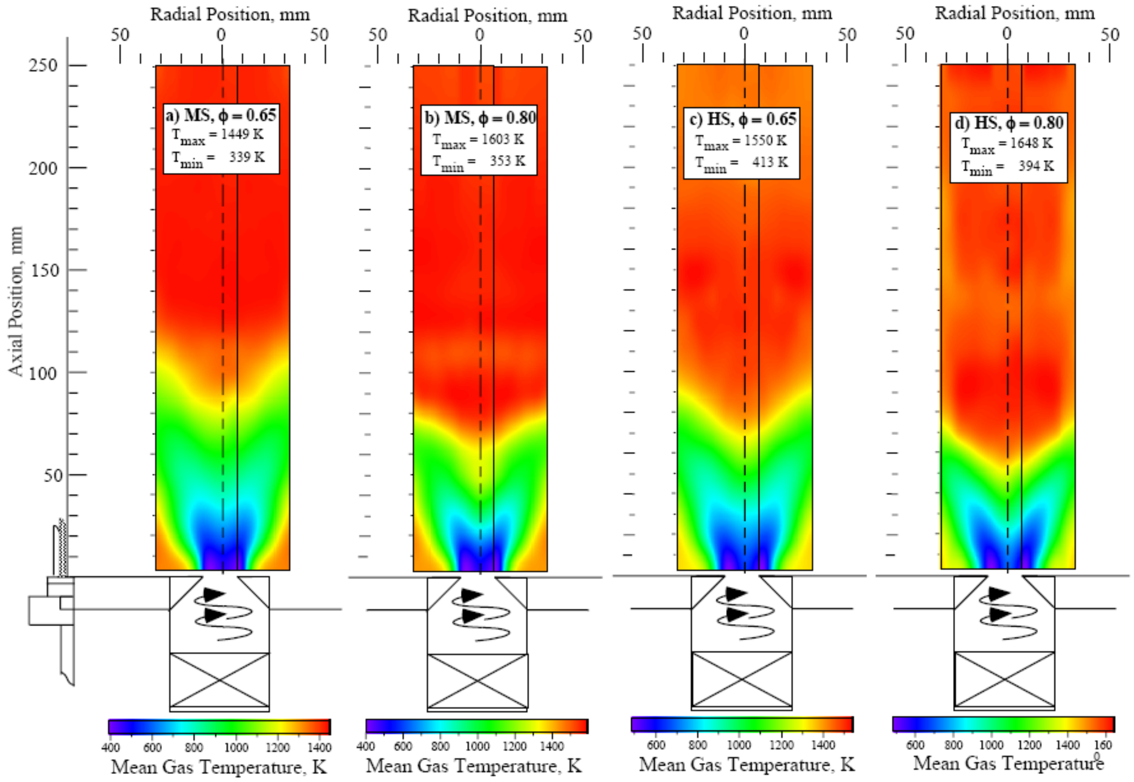

Figure 6-2. Mean temperature profiles for all four cases.

6.3 Planar Laser-Induced Fluorescence (PLIF) OH Species Concentration Data

The PLIF OH concentration data consisted of computer-generated false color images of instantaneous OH species concentrations over a 2-dimensional plane in the combustor. While the images provide instantaneous flame structure, they have not been accurately quantified. In other words, the images correspond to OH counts by the detector, and these counts have not been related to actual OH species concentrations, but are proportional to OH concentration. In addition, individual images can be somewhat misleading. For each image, the detector counts for each pixel were normalized to the peak detector count to create a false color image, with red scaled to the peak value and black scaled to the minimum value. The detector counts were normalized to the peak relative intensity for that image whether the value of the peak detector count was 400 or 4000.

These instantaneous images were originally CANVAS documents, but were converted to Adobe PDF format, with 16 images per document. Average and standard deviation profiles were also available for each case as CANVAS documents. These profiles were also converted to Adobe PDF documents, and one of these profiles is shown in Figure 6-3. In addition, probability density functions which show the distribution of instantaneous OH species concentrations at various points throughout the reactor were placed in Adobe PDF format.

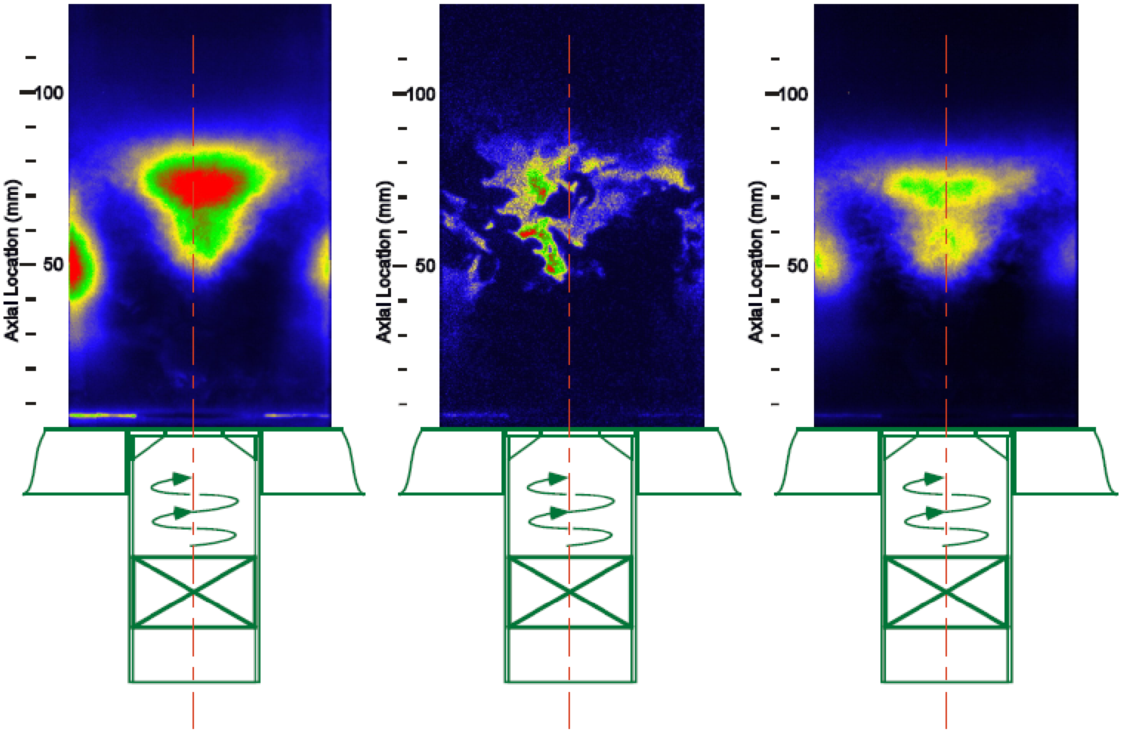

(a) Average of 256 Images (b) Example Instantaneous Image (c) Standard Deviation for 256 Images

Figure 6-3. Representative profiles of OH concentration using PLIF for the HS-0.65 case.

6.4 Data Summary

Table 6-1 describes all of the data that were compiled for this project. This table includes the data for all four operating conditions.

Table 6-1. Summary of the Data Compiled for the LSGTC.

Case	HS-0.65	HS-0.80	MS-0.65	MS-0.80
LDA Velocity Data				
Spreadsheet Data	X	X	X	X
2-D Color Plots (Average)	X	X	X	X
2-D Color Plots (Standard Deviation)		X	X	
CARS Temperature Data				
Spreadsheet Data	X	X	X	X
1-D Plots (Average)	X	X	X	X
2-D Color Plots (Avg. and StDev)	X	X	X	X
PLIF OH Concentration Data				
Spreadsheet Data	X	X	X	X
Instantaneous 2-D Color Plots	X	X	X	X
Average 2-D Color Plots	X	X	X	X
2-D Color Plots (Standard Deviation)		X		

6.5 Conclusions

The compiled LSGTC data provide the most complete data set available for turbulent, swirling, lean, premixed combustion. This data set was placed on the internet at http://www.et.byu.edu/~tom/gas_turbines/LSGTC_data_description.html. The data set also is included in the CD that accompanies this dissertation. Lean premixed combustion is important to understand and model, since it offers low pollutant emissions and increased efficiency for the gas turbine industry. These compiled data should serve as a benchmark to validate turbulent, premixed combustion modeling work. This modeling work is critical in the maturation of lean, premixed combustion technology.

7. Conclusions

This dissertation discussed several aspects of CFD modeling: code application, code development and improvement, and code evaluation. Computational fluid dynamics modeling was successfully used to predict the performance of two systems that involved flow, heat transfer, and chemical reactions. CFD results were analyzed to understand the performance of the studied equipment and to help in the design of new equipment.

7.1 Solar CO_2 Conversion Modeling Research

Solar CO_2 conversion involves using solar energy to drive the high-temperature dissociation of CO_2 into CO and O_2. Modeling was needed to understand the various phenomena (flow, heat transfer, reaction chemistry) occurring in the solar converter. Modeling was performed using three CFD codes: FLUENT, STAR-CD, and PCGC-3. The modeling work on the solar CO_2 converter was successful in predicting the performance of the original converter, matching both the experimental outlet CO mol% and outlet temperature. Modeling showed that all significant reactions occurred in a small thermal boundary layer directly around the zirconia rod, with the majority of the flow bypassing the highest temperatures in the converter.

CFD modeling also showed that the converter could be improved by several modifications, including increasing the zirconia rod diameter, decreasing the overall flow rate, decreasing the cool-down pipe diameter, changing the cool-down section, and increasing the operating pressure. Three of these modifications (decreasing overall flow rate, increasing zirconia rod diameter, and decreasing cool-down pipe diameter) have were made to the prototype and have resulted in increased CO conversion, as predicted by the modeling work. Modeling efforts helped improve CO conversion in the converter by over 50%. This work was done to improve converter performance to help make this process more economically viable. This process has the potential to provide renewable energy (H_2 or CO) and/or electricity without the production of additional greenhouse gases.

7.2 Improved Coal Combustion Modeling Using STAR-CD

PCGC-3, a CFD code developed at BYU for the purpose of modeling coal combustion and gasification, contains advanced coal combustion submodels. These submodels include a coal initialization model, a moisture vaporization model, three devolatilization models (one-step, two-step, CPD), and two char oxidation models (global nth-order, CBK). These submodels were implemented into STAR-CD, a commercial CFD code. The implementation of these coal submodels into STAR-CD improved its overall accuracy in modeling coal combustion systems, as shown by comparison of predictions to validation data. Predictions made using the implemented PCGC-3 coal submodels agreed more closely (between 25-40%) with experimental data than predictions made using the original STAR-CD coal submodels.

Accurate coal combustion and gasification modeling using STAR-CD will enable better analysis of coal-fired commercial facilities, which should lead to increased efficiency and reduced emissions in these facilities. The increased accuracy of the coal combustion and gasification models should also increase use of STAR-CD in other modeling applications.

7.3 Premixed Turbulent Combustion Data Compilation

Lean premixed combustion offers lower pollutant emissions and increased efficiency versus traditional natural gas combustion techniques. Lean premixed combustion data have previously been taken in a laboratory-scale gas turbine combustor at BYU using advanced laser diagnostics, and reported elsewhere in unusable formats. These data consist of velocity, temperature, and OH species concentration measurements throughout the combustor. These data were gathered and compiled into a central location for easy access and use by both modelers (to validate code predictions) and experimentalists (to establish a basis for subsequent work). This data set provides the most complete data set available for turbulent, swirling, lean, premixed combustion. These compiled data can now serve as a benchmark to validate turbulent, premixed combustion modeling work.

8. References

Anthony, D. B., J. B. Howard, H. C. Hottel, and H. P. Meissner, "Rapid Devolatilization of Pulverized Coal," *Fifteenth Symposium (International) on Combustion*, The Combustion Institute, Pittsburgh, PA, 1303-1317 (1975).

Asay, B. W., L. D. Smoot, and P. O. Hedman, "Effects of Coal Type and Moisture Content on Burnout and Nitrogenous Pollutant Formation," *Combustion Science and Technology*, **35**, 15-31 (1983).

Bernard, P. S., and J. M. Wallace, Turbulent Flow: Analysis, Measurement, and Prediction, John Wiley & Sons, Hoboken, NJ, (2002).

Bird, R. B., W. E. Stewart, and E. N. Lightfoot, Transport Phenomena, John Wiley & Sons, New York, NY (2002).

Boysan, F., W. H. Ayers, J. Swithenbank, and Z. Pan, "Three-Dimensional Model of Spray Combustion in Gas Turbine Combustors," AIAA Paper, St. Louis, MO, 1-7 (1981).

Brown, A. L. and T. H. Fletcher, "Modeling Soot Derived from Pulverized Coal," *Energy and Fuels*, **12**, 745-757 (1998).

Cannon, J. N., B. W. Webb, and M. Queiroz, "Validation of 3-D Combustion Model (Results of Goudey Station Boiler Testing 1989 and 1991)," Final Report, ESEERCO Project No. EP 89-09, Brigham Young University, Provo, Utah (1993).

Cannon, S. M., B. S. Brewster, and L. D. Smoot, "PDF Modeling of Lean Premixed Combustion Using In Situ Tabulated Chemistry," *Combustion and Flame*, **119**, 233-252 (1999).

Carvalho, M. G., T. Farias, and P. Fontes, "Predicting Radiative Heat Transfer in Absorbing, Emitting, and Scattering Media Using the Discrete Transfer Method," *Fundamentals of Radiation Heat Transfer*, ASME Heat Transfer Division, **160**, 17-26 (1991).

Cheng, P., “Two-dimensional Radiating Gas Flow by a Moment Method,” *AIAA Journal,* **2**, 1662-1664 (1964).

Chigier, N.A., Combustion Measurements, Hemisphere, New York, NY, (1991).

Cotronics Corporation, Properties of Refractory, Ceramics, and Intermetallic Materials, New York, NY, (1995).

Eckbreth, A.C., Laser Diagnostics for Combustion Temperature and Species Measurements, Gordon and Breach, Amsterdam, The Netherlands, (1996).

Fletcher, T. H., A. R. Kerstein, R. J. Pugmire, and D. M. Grant, “Chemical Percolation Model for Devolatilization. 2. Temperature and Heating Rate Effects on Product Yields,” *Energy and Fuels*, **4**, 54-60 (1990).

Fletcher, T. H., A. R. Kerstein, R. J. Pugmire, M. S. Solum, and D. M. Grant, “Chemical Percolation Model for Devolatilization. 3. Direct Use of ^{13}C NMR Data to Predict Effects of Coal Type,” *Energy and Fuels*, **6**, 414-431 (1992).

Fletcher, T. H., J. Ma, J. R. Rigby, A. L. Brown, and B. W. Webb, “Soot in Coal Combustion Systems,” *Progress in Energy and Combustion Science*, **23**, 283-301 (1997).

Flores, D. V., “Analysis of Lean Premixed Turbulent Combustion using Coherent Anti-Stokes Raman Spectroscopy Temperature Measurements,” Ph. D. Dissertation, Department of Chemical Engineering, Brigham Young University, Provo (2003).

Flores, D. V. and T. F. Fletcher, “The Use of Two Mixture Fractions to Treat Coal Combustion Products in Turbulent Pulverized-Coal Flames,” *Combustion Science and Technology*, **150**, 1-26 (2000).

FLUENT User’s Guide, FLUENT, Inc. Lebanon, NH, 2007.

Foster, P. J., “Continuous CO Separation by Liquid Absorption in Aqueous Cuprous Chloride (CuCl) and Magnesium Chloride ($MgCl_2$) Solution”, M.S. Thesis, Department of Chemical Engineering, Brigham Young University, Provo (2006).

Gibbins-Matham, J. and R. Kandiyoti, “Coal Pyrolysis Yields from Fast and Slow Heating in a Wire-Mesh Apparatus with a Gas Sweep,” *Energy & Fuels,* **2**, 505-511 (1988).

Goetz, G. J., N. Y. Nsakala, R. L. Patel, and G. H. Quentin, “Combustion and Gasification Kinetics of Chars from Four Commercially Significant Coals of Varying Rank,” 1983 International Conference on Coal Science, Pittsburgh, PA, 571-574 (1983).

Gordon, S. and B. J. McBride, "Computer Program for Computation of Complex Chemical Equilibrium Compositions, Rocket Performance, Incident and Reflected Shocks, and Chapman-Jouguet Detonations," NASA report SP-273, (1971).

Gosman, A.D., "Developments in Industrial Computational Fluid Dynamics," *Chemical Engineering Research and Design*, **76**, 153-161 (1998).

Grant, D. M., R. J. Pugmire, T. H. Fletcher, and A. R. Kerstein, "A Chemical Model of Coal Devolatilization Using Percolation Lattice Statistics," *Energy and Fuels*, **3**, 175-186 (1989).

Haslam, J. K., and P. O. Hedman, "The Use of Two Pyromethene Dyes in a Single Stokes Dye Laser to Make CARS Temperature and Multiple Species (CO, CO_2, O_2, N_2) Concentration Measurements," Fall Meeting of WSS/CI, 96F-086, Los Angeles, CA (1996).

Hedman, P. O., T. H. Fletcher, S. G. Graham, G. W. Timothy, D. V. Flores, and J. K. Haslam, "Observations of Flame Behavior in a Laboratory-Scale Pre-Mixed Natural Gas/Air Gas Turbine Combustor from PLIF Measurements of OH," paper GT-2002-20052, ASME Turbo Expo Meeting, Amsterdam, The Netherlands, (June 3-6, 2002).

Hedman, P. O., D. V. Flores, and T. H. Fletcher, "Observations of Flame Behavior in a Laboratory-Scale Pre-Mixed Natural Gas/Air Gas Turbine Combustor from CARS Temperature Measurements," paper GT-2002-20054, ASME Turbo Expo Meeting, Amsterdam, The Netherlands, (June 3-6, 2002).

Hedman, P. O., R. L. Murray, and T. H. Fletcher, "Observations of Flame Behavior in a Laboratory-Scale Pre-Mixed Natural Gas/Air Gas Turbine Combustor from LDA Velocity Measurements," paper GT-2002-20053, ASME Turbo Expo Meeting, Amsterdam, The Netherlands, (June 3-6, 2002).

Hedman, P. O., T. H. Fletcher, D. V. Flores, S. G. Graham, J. K. Haslam, R. L. Murray, G. W. Timothy, "Observations of Flame Behavior in a Laboratory-Scale Pre-Mixed Natural Gas/Air Gas Turbine Combustor from PLIF Measurements of OH, LDA Velocity measurements, and CARS Temperature Measurements," *ASME Journal for Gas Turbines and Power*, **127:4**, 724-739 (2005).

Hedman, P.O., Personal Communication, July 22, 2006.

Hill. S. C. and L. D. Smoot, "A Comprehensive Three-Dimensional Model for Simulation of Combustion Systems: PCGC-3," *Energy & Fuels*, **7**, 874-883 (1993).

Hill, S. C. and L. D. Smoot, "Modeling of Nitrogen Oxides Formation and Destruction in Combustion Systems," *Progress in Energy and Combustion Science*, **26**, 417-458 (2000).

Hurt, R., J. K. Sun, and M. Lunden, "A Kinetic Model of Carbon Burnout in Pulverized Coal Combustion," *Combustion and Flame*, **113**, 181-197 (1998).

Incropera, F. P. and D. P. DeWitt, Fundamentals of Heat and Mass Transfer, John Wiley & Sons, New York, NY (1996).

JANAF Thermochemical Tables, Dow Chemical Company, Midland, MI (1998).

Jensen, R. J., R. D. Guetter, and J. L. Lyman, "The Ultraviolet Absorption of Hot Carbon Dioxide," *Chemical Physics Letters*, **277**, 356-360 (1997).

Jensen, R.J., Personal Communication, September 12, 2005.

Kee, R. J., J. F. Grcar, M. D. Smooke, and J. A. Miller, "A Fortran Program for Modeling Steady Laminar One-Dimensional Premixed Flames," Sandia National Laboratories report UC-401, (1992).

Kee, R. J., F. M. Rupley, E. Meeks, and J. A. Miller, "CHEMKIN-111: A Fortran Chemical Kinetics Package for the Analysis of Gas-Phase Chemical and Plasma Kinetics," Sandia National Laboratories report UC-405, (1996).

Kobayashi, H., J. B. Howard, and A. F. Sarofim, "Coal Devolatilization at High Temperature," *Sixteenth Symposium (International) on Combustion*, The Combustion Institute, Pittsburgh, PA, 411-425 (1976).

Kodama, T., "High-temperature Solar Chemistry for Converting Solar Heat to Chemical Fuels," *Progress in Energy and Combustion Sciences*, **29**, 567-597 (2003).

Kohse-Höinghaus, K. and J.B. Jeffries, Applied Combustion Diagnostics, Taylor and Francis, New York, NY, 2002.

Kumar, S., A. Majumdar, and C. L. Tien, "The Differential-Discrete-Ordinate Method for Solutions of the Equation of Radiative Transfer," *Journal of Heat Transfer*, **112**, 424-429 (1990).

Launder, B. E., G. J. Reece, and W. Rodi, "Progress in the Development of a Reynolds-Stress Turbulence Closure," *Journal of Fluid Mechanics*, **68**, 537-566 (1975).

Launder, B. E., and D. B. Spalding, Lectures in Mathematical Models of Turbulence, Academic Press, London, England, (1972).

Leonard, B. P. and S. Mokhtari. "ULTRA-SHARP Nonoscillatory Convection Schemes for High-Speed Steady Multidimensional Flow," NASA TM 1-2568 (ICOMP-90-12), NASA Lewis Research Center, (1990).

Libby, P. A. and F. A. Williams, Turbulent Reacting Flows, Springer-Verlag, Berlin, Germany, (1980).

Lyman, J. L. and R. J. Jensen, "Chemical Reactions Occurring During Direct Solar Reduction of CO_2," *The Science of the Total Environment*, **277**, 7-14 (2001).

Magnussen, B. F., and B. H. Hjertager, "On Mathematical Models of Turbulent Combustion with Special Emphasis on Soot Formation and Combustion," *Sixteenth Symposium (International) on Combustion*, The Combustion Institute, Cambridge, MA, 719-729 (1976).

Murray, R. L., "Laser Doppler Anemometry Measurements in a Turbulent, Premixed, Natural Gas/Air Combustor," M. S. Thesis, Department of Chemical Engineering, Brigham Young University, Provo (1998).

Nichols, K. M., P. O. Hedman, and L. D. Smoot, "Release and Reaction of Fuel-Nitrogen in a High-Pressure Entrained-Coal Gasifier," *Fuel*, **66**, 1257-1263 (1987).

Patankar, S. V., Numerical Heat Transfer and Fluid Flow, McGraw Hill, Boston, MA, (1980).

Pope, S. B., "PDF Methods for Turbulent Reactive Flows," *Progress in Energy and Combustion Science*, **11**, 119-192 (1985).

Pope, S. B., "Computationally Efficient Implementation of Combustion Chemistry Using In Situ Adaptive Tabulation," *Combustion Theory and Modeling*, **1**, 41–63 (1997).

Price, R. J., D. A. Morse, S. Hardy, T. H. Fletcher, S. Hill, and R. J. Jensen, "Modeling the Direct Solar Conversion of CO_2 to CO and O_2," *Industrial and Engineering Chemistry Research*, **43**, 2446-2453 (2004).

Rachford, H. H. Jr. and J. D. Rice, "Procedure for Use of Electronic Digital Computers in Calculating Flash Vaporization Hydrocarbon Equilibrium," *Journal of Petroleum Technology*, **4**, 10-19 (1952).

Raithby, G. D. and E. H. Chui, "A Finite-Volume Method for Predicting a Radiant Heat Transfer in Enclosures with Participating Media," *Journal of Heat Transfer*, **112**, 415-423 (1990).

Sanderson, D. K. and G. J. Germane, "Comparison of Combustion Gased and Particles in a Pulverized Coal-Fired Reactor," *Energy and Fuels*, **7**, 910-918 (1993).

Sandler, S. I., Chemical and Engineering Thermodynamics, John Wiley & Sons, New York, NY (1999).

Siegel, R. and J. R. Howell, Thermal Radiation Heat Transfer, Taylor & Francis, New York, NY, (2002).

Sloan, D. G., P. J. Smith, and L. D. Smoot, "Modeling of Swirl in Turbulent Flow Systems," *Progress in Energy and Combustion Science*, **12**, 163-250 (1986).

Smith, K. L., L. D. Smoot, T. H. Fletcher and R. J. Pugmire, The Structure and Processes of Coal, Plenum Press, New York, NY, (1994).

Solomon, P. R., M. A. Serio, R. M. Carangelo, J. R. Markham, "Very Rapid Coal Pyrolysis," *Fuel*, **65**, 182-194 (1986).

Spalart, P. R., and S. R. Allmaras, "A One-Equation Turbulence Model for Aerodynamic Flows," *Recherche Aerospatiale*, **1**, 5-21 (1994).

Sturgess, G. J., D. G. Sloan, A. L. Lesmerises, S. P. Heneghan, S.P. and D. R. Ballal, "Design and Development of a Research Combustor for Lean Blow-out Studies," *Journal of Engineering for Gas Turbines and Power, Transactions of the ASME*, **114**, 13-19 (1992).

Thornock, D. E., and R. W. Borion, "Developing a Coal Quality Expert: Combustion and Fireside Performance Characterization Factors," Report prepared for CQ INC. and US Department of Energy, ABB Combustion Engineering (1992).

Thornock, D. E., P. J. Grandia, and B. F. Griffith, "Combustion Modeling: A Combustion Data Set Taken in the Pilot-Scale Fireside Performance Test Facility," Report prepared for ABB Power Plant Laboratories (1993).

Traynor, A. J. and R. J. Jensen, "Direct Solar Reduction of CO_2 to Fuel: First Prototype Results," *Industrial and Engineering Chemistry Research*, **41**, 1935-1939 (2002).

Tree, D. R., D. L. Black, J. R. Rigby, M. Q. McQuay, and B. W. Webb, "Experimental Measurements in the BYU Controlled Profile Reactor," *Progress in Energy and Combustion Science*, **24**, 355-383 (1998).

Tsang, W. and R. F. Hampson, "Chemical Kinetic Data Base for Combustion Chemistry. Part I. Methane and Related Compounds," *Journal of Physical Chemistry Reference Data*, **15**, 1087-1145 (1986).

Turns, S. R., An Introduction to Combustion: Concepts and Applications, McGraw-Hill, Boston, MA, (2000).

Ubhayakar, S. K., D. B. Stickler, and R. E. Gannon, "Modeling of Entrained-Bed Pulverized Coal Gasifiers," *Fuel*, **56**, 281-291 (1977).

Wang, H. and J. N. Harb, "Modeling of Ash Deposition in Large-Scale Combustion Facilities Burning Pulverized Coal," *Progress in Energy and Combustion Science*, **23**, 267-282 (1997).

Wang, H., J. West, and J. N. Harb, "Microanalytical Characterization of Slagging Deposits from a Pilot-Scale Combustor," *Energy and Fuels*, **13**, 570-578 (1999).

Wilcox, D. C., Turbulence Modeling for CFD, DCW Industries, La Canada, CA, (1998).

Yetter, R. A., F. L. Dryer, M. T. Allen, and J. L. Gatto, "Development of Gas-Phase Reaction Mechanisms for Nitramine Combustion," *Journal of Propulsion and Power*, **11**, 683-697 (1995).

Zimont, V., W. Polifke, M. Bettelini, and W. Weinenstein, "An Efficient Computational Model for Premixed Turbulent Combustion at High Reynolds Numbers Based on Turbulent Flame Speed Closure." paper GT-1997-395, ASME Turbo Expo Meeting, Orlando, FL, (June 2-5, 1997).

Appendix A. Solar CO_2 Figures

This appendix contains important figures from the solar CO_2 converter modeling studies. These figures show the grid used for modeling the original prototype, along with velocity, temperature and CO concentration profiles for all of the cases not shown in the text of this dissertation. Some velocity profiles have been excluded because they are nearly identical to ones for other cases, varying only in the relative maximum velocity.

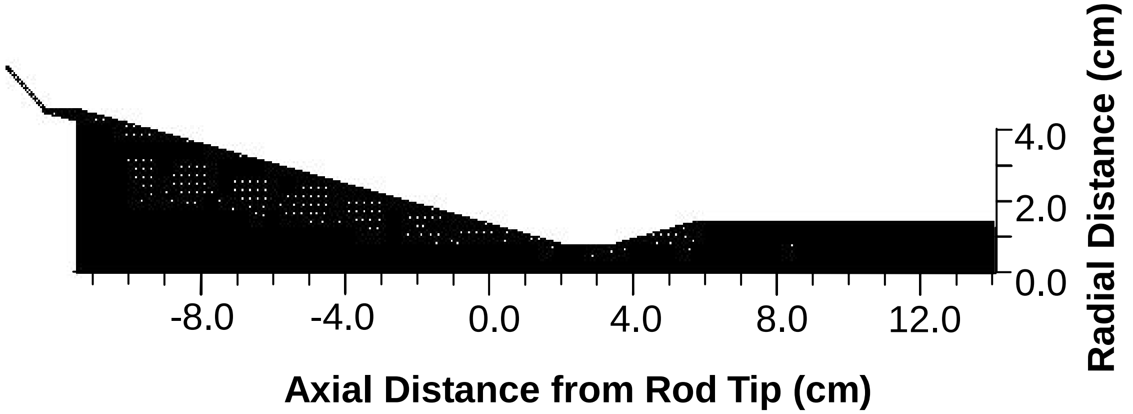

Figure A-1. Mesh used in modeling the solar converter prototype.

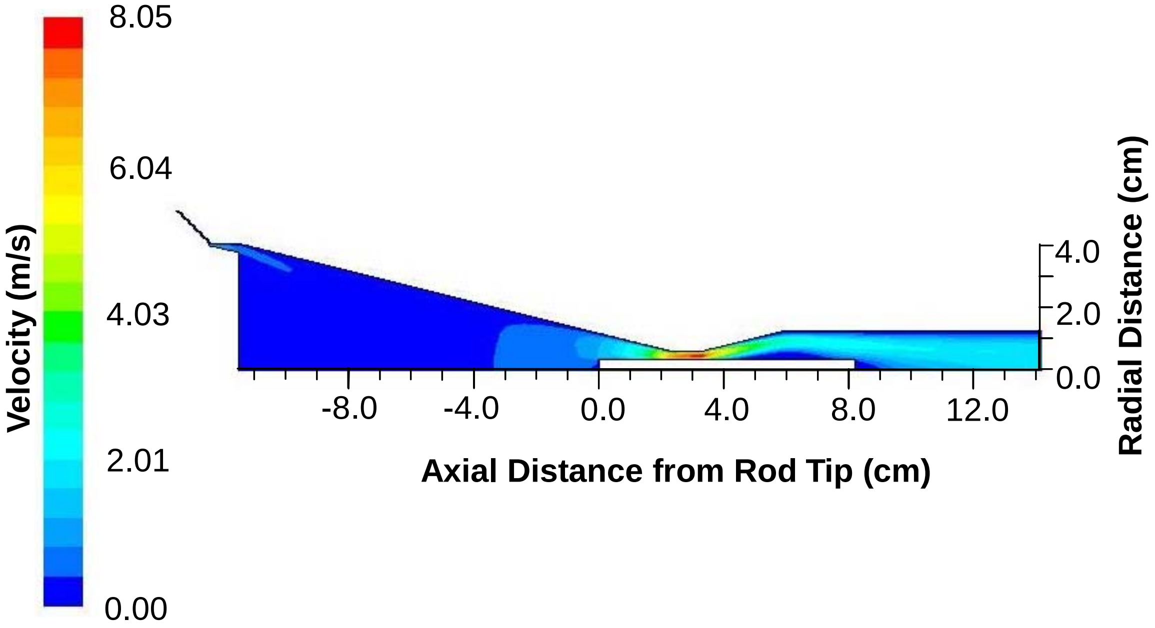

Figure A-2. Predicted velocity profile for the non-reacting case.

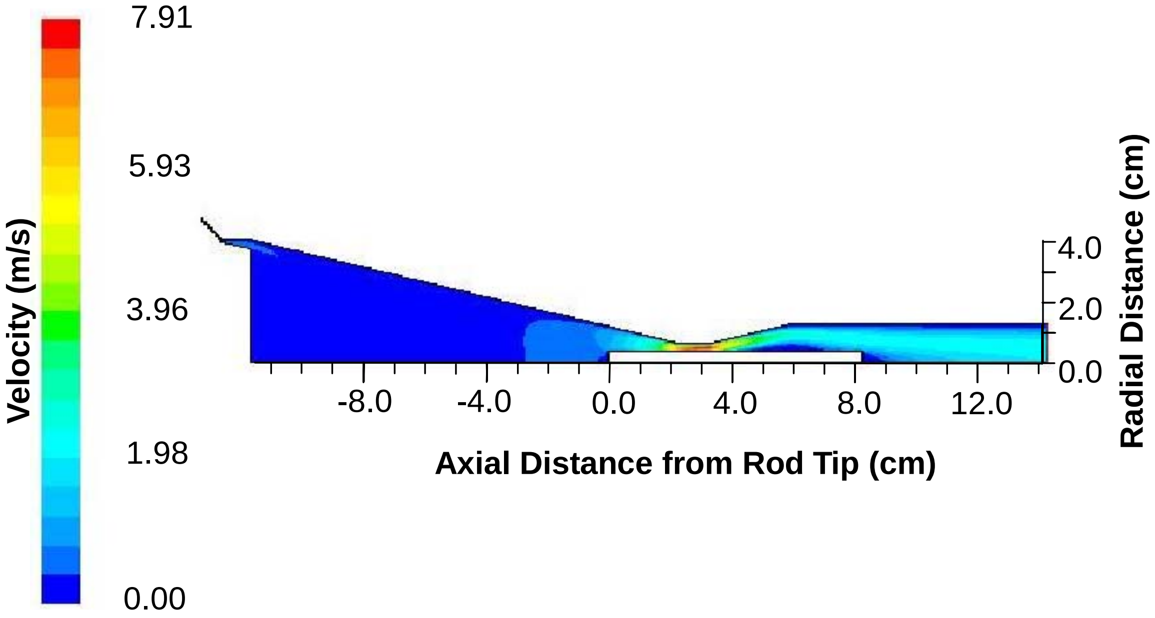

Figure A-3. Predicted velocity profile for the 4.0 kW radiation case.

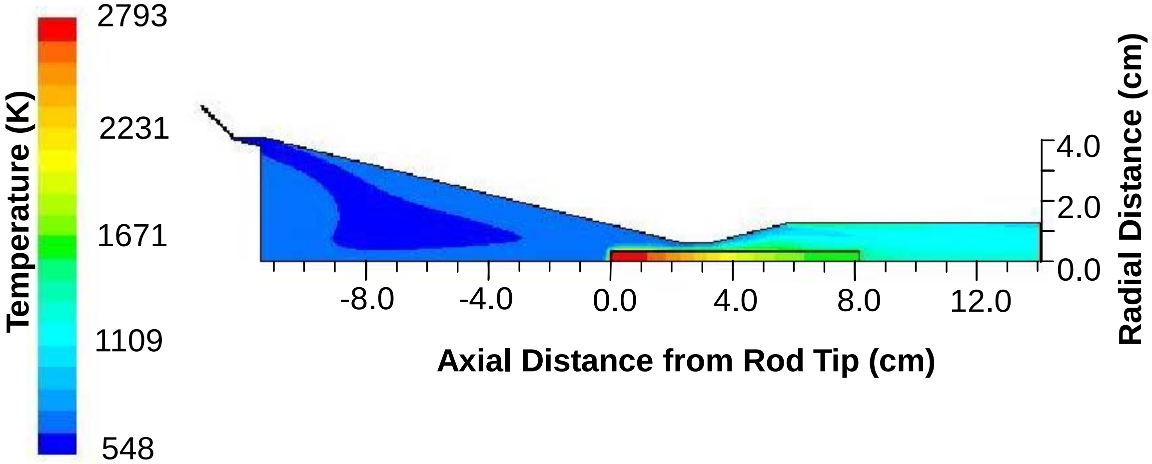

Figure A-4. Predicted temperature profile for the 5.0 kW case.

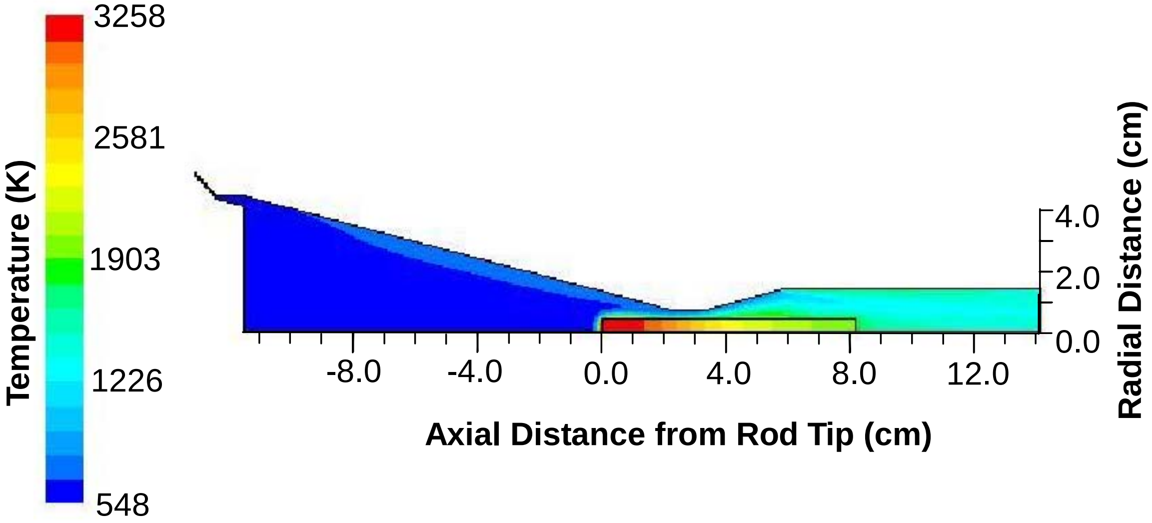

Figure A-5. Predicted temperature profile for the 7.2 kW case.

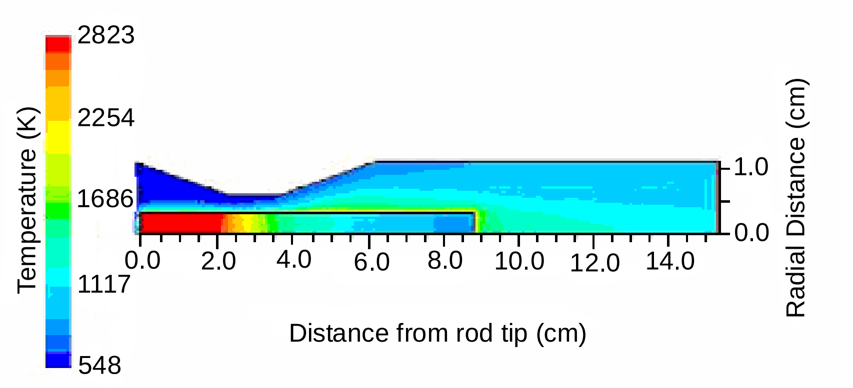

Figure A-6. **Predicted temperature profile for the high-temperature parametric case (Case 1).**

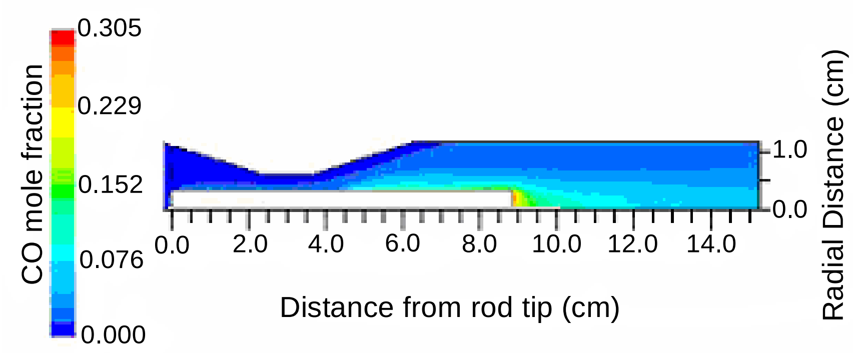

Figure A-7. **Predicted CO mole fraction profile for the high-temperature parametric case (Case 1).**

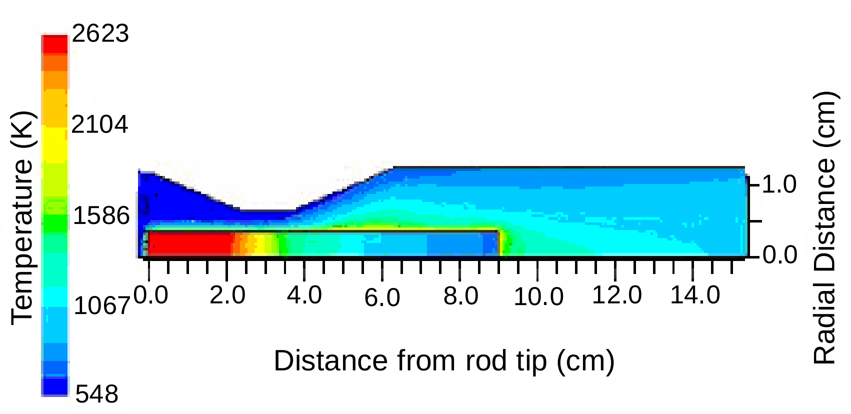

Figure A-8. Predicted temperature for the high-flow parametric case (Case 2).

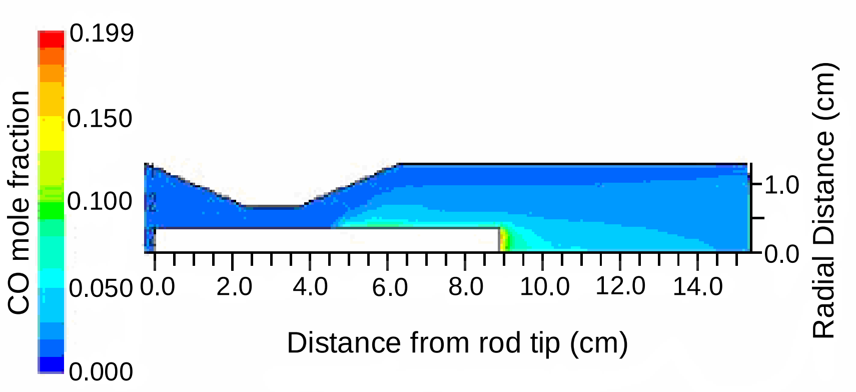

Figure A-9. Predicted CO mole fraction profile for the high-flow parametric case (Case 2).

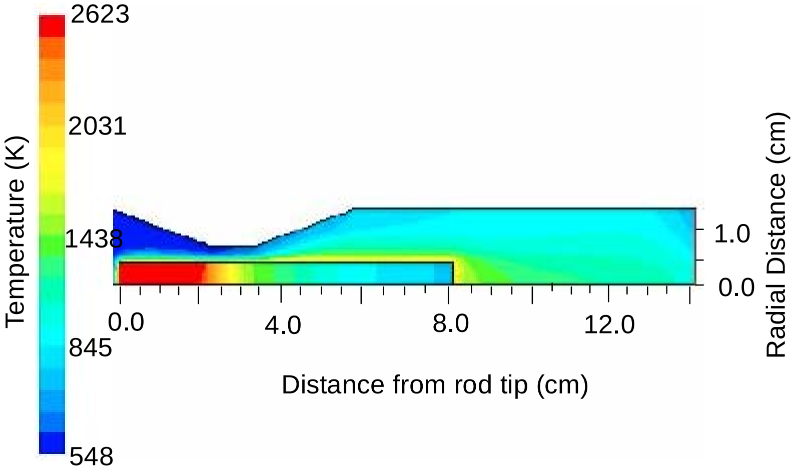

Figure A-10. Predicted temperature profile for the low-flow parametric case (Case 3).

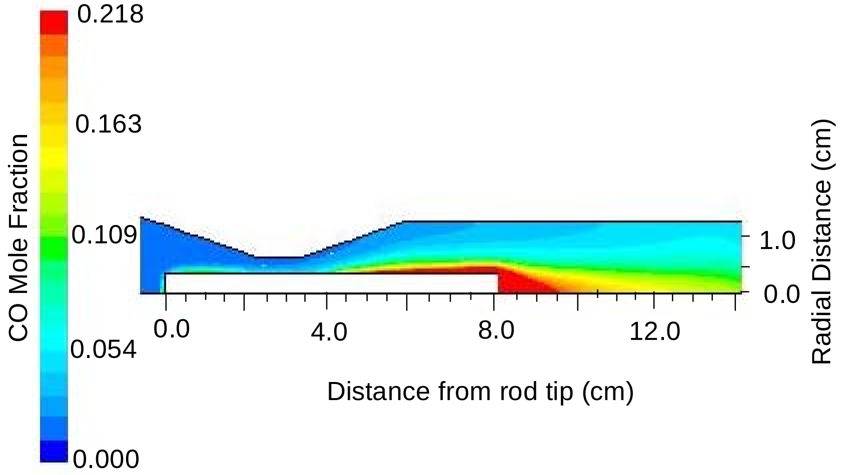

Figure A-11. Predicted CO mole fraction profile for the low-flow parametric case (Case 3).

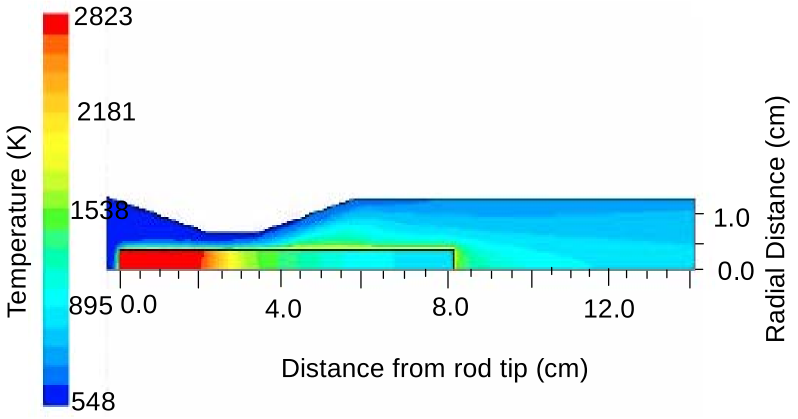

Figure A-12. Predicted temperature profile for the high-temperature/high-flow parametric case (Case 4).

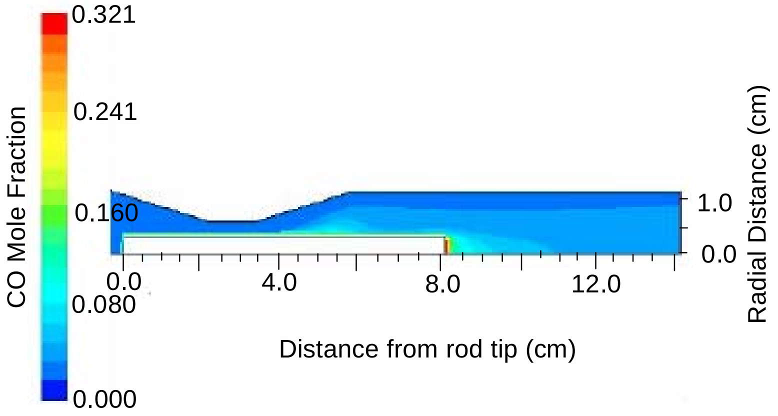

Figure A-13. Predicted CO mole fraction profile for the high-temperature/high-flow parametric case (Case 4).

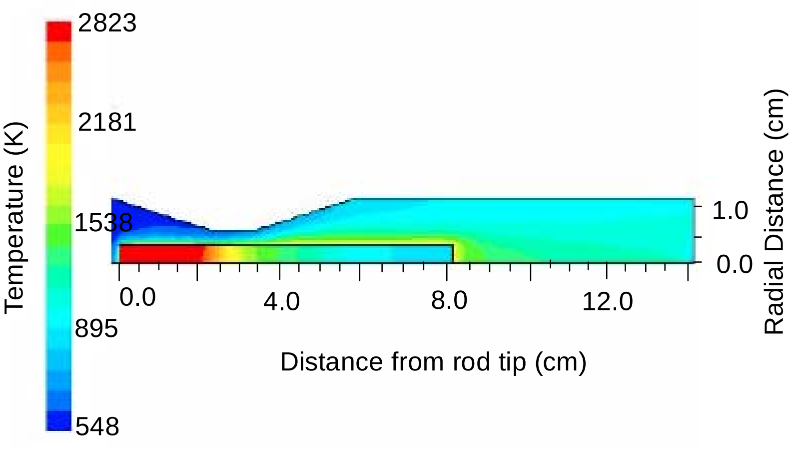

Figure A-14. **Predicted temperature profile for the high-temperature/low-flow parametric case (Case 5).**

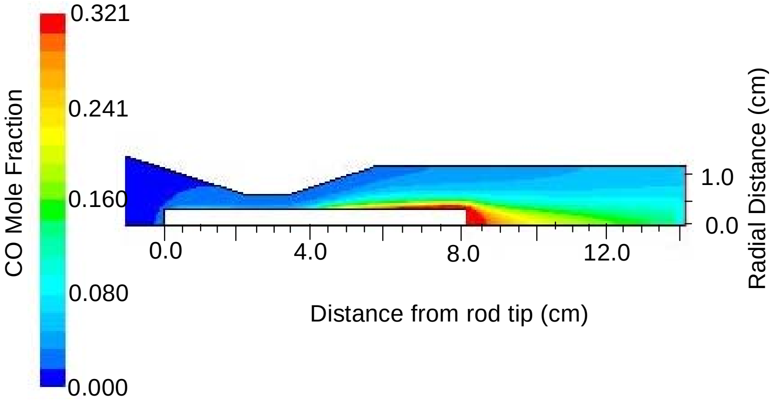

Figure A-15. **Predicted CO mole fraction profile for the high-temperature/low-flow parametric case (Case 5).**

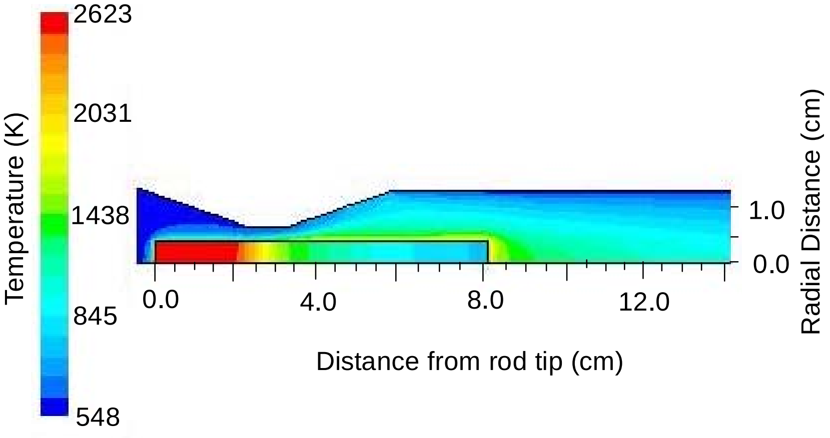

Figure A-16. Predicted temperature profile for the 6 slpm case (Case 6).

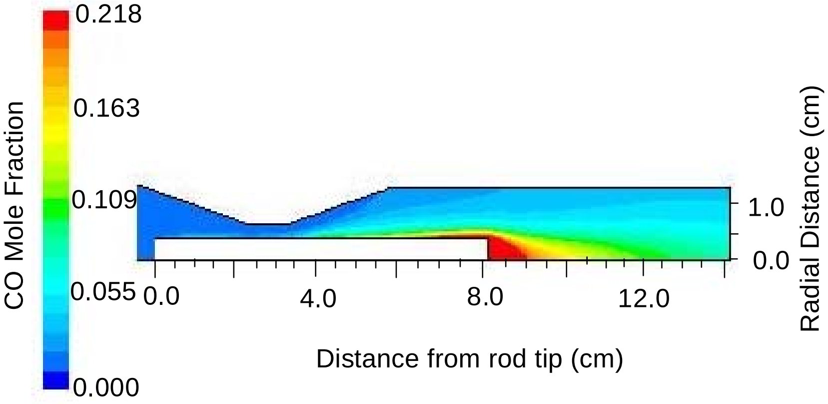

Figure A-17. Predicted CO mole fraction profile for the 6 slpm case (Case 6).

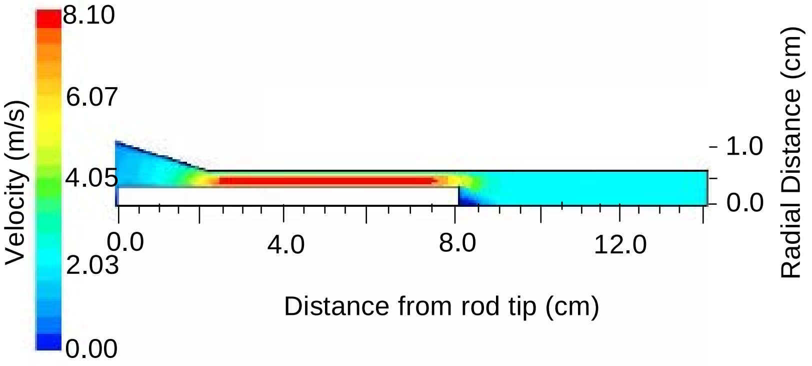

Figure A-18. Predicted velocity profile for the no post-throat expansion case (Case 7).

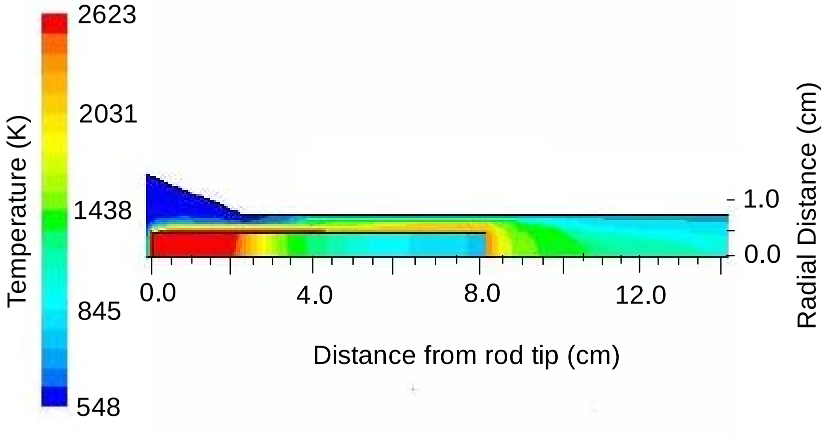

Figure A-19. Predicted temperature profile for the no post-throat expansion case (Case 7).

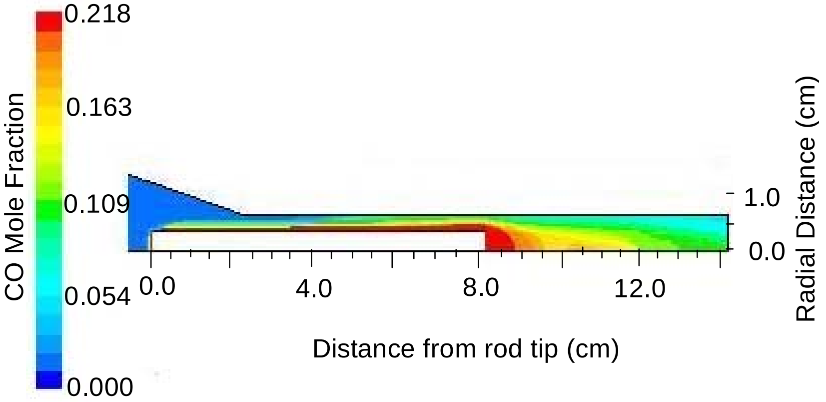

Figure A-20. **Predicted CO mole fraction profile for the no post-throat expansion case (Case 7).**

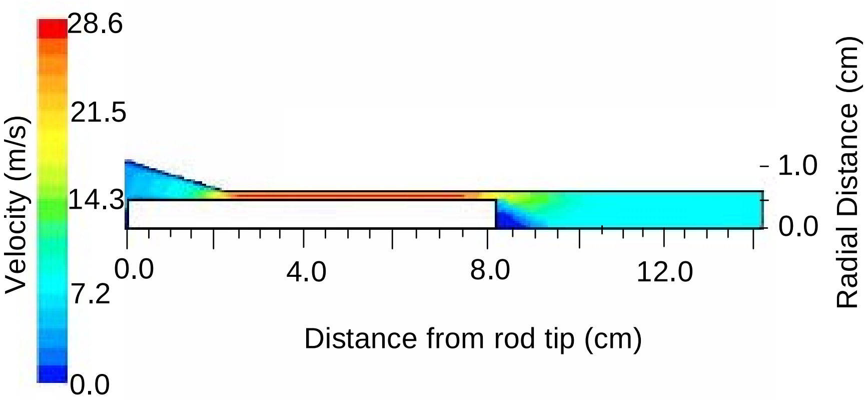

Figure A-21. Predicted velocity for the larger-diameter rod case (Case 8).

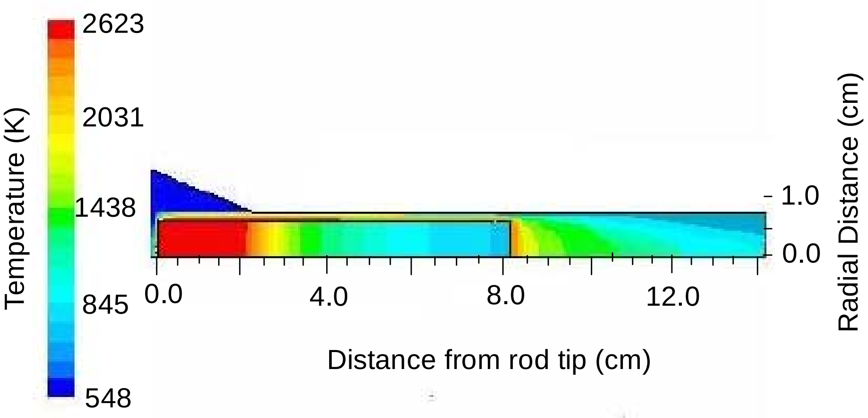

Figure A-22. Predicted temperature profile for the larger-diameter rod case (Case 8).

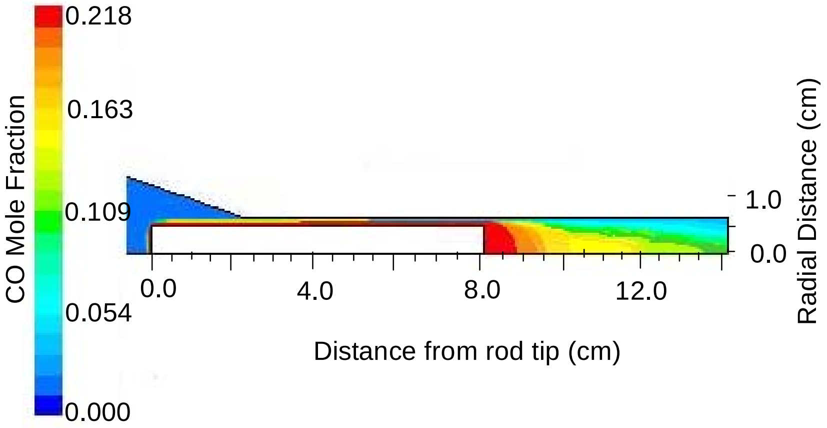

Figure A-23. Predicted CO mole fraction profile for the larger-diameter rod case (Case 8).

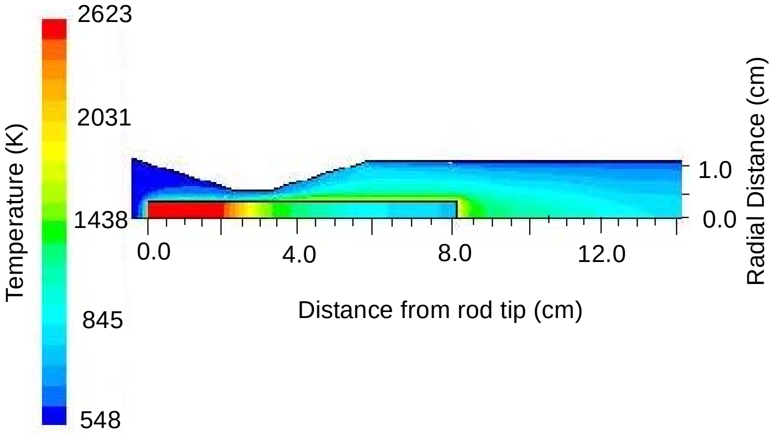

Figure A-24. Predicted temperature profile for the 2 atm-6 slpm case (Case 9).

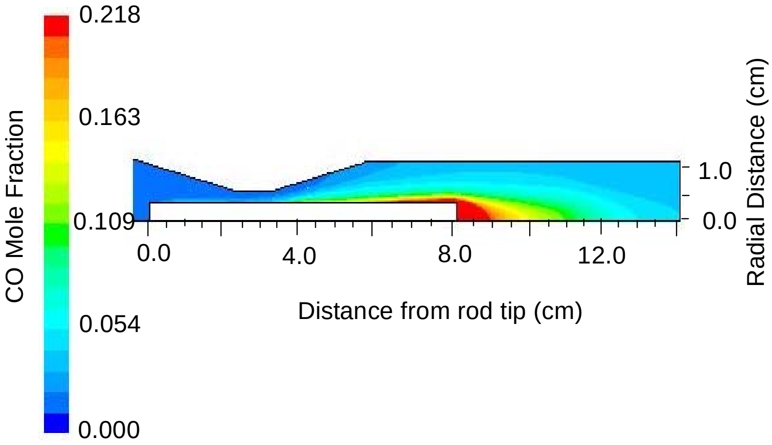

Figure A-25. Predicted CO mole fraction profile for the 2 atm-6 slpm case (Case 9).

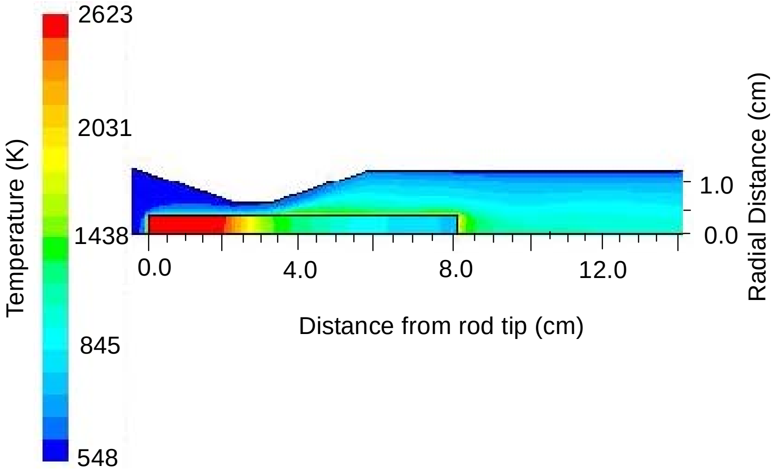

Figure A-26. Predicted temperature profile for the 2 atm-12 splm case (Case 10).

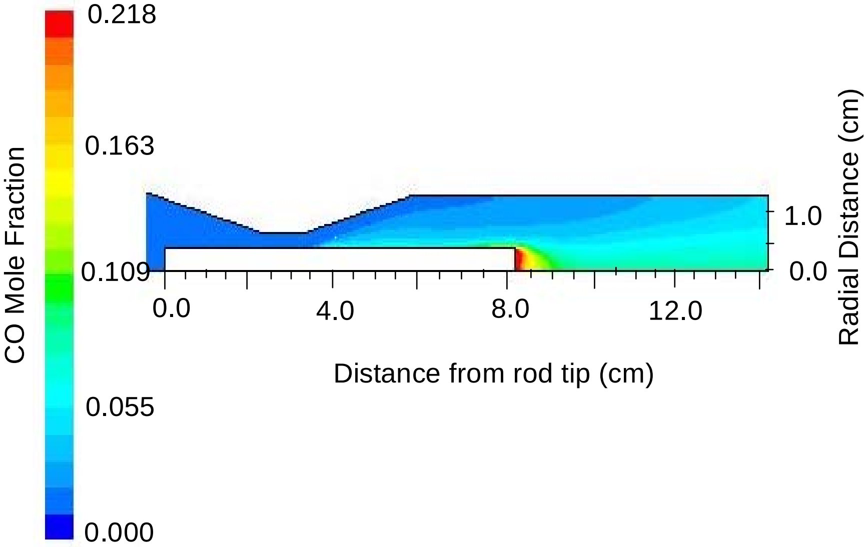

Figure A-27. Predicted CO mole fraction profile for the 2 atm-12 splm case (Case 10).

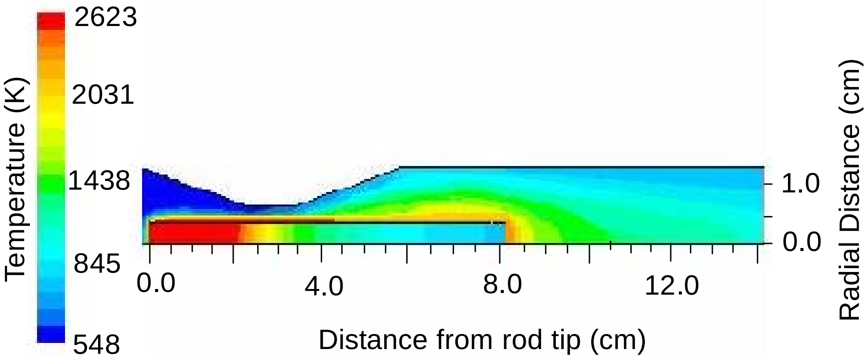

Figure A-28. Predicted temperature profile for the 75/25 mol% CO_2/He case (Case 11).

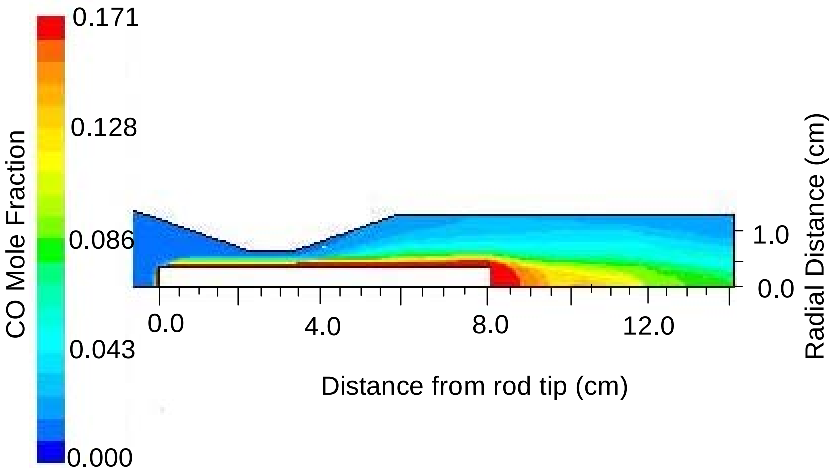

Figure A-29. Predicted CO mole fraction profile for the 75/25 mol% CO2/He case (Case 11).

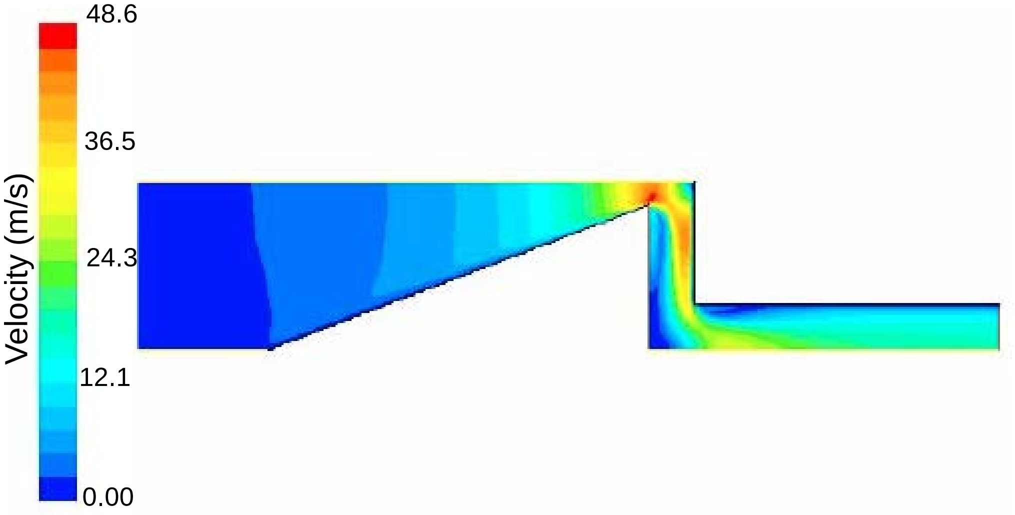

Figure A-30. Predicted velocity profile for the conic rod and impaction plate case (Case 12).

This dissertation also includes a CD. The contents of that CD are listed below, by the section in the dissertation that they correspond to:

-Solar CO_2 Modeling Research

- FLUENT Files for the Base Case Model
- STAR-CD Files for the Base Case Model
- PCGC-3 Files for the Base Case Model File

-Coal Submodel Implementation into STAR-CD

- FORTRAN File with all the implemented Coal Submodels
- Input File for the FORTRAN Submodel Code

- STAR-CD Files for the Validation Case

-Turbulent Premixed Combustion

- LDA Velocity Data and Velocity Profiles
- CARS Temperature Data and Profiles
- PLIF OH Concentration Profiles